2013

Analysis of the B and Be Star Populations of the Double Cluster h and chi Persei

Amber Nichole Boyer
Lehigh University

Recommended Citation

Boyer, Amber Nichole, "Analysis of the B and Be Star Populations of the Double Cluster h and chi Persei" (2013). *Theses and Dissertations.* Paper 1434.

Analysis of the B and Be Star Populations of the Double Cluster h and χ Persei

by

Amber Nichole Boyer

A Dissertation
Presented to the Graduate Committee
of Lehigh University
in Candidacy for the Degree of
Doctor of Philosophy
in
Physics

Lehigh University
September 2013

Approved and recommended for acceptance as a dissertation in partial fulfillment of the requirements for the degree of Doctor of Philosophy.

Amber Nichole Boyer
Analysis of the B and Be Star Populations of the Double Cluster h and χ Persei

Date

M. Virginia McSwain, Dissertation Director, Chair

Committee Members

Accepted Date

George E. McCluskey

John P. Huennekens

James D. Gunton

Michael Stavola

Terry J. Hart

Contents

Acknowledgements **vi**

List of Tables **xii**

List of Figures **xii**

List of Abbreviations **xv**

Abstract **1**

1 Introduction **3**

1.1 Stellar Evolution 4

1.2 Observational Techniques:
Photometry vs. Spectroscopy 6

1.3 Statistical Mechanics 8

1.4 Sources of Continuum Opacity 13

1.5 Line Profile Shapes 16

1.5.1 Bound-Bound Transitions 16

1.5.2 Spectral Line Broadening Mechanisms 16

1.5.3 Physical Structures 20

1.6 Be Star Disk Structure 22

1.7 The Double Cluster: h & χ Persei 26

1.8 Outline of Dissertation 27

2 Observations **28**

2.1 Spectroscopy 28

2.1.1 WIYN 30

2.1.2 WIRO 30
2.1.3 KPNO 2.1m 31
2.1.4 KPNO Coudé Feed 31
2.2 Photometry 31
2.2.1 Strömgren 33
2.2.2 Johnson 34
2.2.3 2MASS 35
2.2.4 *Spitzer* 36
2.2.5 *WISE* 36
2.2.6 *AKARI* 38
2.3 Precision vs. Accuracy 38

3 Determination of Physical Parameters 40
3.1 Spectral Model Fitting for B-type and Non-emission Be Stars 41
3.2 Strömgren Photometric Method for Emission Be Stars 50
3.3 Comparison with Other Studies 55
3.3.1 Huang & Gies 2006 55
3.3.2 Strom et al. 2005 57
3.4 Chapter Summary 57

4 Stellar Distances 60
4.1 Spectral Energy Distributions of B-type Stars 60
4.2 Distance from Absolute Flux 63
4.3 Distance from Spectroscopic Parallax 64
4.4 Summary/Conclusions 66

5 Be Star Disk Models 67
5.1 Disk Variability 67
5.2 Modeling Be Stars from $H\alpha$ Emission 73
5.3 Be Star SEDs 78
5.4 Modeling Be Star Disks Using IR Excesses 79
5.5 Summary/Conclusions 83

6 Conclusions and Further Work **84**

A The Be Stars of h and χ Persei **87**

A.0.1 Star 1057 88
A.0.2 Stars With Only Hα Observations 89
A.1 NGC 869: h Per 90
A.1.1 Star 49 90
A.1.2 Star 146 92
A.1.3 Star 309 94
A.1.4 Star 566 96
A.1.5 Star 717 98
A.1.6 Star 847 100
A.1.7 Star 992 102
A.1.8 Star 1161 104
A.1.9 Star 1261 106
A.1.10 Star 1268 108
A.1.11 Star 1278 110
A.1.12 Star 1282 112
A.2 NGC 884: χ Per 114
A.2.1 Star 1702 114
A.2.2 Star 1926 116
A.2.3 Star 1977 118
A.2.4 Star 2088 120
A.2.5 Star 2091 122
A.2.6 Star 2138 124
A.2.7 Star 2165 126
A.2.8 Star 2262 128
A.2.9 Star 2284 130
A.2.10 Star 2563 132
A.2.11 Star 2771 134

Bibliography **139**

Curriculum Vitae **140**

Acknowledgements

I am grateful to my thesis adviser, Dr. M. Virginia McSwain, for taking me on as a student and guiding me through this process. The experience I've gained by going observing, writing my own proposals and grants, presenting at conferences, and mentoring students has been invaluable and will serve me well as I move into my position at Kutztown University.

With few astronomy faculty in our department, I must sincerely thank my committee members who have taken the time to step well outside of their own fields to consider the stars a little. Their guidance and support have greatly improved this work. Being the only one of us who has slipped the surly bonds of Earth and seen the stars shine pristinely above the atmosphere thru the window of the space shuttle, Professor Hart has brought a unique perspective and wonderful stories to our meetings, and I am very grateful for his presence on the committee. I am also very appreciative of Professors Gunton and Stavola occasionally checking in on me and supporting me during many of the low points of this endeavor.

I owe a lifetime of thanks to my husband, Daniel, for his steadfast support and endless encouragement. We met in Prof. Kritz's plasma physics class shortly before my first shot at the qualifying exams, so I don't think he has ever seen me not stressed and stretched to my breaking point. Since he is also pursuing a doctorate with Lehigh's Mechanical Engineering program, he has been better able to understand the difficulties and frustrations I've faced at each step of this process than most family and friends, and has been more than patient with it all. Without his daily encouragement, guidance, and hugs, I'd have been completely lost. Also, he has requested that I thank him for our "spirited discussions" regarding snags in my research. Being an outside observer, he's often good at looking over my shoulder and pointing out the goofy thing I've done that is causing my problem, but can't see in that moment. He has become my family and my home, and I will always be grateful for that.

While I know our dog Jack may be an unusual addition to this list, he honestly deserves as much credit as Daniel for getting me through the graduate program. A number of folks I know in academia can't seem to understand why on Earth I would opt to get a dog, as opposed to a more self-sufficient cat. Don't get me wrong, I like cats just fine, but the attention that Jack requires has been the one thing that has really prevented me from losing my grip on reality. At some point in the evening I have to go home, have to go outside for a while, and have to do something that has nothing to do with astronomy or physics. His head on my lap while I'm working, and his enthusiastic "Hello!" when I walk in the door have made all the difference in life. His intelligence and personality are beyond any other dog I've had...seriously, what dog knows how to shut a laptop when you've been working too long and forgotten his dinner?

Coming to Lehigh for school meant moving 6 hours away from my family in Virginia. It is impossible to list all of the family moments that I've missed out on the past 5 years being so far away, constantly swamped with work and travel. That aspect of completing this degree has been difficult for me to come to terms with. Still, despite the distance my parents (Jeff and Debbie) and siblings (Zach and Hannah) have been an incredible source of encouragement and laughter. I've always appreciated their advice, and interest in what I'm doing and where I'm traveling. I know it must have started to get annoying somewhere along the line, my constantly calling home and asking what's going on, but I've always appreciated my mom and dad indulging me with a goofy story in those moments and making home feel a little less far away. Zach and Hannah, in particular, were still kids when I left home. I'm incredibly proud of the way they have both begun to carve out their own paths through life, and look forward to seeing where their respective talents take them.

The first homework assignment of the first physics class that I took as a college freshman sent me into an utter panic. I remember timidly walking into my professor's office after a failed attempt at the problems, shamefully explaining that I couldn't figure any of them out and should probably change my major. John Hardie just smirked, told me not to go changing majors yet, and proceeded to fix every problem I'd had in all of 10 minutes. He is still by far the best teacher and mentor I have had in all of my time in academia. Nothing about his classes was easy by any means, but he has an extraordinary talent for teaching complicated material to just about anyone.

When John left before my senior year to go to medical school, conservation of Hardie number dictated that his wife Linda then came back to work at CNU. Linda and I became great friends and running buddies (with her dog Lucy, who often came to work) over my last year. She and John are the only close friends I still keep up with from CNU, and I am forever grateful for their friendship and guidance.

I am incredibly grateful for the continued support and guidance of Edward Brash and my CNU PCSE family. Their reassurance of my abilities, understanding of the Ph.D. process, and words of encouragement have been invaluable to my sanity these past five years. When Ed offered me the opportunity to work with the GEp group at Jefferson Labs, doing high energy physics research, I had no idea how well all those 12am - 8am experiment shifts would serve me when I started going observing. After John's departure, Ed was enormously helpful in guiding me through the ups and downs of the grad school application process. I've never been good at picking up the gist of a concept and just running with it without understanding the details (which I'm sure the faculty here could vouch for). John and Ed made the details transparent without feeling a need to question my level of intelligence because I didn't understand. I hope that in my time at Kutztown I can find a way to emulate the grounded professionalism and genuine enthusiasm for my students that John, Ed, and so many others at CNU embodied.

Most graduate students would agree that having a solid, supporting group of students to work with and around is essential. Christina Aragona and Natalie Hernandez have been the best of group mates along a very challenging path. I cannot thank them enough for their help, support, and enthusiasm regarding research and life outside of physics. I have gotten to know a number of the upperclassmen who have already come and gone through the program, and all have provided advice and encouragement that I very much appreciate. Dave Kashinski and Jeff Stephens pretty much adopted me from the start and have always been there when I needed it. It was like I had gone to grad school with my older brothers! Ruthie Malenda was the first and only person I really knew when I decided on Lehigh. Right after I got my offer, she immediately emailed me to say I was going to live with her, no questions about it, I think before I even had a chance to send my official letter back. Since then, she has been an enormous source of support in every aspect of life. Thank you Ruthie, for everything.

The abilities I have developed as an observer are largely thanks to Tabitha Boyajan, who showed me the ropes my first time observing at Kitt Peak as a first year student. Over the course of graduate school Tabitha, Erika Grundstrom, Saida Caballero, and Yamina Touhami have become incredible friends and mentors to me, providing a sounding board for difficult problems and excellent conference companions. I am incredibly grateful to Wenjin Huang and Doug Gies for their thoughtful feedback regarding this work. Doug in particular has continually shared his interest and enthusiasm in the field of massive stars, and is always ready with excellent conversation that fends off doubts when things are tough.

We are grateful to the University of Wyoming for providing observing time at the WIRO 2.3m telescope, as well as to Chip Kobulnicky and Dan Kiminki for their support of our observations. A.N.M.B. is grateful for thesis student travel support provided by NOAO. We would like to thank Yale University for providing access to the WIYN telescope at KPNO. The WIYN Observatory is a joint facility of the University of Wisconsin-Madison, Indiana University, Yale University, and the National Optical Astronomy Observatory. We are very grateful to the support staff at NOAO, especially Di Harmer and Daryl Wilmarth for their help in obtaining our observations at KPNO.

This publication makes use of data products from the Two Micron All Sky Survey, which is a joint project of the University of Massachusetts and the Infrared Processing and Analysis Center/California Institute of Technology, funded by the National Aeronautics and Space Administration and the National Science Foundation. This work is also based [in part] on observations made with the Spitzer Space Telescope, which is operated by the Jet Propulsion Laboratory, California Institute of Technology under a contract with NASA. Support for this work was provided by NASA through an award issued by JPL/Caltech. This publication makes use of data products from the Wide-field Infrared Survey Explorer, which is a joint project of the University of California, Los Angeles, and the Jet Propulsion Laboratory/California Institute of Technology, funded by the National Aeronautics and Space Administration. This research is based on observations with AKARI, a JAXA project with the participation of ESA.

In completing this week we have made use of the NASA/ IPAC Infrared Science Archive, which is operated by the Jet Propulsion Laboratory, California Institute of Technology, under contract with the National Aeronautics and Space Administration. We have also utilized the WEBDA database, operated at the Institute for Astronomy of the University of Vienna, as well as NASA's Astrophysics Data System. This research has made use of the SIMBAD database, operated at CDS, Strasbourg, France. IRAF is distributed by the National Optical Astronomy Observatory, which is operated by the Association of Universities for Research in Astronomy (AURA) under cooperative agreement with the National Science Foundation.

This work has been supported by the National Science Foundation under grant AST-1109247 and by NASA under DPR numbers NNX08AX79G, NNX09AP86G, and NNX11AO41G. A.N.M.B. has also been supported by a Grant-In-Aid of Research (G20110315157195) from the National Academy of Sciences, administered by Sigma Xi. And finally, institutional support was provided by Lehigh University.

List of Tables

2.1 Journal of Spectroscopy 29
2.2 Photometric Catalogs 32
2.3 Photometric Filter Specifications 33

3.1 Physical Parameters of B-type Cluster Members 43
3.1 Physical Parameters of B-type Cluster Members 44
3.1 Physical Parameters of B-type Cluster Members 45
3.2 Physical Parameters of Be Star Cluster Members 46
3.2 Physical Parameters of Be Star Cluster Members 47

5.1 Be Star Hα Equivalent Widths 70
5.2 Be Star Disk Parameters from Hα Equivalent Widths 76
5.2 Be Star Disk Parameters from Hα Equivalent Widths 77
5.2 Be Star Disk Parameters from Hα Equivalent Widths 78
5.3 Be Star Disk Parameters from IR Excesses 82

List of Figures

1.1 Hertzsprung-Russell Diagram 6
1.2 Simplified schematic of a slit spectrograph. 7
1.3 Relative occupancy of the n = 1 and n = 2 states of hydrogen with respect to temperature. 10
1.4 Fraction of ionized hydrogen relative to temperature. 11
1.5 Fraction of all hydrogen available in the n = 2 excitation state with respect to temperature 12
1.6 Effects of T_{eff}, log g, and V sin i on overall line profile shape. 18
1.7 Normalized Gaussian, Lorentzian, and Voigt profile shapes. 19
1.8 Line profile shape components for a spherical outflow. 21
1.9 Be star line profile shape components. 22

2.1 Strömgren *uvby* normalized spectral responses 35
2.2 Normalized spectral response curves for the various filter systems used in this work for SED fitting. 37

3.1 Sample spectral line fits for NGC 869-90 41
3.2 Cumulative distribution function of V sin i 48
3.3 For both NGC 869 and NGC 884, T_{eff} and log g_{polar} are plotted with the evolutionary tracks of Schaller et al. (1992) 51
3.4 Calibration of Strömgren photometry method 54
3.5 Comparison of parameter results with Huang & Gies [2006a], Strom et al. [2005], and Slesnick et al. [2002]. 58

4.1 Illustration of the relevant geometric quantities for determining stellar distance via angular diameter. 61

4.2 Example SED of B-type star NGC 869 - 864. 63
4.3 Distance results for absolute flux method 64
4.4 Distance results for spectroscopic parallax method 66

5.1 Illustration of line equivalent width 68
5.2 Hα spectra of stars NGC 884–1702 and NGC 884–1926 69
5.3 Results of $W_{H\alpha}$ analysis 71
5.4 Results of $W_{H\alpha}$ analysis compared to T_{eff} 72
5.5 Resultant R_d, ρ_0, and M_d from the models of Grundstrom & Gies [2006] 75
5.6 Example SED of Be Star NGC 869 - 1282 79
5.7 Example Be disk SED of NGC 884-1926 82

A.1 Hα spectra of NGC 869-1057 88
A.2 Hα spectra of NGC 869–517, NGC 869–846, and NGC 884–1772 . . 89
A.3 Observed Hα spectra of NGC 869–49 90
A.4 Observed SED and disk excess of NGC 869-49 91
A.5 Hα spectra of NGC 869-146 92
A.6 Observed SED of NGC 869-146 93
A.7 Hα spectra of NGC 869-309 94
A.8 Observed SED and disk excess of NGC 869-309 95
A.9 Hα spectra of NGC 869-566 96
A.10 Observed SED and disk excess of NGC 869-566 97
A.11 Hα spectra of NGC 869-717 98
A.12 Observed SED of NGC 869-717 99
A.13 Hα spectra of NGC 869-847 100
A.14 Observed SED and disk excess of NGC 869-847 101
A.15 Hα spectra of NGC 869-992 102
A.16 Observed SED and disk excess of NGC 869-992 103
A.17 Hα spectra of NGC 869-1161 104
A.18 Observed SED and disk excess of NGC 869-1161 105
A.19 Hα spectra of NGC 869-1261 106
A.20 Observed SED and disk excess of NGC 869-1261 107
A.21 Hα spectra of NGC 869-1268 108
A.22 Observed SED of NGC 869-1268 109

A.23 Hα spectra of NGC 869-1278 110
A.24 Observed SED and disk excess of NGC 869-1278 111
A.25 Hα spectra of NGC 869-1282 112
A.26 Observed SED and disk excess of NGC 869-1282 113
A.27 Hα spectra of NGC 884-1702 114
A.28 Observed SED of NGC 884-1702 115
A.29 Hα spectra of NGC 884-1926 116
A.30 Observed SED and disk excess of NGC 884-1926 117
A.31 Hα spectra of NGC 884-1977 118
A.32 Observed SED and disk excess of NGC 884-1977 119
A.33 Hα spectra of NGC 884-2088 120
A.34 Observed SED and disk excess of NGC 884-2088 121
A.35 Hα spectra of NGC 884-2091 122
A.36 Observed SED and disk excess of NGC 884-2091 123
A.37 Hα spectra of NGC 884-2138 124
A.38 Observed SED and disk excess of NGC 884-2138 125
A.39 Hα spectra of NGC 884-2165 126
A.40 Observed SED and disk excess of NGC 884-2165 127
A.41 Hα spectra of NGC 884-2262 128
A.42 Observed SED of NGC 884-2262 129
A.43 Hα spectra of NGC 884-2284 130
A.44 Observed SED and disk excess of NGC 884-2284 131
A.45 Hα spectra of NGC 884-2563 132
A.46 Observed SED and disk excess of NGC 884-2563 133
A.47 Hα spectra of NGC 884-2771 134
A.48 Observed SED and disk excess of NGC 884-2771 135

List of Abbreviations

AAS	American Astronomical Society
AKARI	Japanese for "light"; Infrared Satellite developed by the Japan Aerospace Exploration Agency
AURA	Universities for Research in Astronomy
BC	Bolometric Correction
CCD	Charge-Coupled Device
CF	Coudé Feed
EM	Electromagnetic
FIS	Far-Infrared Surveyor
FWHM	Full-Width Half-Maximum
HJD	Heliocentric Julian Date
IAU	International Astronomical Union
IDL	Interactive Data Language
IPAC	Infrared Processing and Analysis Center
IR	Infrared
IRAC	Infrared Array Camera
IRAF	Image Reduction and Analysis Facility
IRC	Infrared Camera
IRSA	Infrared Science Archive
ISM	Interstellar Medium
JPL	Jet Propulsion Laboratory
KPNO	Kitt Peak National Observatory
LTE	Local Thermodynamic Equilibrium
MIPS	Multi-Band Imaging Photometer
NASA	National Aeronautics and Space Administration
NASA ADS	NASA's Abstract Database System
NOAO	National Optical Astronomy Observatory
NRP	Non-radial Pulsation
NSF	National Science Foundation

SED	Spectral Energy Distribution
SIMBAD	Set of Identifications, Measurements, and Bibliography for Astronomical Data
UT	Universal Time
UV	Ultraviolet
WEBDA	Web Database of Open Clusters
WIRO	Wyoming Infrared Observatory
WISE	Wide-field Infrared Survey Explorer
WIYN	Wisconsin Indiana Yale and NOAO
ZAMS:	Zero Age Main Sequence
2MASS	2 Micron All-Sky Survey

Abstract

In this dissertation we present a study of the B and Be star populations of the Double Cluster h and χ Persei. Classical Be stars are best known for their circumstellar disks, which are composed of material ejected off of the stellar surface during outburst events. These open clusters present an optimal location for studying the physical properties and variability of these disk structures, as upwards of 30% of the brightest B-type stars in h and χ Per are known to be Be stars.

To begin our study, we first need to establish reliable measurements of basic physical parameters for each B-type and Be star in our sample. Blue optical spectroscopy is used to first measure projected rotational velocity, $V \sin i$, effective surface temperature, $T_{\rm eff}$, and surface gravity, $\log g$, for B-type sample stars, while available Strömgren photometry is used to calculate $T_{\rm eff}$ and $\log g$ for the Be stars showing emission. Stellar masses and radii are then determined for each star via the evolutionary tracks of Schaller et al. [1992].

With these measurements, the model B-type star spectral energy distributions of Lanz & Hubeny [2007], and photometric observations in the optical, near- and mid-IR wavelengths, we then use two independent means of determining the distance to each star, and compare these to the established cluster distances from the study of Currie et al. [2010]. This serves as a check of the reliability of our parameter determinations and our ability to model the total stellar flux of these B-type stars.

Our study of the cluster Be stars is continued by examining the disk spectral energy distributions via photometric observations from WEBDA, 2MASS, *Spitzer*, *AKARI*, and *WISE*. Using the methods we have developed for modeling B star stellar flux, we can now extract the Be disk contribution to the total system flux. We also present multiple observations of Hα taken between 2009-2012 with the KPNO Coudé Feed, KPNO 2.1m, and WIRO telescopes, used to monitor the presence of disk

emission and its strength in our sample Be stars. We use the Hα equivalent width model of Grundstrom & Gies [2006] and the infrared flux model of Touhami et al. [2011] to constrain the disk masses, radii, and densities for our Be star sample. We find that our sample Be stars have disks $10 - 100$ R$_\odot$ in size, have densities typical of other observed Be disks, and that nearly all exhibit some level of variability in the size and strength of their disks over the course of our observations.

Chapter 1

Introduction

Usually, one thinks of stars as being constant. Always just over head, appearing after every sunset, decorating a clear night sky with a comforting consistency. With thousands of years of careful observation, we have slowly learned that these small points of light are in fact changing in a multitude of different ways. What I have personally always found fascinating is that we can actually watch some of these changes happen over the course of many years, a few months, or within a few seconds. With lifetimes of different stars spanning several thousands of years to older than the current age of the universe, it is simply spectacular that there are significant short term changes in these tiny points of light and that we have the tools to watch it happen, much like a flip book.

Through this dissertation I hope to share the story of a particular type of star that has caught my attention. Each time I've gone out to observe the clusters this work centers on, I'm curious to see if and how each of the Be stars in my sample and the disks they host have changed since I last checked in. These unique B-type stars are 2–10 times the physical size of our Sun (which is roughly 100 times the radius of Earth), and have disks of gaseous hydrogen material that are typically a few times the the radius of the star in size. These Be disks have been observed to change dramatically, even in the span of a few nights or weeks. Some even lose their disks entirely at different times, which is not a trivial event for such a physically large structure.

To start this story of Be stars in the Double Cluster h and χ Persei, we first need to spend some time talking about the specific characteristics of stars, how they change over time, the physics governing their existence, and what questions we hope to answer through the work detailed in the later chapters of this dissertation. We'll begin broadly by taking a look at what a B-type star is and how it compares to all the other stars we see in the night sky.

1.1 Stellar Evolution

Even the earliest astronomers, using only their eyes, noticed that not all stars they could see in the sky appeared to be the same. While their hypothesized reasons for these differences were wrong, these early observers were correct that not all stars are wrought from the same mold. In fact there is a veritable zoo of stars throughout the universe ranging in size, mass, temperature, brightness, and composition. Stars also undergo a number of physical changes over the course of their existence, some more drastic than others, that ultimately change their size, temperature, brightness, and composition over time.

All stars start life as dense clumps of gas and dust, condensing and slowly growing in mass from nebular clouds. As material is continually added (accreted) onto the protostar, temperature, density, and pressure increase in the interior until they become high enough for nuclear fusion to occur. At this point the star begins to generate its own energy in its core, accretion stops, and the radiation pressure produced by the fusion of hydrogen into helium is able to halt the gravitational collapse of material at the stellar surface. The star is now considered to be a main sequence object.

How long a star lives and what evolutionary path it will take is predominantly dependent upon its mass when it moves onto the main sequence. Along the main sequence effective temperature and luminosity (brightness) increase with mass. Modern classification schemes group stars into spectral types, OBAFGKM, based upon their temperatures, with O- and B-type stars being the hottest, most massive, and most luminous. Each spectral class is further broken up into classes 0–9, such that a B0 star is hotter and more massive than a B5 star, which is then hotter and more massive than a B9 star. These hot O- and B-type stars have very short lifetimes, on the order of a few millions of years. Though they start out with a larger supply of material for fusion, they must use their stores at very rapid rates in order to sustain themselves against gravitational collapse. Once a massive star depletes the available hydrogen in its core, it will leave the main sequence and undergo a series of core contraction and envelope expansion events. When this occurs, the star will evolve into a giant or supergiant star. During these contractions the photosphere cools and expands in radius, while the core temperature and density increases until the next stage of fusion is able to occur, from helium up to nickel and iron in the most massive of O-type stars. After reaching the limits of fusible material in their cores massive stars end their lives spectacularly with a supernova explosion, leaving behind a neutron star or stellar-mass black hole remnant.

Cooler stars, being less massive and less bright, are able to use their fusion fuel supplies at a much slower rate, thus extending their lifetimes by several orders of magnitude. Stars like our Sun will spend upwards of ten billion years on the main sequence, evolve into red giants, and eventually end their lives as slowly cooling white dwarfs after having blown away their remaining photospheres. The coolest M-type stars have lifetimes on the order of the age of the Universe, and will slowly cool and fade once they have completely exhausted the hydrogen they are composed of, without ever evolving off of the main sequence.

During the various stages of any star's evolution, it experiences significant changes in its radius and surface temperature, which are strongly tied to the brightness of the star. The Stefan-Boltzmann relation

$$L = 4\pi R^2 \sigma T^4 \tag{1.1}$$

illustrates the dependancies of luminosity on stellar radius and temperature. Measuring temperature and luminosity for a sample of stars covering all spectral types, and evolutionary stages, we can create a Hertzsprung-Russell diagram like the one shown in Figure 1.1. In this figure main sequence stars are designated by *plus* symbols, giants by *asterisks*, and supergiants by *cross* symbols. The solid track included in this figure illustrates how a massive B-type star of 9 $M_\odot$ moves across this diagram over the various evolutionary phases of its life.

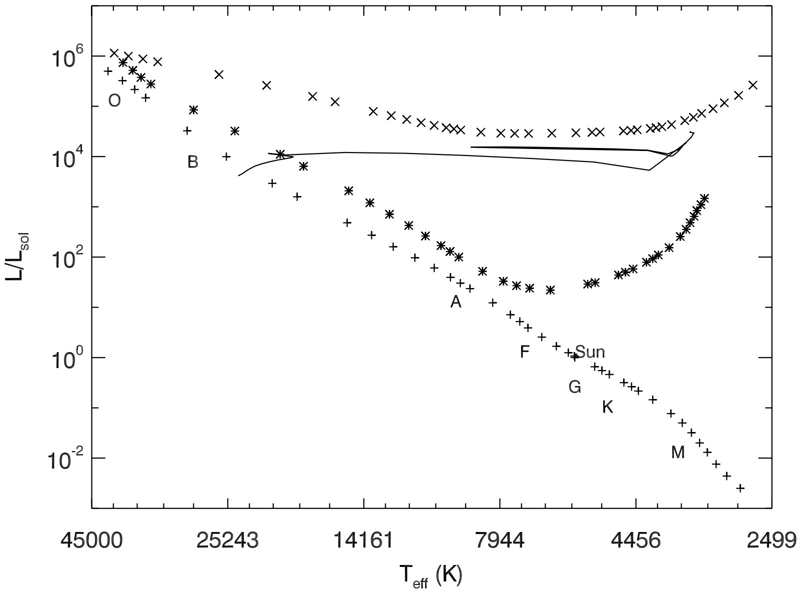

Figure 1.1 Hertzsprung-Russell diagram utilizing the stellar data provided in Appendix G of Carroll & Ostlie [2007]. Main sequence (*plus*), giant (*asterisks*), and supergiant (*cross*) star temperatures and luminosities are shown with a 9 M$_\odot$ evolutionary track from Schaller et al. [1992].

1.2 Observational Techniques: Photometry vs. Spectroscopy

The advent of the telescope in the early 1600's allowed early astronomers to begin looking further and further out into the night sky, beyond the reach of the unaided human eye. With the advances that have been made in the materials and technology utilized in telescopes today, there are a multitude of different observing techniques that are available to modern astronomers, providing the means to peer into birthplaces of stars and out to the very edge of the observable universe. Two of the most widely used and versatile observing techniques are spectroscopy and photometry.

Spectroscopy measures the intensity (amount) of radiation being emitted by an object as a function of wavelength on a very fine wavelength scale, over a region of the electromagnetic (EM) spectrum. To do this, light is first collected by a telescope and then passed though a very narrow slit. The star light is then collimated by a mirror and directed onto a diffraction grating, which is a very finely etched reflective surface which spreads the light out into its constituent wavelengths. After reflecting off of the grating, the spectrum is focused onto a CCD detector and recored for use. Traditional spectrographs can take data on only one star at a time, while newer instruments using optical fibers are now able to simultaneously take spectra of up to 100 objects at a time in a small region of the sky. A simple schematic of a spectrograph is shown in Figure 1.2.

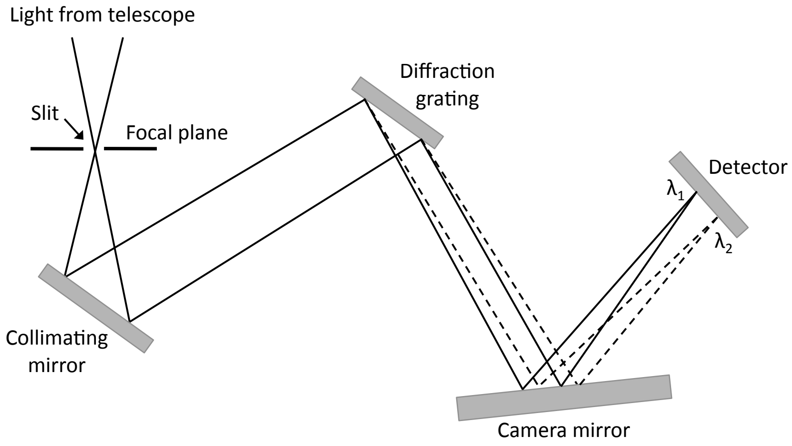

Figure 1.2 Simplified schematic of a slit spectrograph.

Photometry also measures the intensity of radiation being emitted by an object but does so on a much more coarse wavelength scale than spectroscopy. Light from a region of the sky, like a cluster of stars, is collected and the image is focused by a telescope, and then passed through a filter which only allows photons within a specified wavelength range through. The light which makes it through the filter is again focused and directed onto a CCD detector which essentially records how many photons from each source passed through the filter. This measure of brightness of an object through a specific filter is referred to as a "magnitude", and when considered with other magnitudes of the same object through other filters covering different wavelength regions, allows for the investigation of a number of different physical properties. Today there are a plethora of different photometric filters available in the ultra-violet (UV), optical, and infrared (IR) spectral regions.

Though the techniques are somewhat similar, there are pros and cons to both spectroscopy and photometry. Spectroscopy provides extraordinarily detailed measurements of the individual spectral lines of an object, and can be utilized for a number of applications: measuring rotation, effective temperature, and surface gravity of single stars, properties of binary systems, characteristics of events on the surface of the star and its surrounding environment, physical composition and evolutionary state to name a few. The detailed information provided by spectroscopy comes at the cost of time and restricted wavelength coverage. Traditional telescope instruments can only take one spectrum of one object at a time, and since the source light is being significantly dispersed, longer exposures to collect enough light are needed. Photometry provides excellent imaging capabilities and allows for quick magnitude measurements of a large group of stars at a single time. En mass, it can provide a look at the evolutionary state of a large sample or cluster of stars, track subtle variations in brightness over time, and allow for a first pass of a large group of stars when looking for particular objects exhibiting atypical features effecting their brightness. Obtaining many magnitude measurements covering the full UV to far-IR spectral regions can also provide a look at the amount of light emitted by the star across the EM spectrum, and is effectively a very low resolution spectrum covering a very wide wavelength range. But the cost here is in the level of detail that can be obtained about the physical properties of an individual star or its environment.

When used in complement, the broad measurements provided by photometry and the detailed measurements of spectral lines yielded by spectroscopy allow for the in-depth examination of the physical characteristics of a large sample of stars.

1.3 Statistical Mechanics

Even on the grandiose scale of stars, the details of atomic interactions still reign supreme and are governed by the laws of statistical mechanics. Stars are, in the simplest of terms, just large collections of gases composed of various atoms that interact according to the temperatures, densities, and pressures they experience. To understand the physical mechanisms underlying the modern stellar classification scheme, which exploits the fact that stars of different temperatures exhibit different lines of varied strength in their spectra, we have to consider the atomic conditions in the stellar atmosphere. More specifically, in what energy levels (orbitals) are electrons most likely to be found within their host atoms, and what are the relative numbers of atoms in various states of ionization? Ionization is a state in which an atom has lost an electron. With the removal of one electron, an atom is said to be singly ionized, remove a second and it is doubly ionized, and so forth. We will consider the questions of energy level occupation and ionization state with regard to hydrogen atoms, and an emphasis on massive O- and B-type stars.

As atoms in a gas move around they gain and lose energy by colliding with other atoms. When an atom gains energy, the electrons it hosts are able to make transitions from lower energy levels to higher energy levels. The loss of energy during a collision results in one of these electrons in a higher energy state giving up a requisite amount of energy and transitioning to a lower state. In general, the higher energy states in a given atom are less likely to be occupied by electrons at any given time. The rate at which these collisions occur, and the ratios of energy level occupations is intimately related to the temperature of the gas under consideration. The Boltzmann equation, which is used to describe the thermal population of the levels of a particular atom, is given as a ratio of the number of atoms in each of two different states of excitation, N_a and N_b,

$$\frac{N_b}{N_a} = \frac{g_b e^{-E_b/kT}}{g_a e^{-E_a/kT}} = \frac{g_b}{g_a} e^{-(E_b - E_a)/kT}. \tag{1.2}$$

Here g_a and g_b denote the degeneracies of excitation states a and b, E_a and E_b are the energies of the states, and T is the gas temperature in Kelvin units.

Plugging in the appropriate degeneracies ($g_n = 2n^2$) and energies for the ground (n = 1) and first excited (n = 2) states for hydrogen, we can determine the ratio of $N_2/(N_1 + N_2)$ with respect to temperature, as shown in Figure 1.3. We find that this ratio of $N_2/(N_1 + N_2)$ is 50% for a temperature of 85,400 K, which is several times hotter than a typical B-type or even O-type star. This requires most all electrons in hydrogen to be in the n = 1 ground state at normal stellar surface temperatures. Since transitions upwards from and down to the n = 2 state in hydrogen are responsible for producing the Balmer set of lines in the optical wavelength region, which are the predominant spectral features in massive stars, this seems exorbitantly high. To reconcile this theoretical occupation of energy states with observations, we must also consider the ionization state of the hydrogen gas.

Much as the ratios of energy level occupations are governed by the temperature

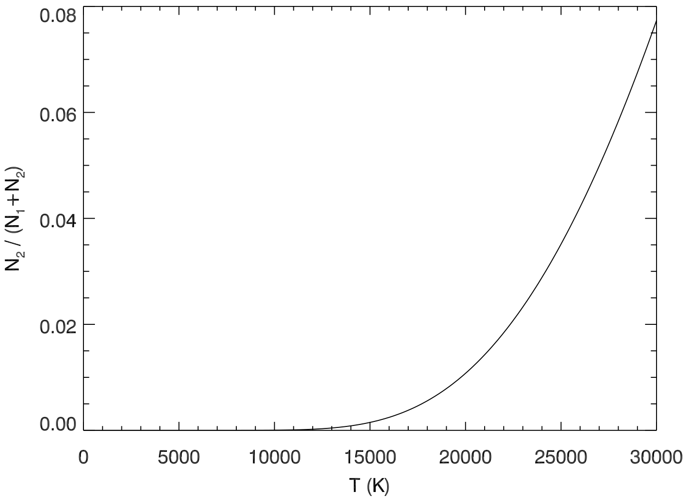

Figure 1.3 Relative occupancy of the n = 1 and n = 2 states of hydrogen with respect to temperature.

of the gas in question, so is the ratio of states of ionization in the gas. The Saha equation is given as a fraction of ionization levels, N_{i+1} and N_i,

$$\frac{N_{i+1}}{N_i} = \frac{2Z_{i+1}}{n_e Z_i} \left(\frac{2\pi m_e k T}{h^2} \right)^{3/2} e^{-\chi_i/kT}, \tag{1.3}$$

for a mixture of gasses. In this expression n_e designates the number density of free electrons in the gas, m_e is the electron mass, T is the gas temperature, k is Boltzmann's constant, h is Planck's constant, and χ_i is the ionization energy of the ground state of the atom. The partition function, Z, is given by

$$Z = \sum_{j=1}^{\infty} g_j e^{-(E_j - E_1)/kT}, \tag{1.4}$$

where E_j is the energy of the *jth* energy state and g_j is the degeneracy of that state. The partition function is simply a weighted sum of all the possible ways the electrons in an atom can be arranged with the same energy. Electron arrangements that are more energetic, and therefore less likely to occur, are weighted less than less energetic arrangements. The factor of two in Equation 1.3 accounts for the two possible spin orientations (up or down) of the free electron.

For most atoms, this must be solved as a coupled set of equations, however, the situation for hydrogen can be simplified to provide a quick analytic solution. For a mixture of pure hydrogen with most atoms in the ground state, the partition function of neural hydrogen Z_I is approximately equal to the ground state degeneracy $g_I = 2$. The partition function for ionized hydrogen (i.e. a proton) is then $Z_{II} = 1$. We set $n_e = 10^{20}$, which is a typical value in most stellar atmospheres, and $\chi_i = -13.6$ eV for hydrogen. Determining this ionization fraction $y = N_{II}/N_{total}$ with respect to T, as shown in Figure 1.4, we find that half of the available hydrogen is ionized ($y = 0.5$) at $\sim 9,000$ K.

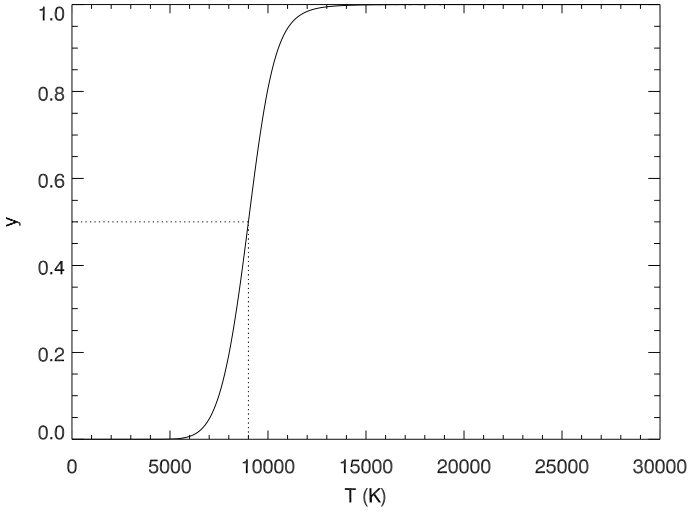

Figure 1.4 Fraction of ionized hydrogen relative to temperature. At a temperature of $\sim 9,000$ K, the hydrogen is half ionized.

Combining the results of Equations 1.2 and 1.3, we can determine the strength of the Balmer lines as a function of temperature. The overall strength of these lines depends on the faction of all hydrogen atoms that are in the n = 2 excitation state. This fraction is given as

$$\frac{N_2}{N_{total}} = \left(\frac{N_2}{N_1 + N_2}\right)\left(\frac{N_I}{N_{total}}\right), \tag{1.5}$$

and when considered as a function of T, results in the distribution shown Figure 1.5. We see that fraction of hydrogen available to produce the Balmer lines increases from

$5,000$ K, peaks at $\sim 10,000$ K, and then quickly falls off with increasing temperature as more of the hydrogen that can produce the Balmer lines becomes ionized. This agrees well with observations, and provides an excellent physical means for classifying stars.

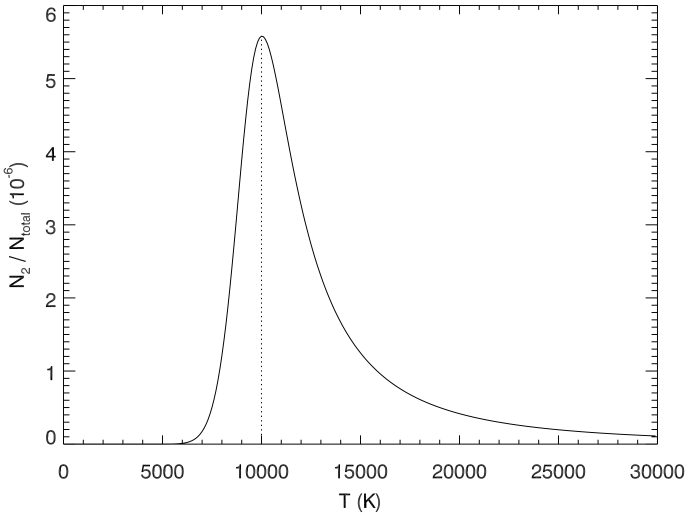

Figure 1.5 Fraction of all hydrogen available in the n = 2 excitation state, contributing to the strength of the hydrogen Balmer lines, with respect to temperature.

The entire lifetime of a star after formation is spent fighting off the force of gravity which is trying to collapse it. Since gravity is an attractive force, there must be an outward force produced in the stellar interior which counters it. This outward force is produced by radiation pressure, which is generated by the fusion of hydrogen and other materials in the stellar core. The more massive a star is, the larger its gravity and thus the greater the pressure that must be generated by the interior at a given time. For massive O- and B-type stars this results in the short lifetimes mentioned in Section 1.1, and explains why they exhaust their fusible supplies at such a rapid rate.

Assuming that the star is static and the acceleration at the surface is zero, the condition for hydrostatic equilibrium is given by

$$\frac{dP}{dr} = -G\frac{M_r \rho}{r^2} = -\rho g, \tag{1.6}$$

where $g = GM_r/r^2$ is the local acceleration of gravity at a radius r, or surface gravity. From this expression we see that an interior pressure gradient, a change in pressure with radius, is required for a star to balance the inward force of gravity and maintain stability. The negative sign also indicates that this pressure must decrease with increasing radius, such that the interior pressure is larger than near the stellar surface. It is because stars are in hydrostatic equilibrium, that we can utilize the Boltzmann and Saha equations to describe the atomic states of their atmospheres.

1.4 Sources of Continuum Opacity

When a beam of light produced in the interior of a star passes through gaseous material, like the stellar photosphere, some of the photons from the beam will be removed or have their paths diverted. In stellar photospheres the gaseous material is typically comprised of atoms (predominantly hydrogen, helium), ions, and free electrons. These disruptions to the paths of the escaping photons are caused by the atomic processes of absorption and scattering. When photons are removed from the beam on its way to an observer on Earth, the original intensity I_λ is diminished by some amount dI_λ over the path ds the beam travels

$$dI_\lambda = -\kappa_\lambda \rho I_\lambda ds. \tag{1.7}$$

In this expression we see that the decrease in intensity is dependent on the density ρ of the material the beam is traveling through, as well as the opacity κ_λ. Opacity defines the cross section within which absorption or scattering of photons can occur per unit mass of gaseous material. This quantity is wavelength dependent and is a function of the gas composition, density, and temperature. When a photon passes within the cross-sectional area of a charged particle, there are a number of ways in which the target particle can interact with the incident photon.

Closely related to opacity is optical depth τ_λ which is essentially a measure of the number of scattering events a photon may undergo while passing through a gas (photosphere, molecular cloud, ISM, etc.) as measured for a photon along a given path.

$$d\tau_\lambda = -\kappa_\lambda \rho ds. \tag{1.8}$$

With this definition, we can now express the change in intensity of a beam in terms of the optical depth of the medium it is passing through

$$dI_\lambda = I_\lambda d\tau. \tag{1.9}$$

There are a myriad of different processes which contribute to the opacity of gas clouds, dust, and the photospheres of stars, the most prominent of which will be discussed in the remainder of this section.

In the case of bound-free absorption, otherwise known as photoionization, an incident photon of high enough energy will ionize an atom. The photon wavelength must be less than or equal to hc/χ_n, where χ_n is the ionization energy of the n^{th} atomic energy level. Ionization is a process whereby an outer valence electron initially bound to its atom is imparted enough energy by the incident photon that it is removed from the atom and becomes a free electron. This process is a significant source of continuum opacity in B- and A-type stars with the photoionization of neutral hydrogen, and to a lesser extent helium. The inverse of this process, free-bound emission, occurs when a free electron recombines with a nearby ion, emitting one or more photons in random directions as a result.

Free-free absorption is a process in which a free electron in the presence of an ion absorbs an incident photon. This absorption causes the speed of the electron to increase and deflect its trajectory. Free-free absorption can occur for a continuous range of wavelengths, and thus is another significant contributor to continuum opacity. Similarly, an energetic free electron may pass by an ion, in which case the electron gives up energy by emitting a photon and thus slows down (free-free emission). This effect is particularly important for circumstellar disks, which will be discussed further in Section1.5.3. These absorbing processes are also known as thermal bremsstrahlung.

Thompson scattering occurs when a photon is scattered, rather than absorbed, by a free electron when the electron oscillates in the electromagnetic field of the photon. The cross-section for this process is approximately 2×10^6 times smaller than that of the photoionization of hydrogen. While this is very small, in electron-dense environments this becomes a very effective means of scattering. In stellar interiors and the photospheres of massive stars, where temperatures and ionization rates are high, Thompson scattering is the dominant source of continuum opacity.

Rayleigh scattering also involves the electromagnetic field of an incident photon driving oscillations of an electron, but occurs for bound electrons. Because this occurs for electrons bound within atoms, the cross-section for this process is even smaller than for Thompson scattering and requires more energetic photons with shorter wavelengths. For photons of wavelengths shorter than the size of the atom, undergoing a slightly different interaction, this process is referred to as Compton scattering. Opacity contributions from Rayleigh scattering are negligible in most stellar atmospheres, but are more significant in regard to interstellar dust and nebular clouds of gas.

The interstellar medium (ISM) is composed of large, very diffuse amounts of fine dusty material that exists in the seemingly empty regions between stars. Giant clouds of gas which may eventually condense to form stars are present, particularly in the spiral arm and central regions of our galaxy. All of these gaseous materials tend to absorb or scatter out starlight as it passes through, preferentially scattering shorter wavelength photons via Compton scattering. Because more blue photons are removed by this process, the starlight received by the observer appears to be more red overall, hence this effect is often referred to as reddening.

As might be expected, reddening can have significant impacts on the continuum observations of stars in particularly dusty regions of space, or where there is a significant amount of absorbing material (ISM) along the line of sight. Correcting for the effects of reddening requires careful measurement of the observed color excess of an object in comparison to its expected or intrinsic color, which is determined by its temperature. In astronomy, a "color" refers to a difference between two magnitudes, such as the Johnson B and V filters, which are often used to measure the extinction $\mathrm{E}(B-V)$,

$$\mathrm{E(B-V)} = \mathrm{(B-V)_{obs}} - \mathrm{(B-V)_{int}} \tag{1.10}$$

along a line of sight to a particular object. As shown in the above expression, the difference between these observed and intrinsic colors provide the necessary reddening correction for observed deficiency in shorter wavelength continuum intensity. The change in magnitude due to extinction is approximately equal to the optical depth τ_λ along the line of sight, so Equation 1.8 can also be expressed as

$$d\tau = n_d(s)\sigma_\lambda ds, \tag{1.11}$$

in terms of the number density $n_d(s)$ of the scattering dust grains along the line of sight, and the scattering cross section σ_λ of the scattering material.

1.5 Line Profile Shapes

1.5.1 Bound-Bound Transitions

Bound-bound transitions are simply the excitations and de-excitations of atoms or ions in a gas, and occur with the movement of an electron from one energy state to another. These radiative transitions are the only source of discrete opacity, forming the absorption and emission lines of stellar spectra. To make these transitions, an electron must absorb (excitation) or emit (de-excitation) a photon of a discrete wavelength, which is determined by the difference in energy of the initial and final states.

Spontaneous emission, as indicated by its name, occurs when an electron in an upper energy state spontaneously emits a photon of a specific wavelength. The photon carries away energy and allows the electron to transition to a lower energy state. Stimulated absorption is simply the absorption of a passing photon by an electron, which is then able to transition upwards to a higher energy state. The last of these bound-bound transitions, stimulated emission, occurs when an incident photon of a specific energy interacts with an electron in a higher state, inducing the electron to transition to a lower state and emit a second photon.

The overall shape of these absorption and emission lines found in spectra are governed by a number of physical mechanisms, detailed below.

1.5.2 Spectral Line Broadening Mechanisms

The observed spectral lines we will measure are produced in the outer, less opaque layers of the stellar atmosphere, known as the photosphere, and are due to transitions between various energy levels of the atoms comprising the gas. If the atoms in the gas were not perturbed in any way, one would expect very narrow, sharp lines at the rest wavelength specific to each atomic transition. However, all spectral lines have some observed width that is due to a variety of broadening mechanisms, which can allow us to determine other characteristics of the star (eg. rotation rate, temperature, surface gravity).

Natural broadening is inherent to some degree in every spectral line, and is ultimately due to the Heisenberg uncertainty principle. Each atomic energy level has an associated lifetime and energy, each with some degree of uncertainty. It is this uncertainty in the energy for a given transition that produces an observable spread in the absorption or emission wavelength of a spectral line.

Doppler thermal broadening is produced due to the random thermal motions of atoms in the gas. Each atom has an associated velocity in a random direction that is dependent upon the temperature of the gas. The orientation of this velocity with respect to the line of sight of the observer will produce red (away from observer) or blue (towards observer) shifted wavelengths of the emission or absorption lines. Generally speaking, higher temperatures will produce a broader distribution of Doppler shifted frequencies, and thus a broader line profile shape. For massive O and B-type stars, however, we see a trend opposite to this illustrated in Figure 1.6(a), which is due to the ionization of more and more neutral hydrogen material at higher temperatures. There is less material available to make the transitions producing the hydrogen absorption line, resulting in a narrower line with increasing temperature.

Pressure or collisional broadening is due to the perturbation of atomic energy levels in a gas by the electric fields of passing atoms and ions. Higher pressures, coupled with higher densities and temperatures, increase the collisional rates for atoms in the gas. The increasingly frequent interactions of these atoms result in a larger number of atoms with perturbed energy states, leading to a spread of the wavelengths at which atomic transitions occur. As discussed earlier in Section 1.3, the pressure gradient in stellar interiors is closely related to the surface gravity of the star, demonstrated by Equation 1.6. Higher surface gravity in a star will result in higher pressures and densities in the photosphere, altering the shape of spectral line profiles as shown in Figure 1.6(b).

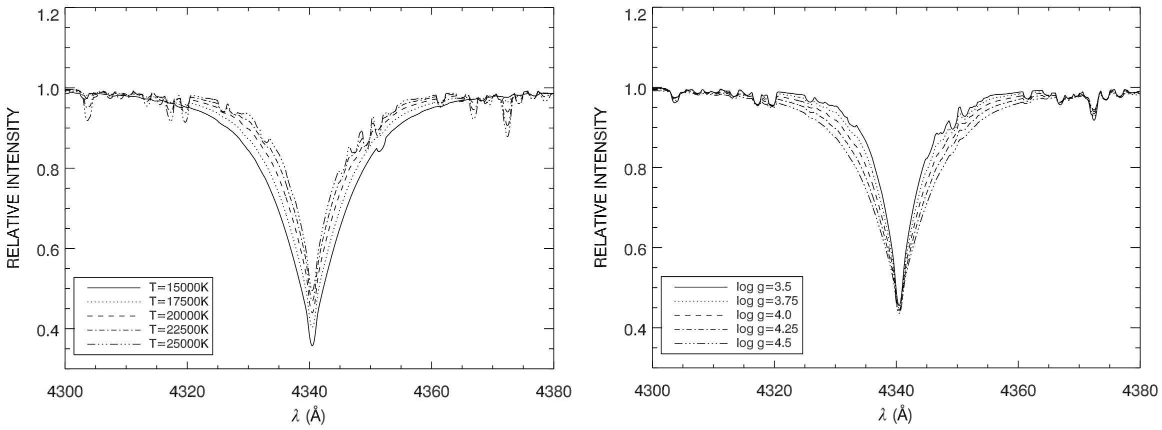

(a) Comparison of model spectra demonstrating the effect of $T_{\rm eff}$ on line profile shape due to changing ionization levels. Stacked model spectra (TLUSTY BSTAR2006 Lanz & Hubeny 2007) are shown for V sin i=50 km s^{-1}, log g=4.25, and varied $T_{\rm eff}$.

(b) Comparison of model spectra demonstrating the effect of log g on line profile shape. Stacked model spectra (TLUSTY BSTAR2006 Lanz & Hubeny 2007) are shown for V sin i=50 km s^{-1}, $T_{\rm eff}$=15000K, and varied log g.

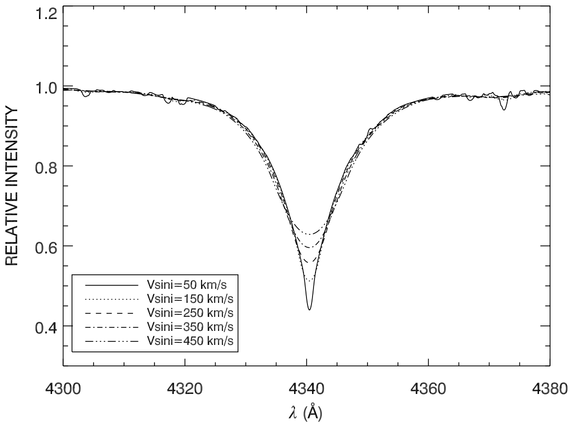

(c) Comparison of model spectra demonstrating the effect of V sin i on line profile shape. Stacked model spectra (TLUSTY BSTAR2006 Lanz & Hubeny 2007) are shown for $T_{\rm eff}$=15000K, log g=4.25, and varied V sin i.

Figure 1.6 Effects of $T_{\rm eff}$, log g, and V sin i on overall line profile shape.

Finally, Doppler rotational broadening is due to the bulk rotational motion of the star. As the gas of the photosphere co-rotates with the star, photons produced by the portion of the gas moving toward the observer's line of sight will have their wavelength blue-shifted, while those produced by gas moving away from the observer's line of sight will have their wavelength red-shifted. The overall effects of this broadening on line profile shape are demonstrated in Figure 1.6(c).

For non-rotating stars, the predominant contributors to the overall line profile shape are the natural, Doppler thermal, and pressure broadening mechanisms. Each contribution to the line profile shape can be described by a mathematical function of either Gaussian or Lorentzian form. Both natural and pressure broadening produce Lorentzian profiles, as they are produced by the oscillations of charged particles, while Doppler thermal broadening produces a Gaussian profile, as the distribution of particle velocities is Maxwell-Boltzmann in nature. These shapes are combined via the mathematical method of convolution, which is simply the multiplication of functions in Fourier space. The total line profile shape produced when all relevant intrinsic broadening mechanism contributions are combined is known as the Voigt profile. Figure 1.7 illustrates the differences between Lorentzian and Gaussian profiles, as well as how each contributes to the breadth and wings of the resultant Voigt profile shape.

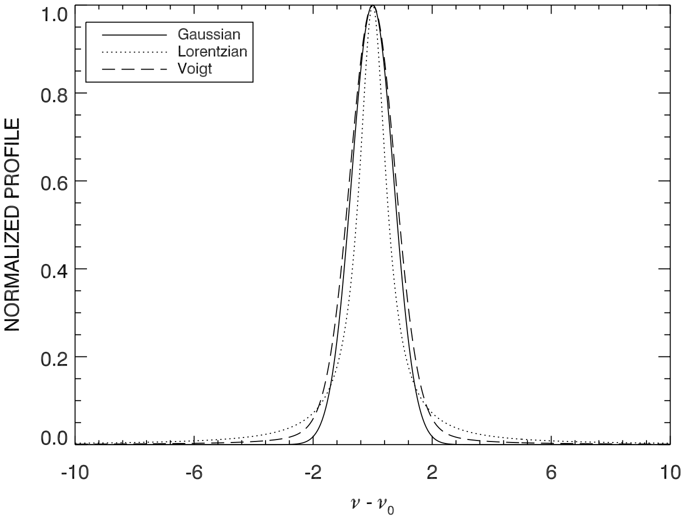

Figure 1.7 Normalized Gaussian, Lorentzian, and Voigt profile shapes.

Another major contributor to the width and shape of stellar spectral lines is the instrumentation used. As discussed in Section 1.2, spectroscopy utilizes a finely etched or blazed grating to disperse the light from a star so that it's intensity can be measured across a fine wavelength scale. In dispersing the light the spectrograph itself adds some additional broadening, as a function of wavelength, to the observed spectrum which must be accounted for before the spectrum can be used.

Measuring this instrumental broadening requires calibration of the spectrum via an emission lamp, which produce very narrow spectral lines. As the intrinsic widths of these lines are significantly small relative to the instrumental broadening, they are considered delta functions. The observed line width of this emission lamp spectrum can then be taken as the instrumental broadening. Emission lamps containing CuAr, HeNeAr, and ThAr are frequently used for this purpose in observational astronomy.

1.5.3 Physical Structures

While we often think of stars as being spherically symmetric, isolated, and that our observation of them is unimpeded, this is often not the case. Though there are numerous physical causes for the scattering or absorption of star light from our line of sight and for asymmetry in the profiles of spectral lines, two of the primary culprits are spherical outflows and rotating disk structures.

Spherical outflows are typical of more massive O- and early B-type stars on the main sequence, as well as evolved giant and supergiant stars. This outflow is a very strong, radiatively driven stellar wind which over time can carry away small fractions of the star's mass. The stellar wind is assumed to be spherically symmetric, with more or less equal expansion of the outer stellar envelope in all radial directions as illustrated by Figure 1.8. This envelope is composed of less dense, gaseous material that is cooler than the hot, dense core which is producing the driving radiation. The portion of this gaseous envelope that lies in front of the star, directly along an observer's line of sight will provide some absorption to the line profile, which is also Doppler shifted to shorter wavelengths as the material is moving toward the observer. The regions of the envelope that are to either side of the star contribute a central emission component to the line profile as the gaseous material is not back lit by the stellar core. The combined line profile observed is a readily recognizable

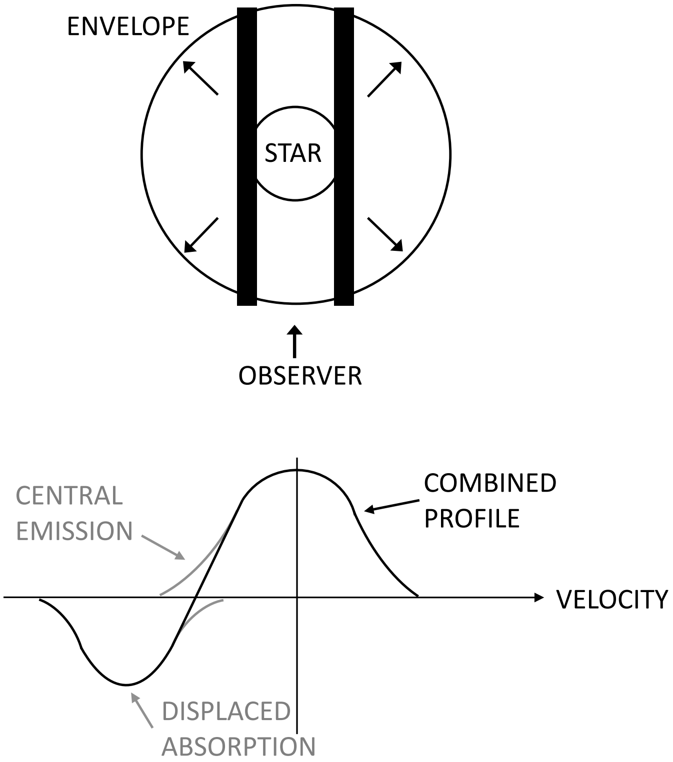

Figure 1.8 Line profile shape components for a spherical outflow.

"S" or P Cygni shape, with the intensity of absorption and emission components dependent upon the geometric size of the expanding envelope in comparison to the stellar photosphere [Conti & Leep, 1974].

Rotating disk structures are present at multiple stages of a star's evolution, and are crucial to a star's initial formation. For the purposes of this thesis, however, we will focus on those which are unique to some main sequence B-type stars, which are flattened, optically thin disks about the equatorial region of the star, composed mostly of hydrogen expelled from the photosphere of the star. There is an obvious disruption to the usual spherical symmetry in these B-type stars, which in tern impacts the overall shape of the hydrogen line profiles in these stars as illustrated in Figure 1.9. Along the observer's line of sight, the visible portion of the stellar photosphere contributes the expected hydrogen absorption, with some additional central absorption contributed by the front portion of the disk. Much like the case of a spherical outflow, the portions of the disk on either side of the star will contribute emission

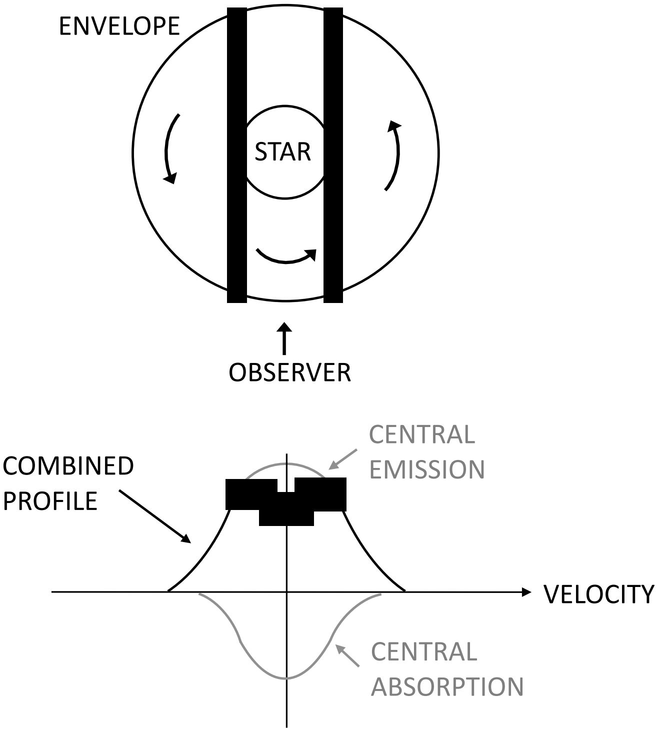

Figure 1.9 Be star line profile shape components.

proportional to the physical size of the disk. However, since these disks co-rotate with the central star, the contribution from the approaching side will be Doppler shifted to shorter wavelengths and the emission from the receding side will be shifted to longer wavelengths, splitting the emission component of the line. When all contributions are combined, the resulting line profile shape consists of a central absorption core with Doppler shifted emission peaks [Conti & Leep, 1974]. It should also be noted that with the lack of spherical symmetry, the wide range of inclinations an individual star + disk may exhibit will drastically alter the observed line shape as more or less of the disk surface area is visible to contribute emission.

1.6 Be Star Disk Structure

The modern working definition of a Be star is given as “a non-supergiant B star whose spectrum has or had at some time, one or more Balmer lines in emission”

[Porter & Rivinius, 2003]. While this general definition also encompasses objects such as the well known Algol binary systems and Herbig Ae/Be stars, classical Be stars are further delineated as having circumstellar line emission formed in an optically thin equatorial disk, low-order line profile variations, and rapid rotation [Porter & Rivinius, 2003]. These Be disks are comprised of warm gaseous material ejected from the stellar surface during outburst events. The gas is then pulled into a gravitationally bound orbit about the stellar equator.

It is well established that as a population, Be stars rotate faster than than their non-emission, B-type counterparts [Huang et al., 2010, McSwain et al., 2008, Porter & Rivinius, 2003]. Precisely why this is the case, however, is still debated. There are three primary theories as to why Be stars are rapid rotators: they may have been born as rapid rotators, spun up by mass transfer in a close binary system, or spun up during the main sequence evolution of B-type stars. The observed rotation rates of Be stars are $\geq$60–80% of their critical velocity [McSwain et al., 2008], at which point the gravitational and centrifugal forces are balanced, although recent results suggest that this threshold may be mass dependent [Huang et al., 2010]. The main sequence lifetimes of these objects are likely extended as a direct result of their rapid rotation, as this fosters rotational mixing of their stellar interiors and replenishes their hydrogen cores [Meynet & Maeder, 2000]. However, rapid rotation alone is not enough to spur the photospheric material of these stars to form the disk structures they host. It is likely that other weaker processes, such as non-radial pulsations (NRPs), are needed to provide the additional angular momentum necessary for this material to leave the stellar surface [Cranmer, 2009, McSwain et al., 2008, Porter & Rivinius, 2003, Rivinius et al., 2001]. A growing number of Be stars have been identified to exhibit NRPs (see Emilio et al. 2010, Rivinius et al. 2003).

While there is certainly some sort of temperature structure to the disks of Be stars, models typically make the assumption that the disks are isothermal as there is not yet a consensus as to what an appropriate profile should be. For investigating the bulk physical properties of the disk this assumption is sufficient and most models assume that the disk temperature T_d can therefore be related to the effective stellar temperature by $T_d = 0.6T_{\text{eff}}$ [Carciofi & Bjorkman, 2006]. In the remainder of this work, the disk model approach of Hummel & Vrancken [2000] is adopted. In this model approach the disk is assumed to be axisymmetric (symmetric about the vertical axis), and centered over the stellar equator.

To derive an expression for the disk density, we follow the Be disk theory detailed in Sigut et al. [2009]. A cylindrical coordinate system will be employed, where r and z are the radial and vertical cylindrical coordinates, respectively, given in units of stellar radii. We begin by assuming that at the equatorial plane ($z = 0$), the disk has a density ρ_0 which falls off with increasing radius as a power-law

$$\rho(r, 0) = \rho_0 (r)^{-n}. \tag{1.12}$$

Having established this definition of ρ with respect to radius, we now need to establish a similar definition with respect to the vertical coordinate in the disk, z. We assume that at a position in the disk equatorial plane the gas is in vertical hydrostatic equilibrium, and thus must satisfy the equation

$$\frac{dP}{dz} = -\rho g_z, \tag{1.13}$$

where the vertical component of the star's gravitational acceleration is given by

$$g_z = G M_\star \frac{z}{(r^2 + z^2)^{3/2}}. \tag{1.14}$$

Using the ideal gas law, we can then write Equation 1.13 in terms of density ρ. Grouping the physical constants and disk temperature into the coefficient α_0, which is a constant given our assumption of an isothermal disk, Equation 1.13 becomes

$$\frac{1}{\rho}\frac{d\rho}{dz} = -\alpha_0 \frac{z}{(r^2 + z^2)^{3/2}}. \tag{1.15}$$

Integrating this expression out to large distances above and below the disk gives

$$\log \rho = -\alpha_0 \left[\frac{1}{r} - \frac{1}{\sqrt{r^2 + z^2}} \right], \tag{1.16}$$

the right-hand side of which can be further reduced by utilizing the small angle approximation $z/r \ll 1$, and Taylor expanding the second term within brackets about z/r. Exponentiating both sides of this expression finally yields the needed expression describing the vertical disk density

$$\rho(z) = \rho_0 \exp\left(-\alpha_0 \frac{z^2}{2r^3}\right) = \rho_0 \exp\left(-\left(\frac{z}{H}\right)^2\right), \tag{1.17}$$

where the constants and radius r in the exponential term are collected to define the disk scale height $H(r)$

$$H(r) = \sqrt{\frac{2r^3}{\alpha_0}}. \tag{1.18}$$

Combining Equations 1.12 and 1.17, we arrive at an expression describing the radial and vertical structure of the disk density

$$\rho(r,z) = \rho_0 r^{-n} \exp\left[-\frac{1}{2}\left(\frac{z}{H(r)}\right)^2\right] \tag{1.19}$$

The disk base density at the stellar equator is given by ρ_0, n is the radial density exponent, and $H(r)$ is given by

$$H(r) = \frac{c_s}{V_K} r^{3/2}, \tag{1.20}$$

where V_K is the Keplerian velocity at the stellar equator, and c_s is the speed of sound, which is dependent on the disk gas temperature. The radial density exponent is usually set as $n = 3$ which is found to be typical of other observed Be star disks [Gies et al., 2007]. The disks are assumed to be in hydrostatic equilibrium vertically and horizontally. Generally speaking a scale height defines a distance over which a relevant quantity decreases by a factor of e (≈ 2.71828). In Be stars this relevant quantity is the disk density. An alternate means of expressing Be disk scale height is given by

$$H(r) = H_0 \left(\frac{r}{R_\star}\right)^\beta, \tag{1.21}$$

where

$$H_0 = \frac{a}{V_{crit}} R_\star, \tag{1.22}$$

$$a = \sqrt{\frac{kT}{\mu m_H}}, \tag{1.23}$$

and $\beta = 1.5$ for an isothermal disk [Bjorkman & Carciofi, 2005, Carciofi & Bjorkman, 2006]. Both expressions for disk scale height are physically the same, and commonly used to model the exponential fall off of the disk density in the vertical direction.

A substantial amount of variability is often observed in Be stars. Short term variations on the order of hours to days are seen in the surface brightness due to NRPs, and also in the line profiles as more dense clumps of material embedded in the disk structure co-rotate with the star [Rivinius et al., 1998]. Some of these line profile variations have been hypothesized to be large clumps of mass injected into the disk, which are slowly diffused outward and drawn out into spiral like arms due to the Keplerian rotation of the disk, termed "spiral density waves" [Porter & Rivinius 2003, and references therein]. Longer term variations (on time scales of months to years) are seen in the overall disk strength, and even the disk presence [eg. Grundstrom et al. 2011, McSwain et al. 2009]. A number of Be stars have been observed to lose their disks entirely for a period of time, and have them return later (termed transient Be stars) [McSwain et al., 2008, Porter & Rivinius, 2003]. While there is much active research being conducted in these areas, the driving mechanisms and physics behind these variations is still not well understood.

1.7 The Double Cluster: h & χ Persei

NGC 869 and NGC 884 (h and χ Persei, respectively) are a well known double open cluster, visible in the Northern hemisphere, and have been the focus of many studies over the years. The early 1900's saw a number of studies attempting to determine cluster membership, positions, and radial velocities [Adams & VanMaanen, 1913, Hertzsprung, 1922, Messow, 1913]. By the 1960's more extensive studies, such as that of Slettebak [1968], were being conducted to determine spectral types for the cluster constituents. More recently an extensive study has been conducted by Currie et al. [2010] in which they investigated the general properties and membership of the clusters. Their results, in agreement with those of Bragg & Kenyon [2005] and Slesnick et al. [2002], find that the clusters are incredibly similar, having common ages of ∼13–14 Myrs, distance moduli dM $= 11.8 - 11.85$ ($\sim 2,200$ pc), and reddenings of E$(B - V) \sim 0.52 - 0.55$. They also estimate a total mass of at least 20,000 $M_\odot$ for the clusters.

One of the prominent motivations for our study is that these young open clusters are rich in Be stars. As early as the 1920's, observational studies conducted by Trumpler [1926] and others noted the presence of emission in the hydrogen lines of many of the brightest B-type cluster members. Modern studies of the cluster have shown that upwards of 30% of the brightest B-type stars are known to be Be stars [Keller et al., 2001]. In a study conducted with *Spitzer*, Currie et al. [2008] investigated the lower mass stellar population for mid-infrared excesses due to the presence of protoplanetary disks. They also identified 57 Be stars and candidates exhibiting excess emission at 24μm, which helped to motivate our study to follow up these candidates and confirm their Be nature. Of their stars, 21 had previously been identified as showing emission, and 20 of their stars are included in the present study.

1.8 Outline of Dissertation

Through this work we seek to characterize the B-type and Be star populations of the Double Cluster, NGC 869 and NGC 884. Chapter 2 details the spectroscopic and photometric observations used to conduct this study. The process of determining physical parameters for these stellar populations is summarized in Chapter 3, along with the results of our analysis. In Chapter 4 we describe our use of spectral energy distributions (SEDs) as a check of our parameter determinations and to determine distances to the stars in our sample. Chapter 5 details the processes for estimating Be disk radius and density via H_α line strength, and predicting the infrared flux contribution of the Be disk. Finally in Chapter 6, we draw our final conclusions from this study and outline future work needed to further the results of this investigation.

Chapter 2

Observations

In the following work, both photometric and spectroscopic data were used to investigate different physical aspects of the B-type and Be star samples. The following section contains details regarding the different instrumentation used to collect data for this work, and the methods by which the data were reduced to their final form.

2.1 Spectroscopy

We have obtained spectra for a total of 104 members of NGC 869 and NGC 884 during multiple observing runs: 2005 November using the Kitt Peak National Observatory (KPNO) Wisconsin Indiana Yale NOAO (WIYN) 3.5 m telescope with the Hydra multifiber spectrograph; 2010 August using the Wyoming Infrared Observatory (WIRO) 2.3 m telescope with the Long Slit spectrograph; 2011 November using the KPNO 2.1 m telescope with the GoldCam spectrograph; and 2012 January using the 0.9 m KPNO Coudé Feed (CF) telescope with the Coudé spectrograph. The UT dates, wavelength range, resolving power, number of targets, and instrumental setup details for all runs are summarized in Table 2.1.

Table 2.1 Journal of Spectroscopy

UT Dates	Range (Å)	Resolving Power ($\lambda/\Delta\lambda$)	Number of Targets	Telescope	Spectrograph	Grating	Order	Filter	Camera	Detector
2005 Nov 14–15	4250–4900	4700	92	WIYN 3.5m	Hydra	1200@28.7	2	BG39	Red bench, blue fibers	5TA1
2009 Oct 16–18	4000–5200	1400	16	WIRO 2.3m	Long Slit	LS-1	2	BG40	—	SBIG-ST-2000
2009 Oct 16–18	5350–6810	4500	13	WIRO 2.3m	Long Slit	LS-2	1	GG455	—	SBIG-ST-2000
2009 Dec 4–5	4000–5200	1400	5	WIRO 2.3m	Long Slit	LS-1	2	BG40	—	SBIG-ST-2000
2009 Dec 10	5350–6810	4500	10	WIRO 2.3m	Long Slit	LS-2	1	GG455	—	SBIG-ST-2000
2010 Aug 23–27	4000–5200	1600	2	WIRO 2.3m	Long Slit	LS-1	2	BG40	—	SBIG-ST-2000
2010 Aug 28–31	5350–6810	4500	6	WIRO 2.3m	Long Slit	LS-2	1	GG455	—	SBIG-ST-2000
2011 Nov 10–13	4000–5200	2300	3	KPNO 2.1m	GoldCam	47	2	CuSO4, WG354	Gold	F3KC
2011 Nov 5–6	5900–7200	1900	3	KPNO 2.1m	GoldCam	56	2	—	Gold	F3KC
2012 Jan 3–8	4090–4550	7800	2	KPNO CF	Coudé	B	3	4-96	Cam5	T2KB
2012 Jan 3–8	6320–7025	11700	9	KPNO CF	Coudé	B	2	OG-55	Cam5	T2KB
2012 Aug 27–29	5600–6800	2700	24	WIRO 2.3m	Long Slit	2000l/mm	1	GG455	—	SBIG-ST-2000
2012 Aug 30–Sep 3	3900-5000	2600	20	WIRO 2.3m	Long Slit	2000l/mm	2	BG40	—	SBIG-ST-2000

2.1.1 WIYN

The WIYN 3.5m telescope is a ground-based optical observatory located at KPNO, outside of Tucson, AZ. It is equipped with the Hydra multi-fiber spectrograph, which is capable of taking up to 100 simultaneous spectra of objects in a given field of view. The telescope is owned and operated by the WIYN Consortium. All of the spectra obtained at the WIYN 3.5 m with the Hydra spectrograph have been zero corrected using standard routines in IRAF[4], and have been flat-fielded, wavelength-calibrated, and sky-subtracted in IRAF using the **dohydra** routine. The Hydra observations obtained by M. Virginia McSwain in 2005 consist of 7 exposures of NGC 869, totaling 2.25 hrs, and 5 exposures of NGC 884, totaling 2 hrs. Each exposure has been wavelength calibrated with a CuAr comparison spectrum both before and after the cluster observations. For each of the two configurations, the exposures have been transformed to a common heliocentric wavelength grid and co-added to produce good signal-to-noise for each star. The spectra were rectified to a unit continuum by fitting line-free regions.

2.1.2 WIRO

WIRO is a classical Cassegrain telescope with a 2.3m aperture that is optimized to make ground based photometric and spectroscopic observations in the near-IR and optical wavelength regions. The telescope is owned and operated by the University of Wyoming and is located atop Mt. Jelm, outside of Laramie, WY. Before any reduction or calibration routines were applied to WIRO data, all spectra (object and comparison) were corrected for bit-flip errors with the **rfits** routine in IRAF. These errors are inherent to the CCD used in this instrument. A CuAr calibration lamp source was used to obtain wavelength calibration spectra before and after every object spectrum. The spectra were then zero-corrected, flat-fielded, wavelength-calibrated, and rectified to a unit continuum using standard slit spectra routines in IRAF. Fainter objects that required multiple exposures were co-added prior to continuum rectification to improve signal-to-noise.

---

[4] IRAF is distributed by the National Optical Astronomy Observatory, which is operated by AURA, Inc., under cooperative agreement with the NSF.

2.1.3 KPNO 2.1m

The KPNO 2.1m Cassegrain telescope has been in operation since 1964, and was one of the earliest telescopes at Kitt Peak. Both imaging and spectroscopic instruments are available for public use in the optical and IR regimes. Spectra from the KPNO 2.1 m instrument have been zero-corrected, flat-fielded, and wavelength-calibrated using the standard routines found in IRAF. Once wavelength calibrated via the HeNeAr comparison lamp spectra, which were taken before and after every object spectrum, the data were rectified to a unit continuum.

2.1.4 KPNO Coudé Feed

The KPNO CF telescope is a unique instrument. The room-sized spectrograph was originally designed to be used in conjunction with the 2.1m telescope, but has since been modified to be used as an independent instrument with a 0.9m aperture mirror that is mounted on the roof of the spectrograph room. In a similar manner to the data gathered with WIRO and the KPNO 2.1m, the spectra obtained with the KPNO CF telescope have been zero-corrected, flat-fielded, and wavelength-calibrated using the standard routines in IRAF. ThAr comparison spectra were taken every one to two hours during the run. The data were then rectified to a unit continuum.

2.2 Photometry

We have also gathered photometry of NGC 869 and NGC 884 members via a number of publications and online databases. Details of all photometry we have used are summarized in Table 2.2. The Strömgren photometric measurements are used to determine T_{eff} and log g for the cluster Be stars, while the remaining photometry are used in our analysis of the Be star disk radii and masses via the SEDs of the star+disk system. The reminder of this section details the process of converting the reported instrumental magnitudes to fluxes and the specifics of each filter system.

A simple relationship between the apparent magnitude and flux of two objects is

Table 2.2. Photometric Catalogs

Filter System	**Central Wavelengths**	**Reference**
Strömgren *uvby*	350/411/467/547 nm	WEBDA[a]
Johnson *UBV*	364/442/540 nm	WEBDA[a]
2MASS JHK_s	1.25/1.65/2.15 μm	Skrutskie et al. [2006]
WISE	3.4/4.6/12/22 μm	Wright et al. [2010]
Spitzer IRAC	3.6/4.5/5.8 μm	Currie et al. [2007]
Spitzer IRAC	8 μm	Currie et al. [2008]
AKARI	8.61/18.39 μm	Ishihara et al. [2010]
Spitzer MIPS	24 μm	Currie et al. [2008]

[a] http://www.univie.ac.at/webda/navigation.html

given by the following expression,

$$m_1 - m_2 = -2.5 \log \frac{F_1}{F_2}. \tag{2.1}$$

Rearranging the above expression, we can determine the flux of a particular star by comparison to a second object with a well established flux and magnitude in a particular waveband, and measuring the unknown star's magnitude in this same waveband

$$F_1 = F_2 \times 10^{-0.4(m_1 - m_2)}. \tag{2.2}$$

To standardize any of the many photometric systems, the flux of a theoretical object with an apparent magnitude of 0 in each filter is taken as the zero-magnitude flux density, $F_{\lambda,zero}$. Making these substitutions into Equation 2.2,

$$F_{\lambda,obj} = F_{\lambda,zero} \times 10^{-0.4(m_\lambda)}, \tag{2.3}$$

the observed flux density of an unknown object, $F_{\lambda,obj}$, can be derived. The typical units associated with F_λ are erg s^{-1} cm^{-2} Å^{-1} (cgs units). The reported values of $F_{\lambda,zero}$ and $\lambda_{central}$ needed to make the above magnitude-to-flux conversion for the photometric systems used in our analysis are given in Table 2.3, along with the full-width half-maximum (FWHM) (effective filter width) of each filter.

Table 2.3 Photometric Filter Specifications

Filter System	**Filter**	$\lambda_{central}$ (Å)	**FWHM** (Å)	$F_{\lambda,zero}$ (erg s^{-1} cm^{-2} $Å^{-1}$)
Strömgren	u	3491	300	11.72×10^{-9}
	v	4111	190	8.66×10^{-9}
	b	4662	180	5.89×10^{-9}
	y	5456	230	3.73×10^{-9}
Johnson	U	3735	660	4.34×10^{-9}
	B	4443	940	6.40×10^{-9}
	V	5483	850	3.67×10^{-9}
2MASS	J	12350	1620	3.129×10^{-10}
	H	16620	2510	1.133×10^{-10}
	K_s	21590	2620	4.283×10^{-11}
WISE	3.4 μm	33526	6600	8.17976×10^{-12}
	4.6 μm	46028	10400	4.55190×10^{-12}
	12 μm	115608	55100	7.74679×10^{-13}
	22 μm	220883	41000	2.20947×10^{-13}
Spitzer IRAC	3.6 μm	35500	7500	6.68209×10^{-12}
	4.5 μm	44930	10150	2.66865×10^{-12}
	5.8 μm	57310	14250	1.04967×10^{-12}
	8 μm	78720	29050	3.10247×10^{-13}
Spitzer MIPS	24 μm	2367580	47000	3.83492×10^{-15}
AKARI	9 μm	86100	41000	2.27515×10^{-13}
	18 μm	183900	99700	1.06374×10^{-14}

2.2.1 Strömgren

The Strömgren photometric system includes narrow-band filters covering the optical region of the electromagnetic spectrum. With such narrow bands, the Strömgren system allows for photometric sampling of specific areas of a stellar spectrum. This property will be utilized later in Chapter 3, as line-less continuum regions in the spectra of massive stars are well sampled by the b and y bands.

Strömgren photometic observations are often reported as a set of indices (b-y, m_1, and c_1) and y magnitude. The indices m_1 and c_1 are given by

$$\begin{aligned} m_1 = &\quad (v-b)-(b-y) \qquad (2.4) \\ c_1 = &\quad (u-v)-(v-b). \qquad (2.5) \end{aligned}$$

Using the expressions given in Equations 2.6 – 2.8, the remaining magnitudes can be recovered.

$$\begin{aligned} b = &\quad y+(b-y) \qquad (2.6) \\ v = &\quad m_1+(b-y)+b \qquad (2.7) \\ u = &\quad c_1+2(v-b)+b. \qquad (2.8) \end{aligned}$$

The H_β wide and narrow filters sample the second of the hydrogen Balmer lines, centered at 4861 Å, and together yield the β index

$$\beta = m_{narrow} - m_{wide} \qquad (2.9)$$

which provides an effective equivalent width of the H_β line. In this expression m_{narrow} designates the narrow band magnitude, and m_{wide} designates the wide band magnitude.

Shown in Figure 2.1 are the normalized spectral response curves for a standard set of *uvby* filters. Plotted above the response curves is a model spectrum of a $T_{\mathrm{eff}} = 15000$ K and log $g = 3.80$ dex B-type star, from the TLUSTY BSTAR2006 grid of model spectra [Lanz & Hubeny, 2007], illustrating the specific spectral regions sampled by each of the Strómgren filters.

2.2.2 Johnson

The Johnson photometric system includes wide-band filters in the near-ultra-violet and optical spectral regions. The calibration of this system, as detailed by Colina et al. [1996], is derived from setting the UBV magnitudes of Vega to zero. This calibration reports errors in the determined zero-magnitude fluxes of order $5-6\%$. The UBV magnitudes used in this work were gathered from the WEBDA database. As there are multiple values reported for each band from several sources, we have averaged the

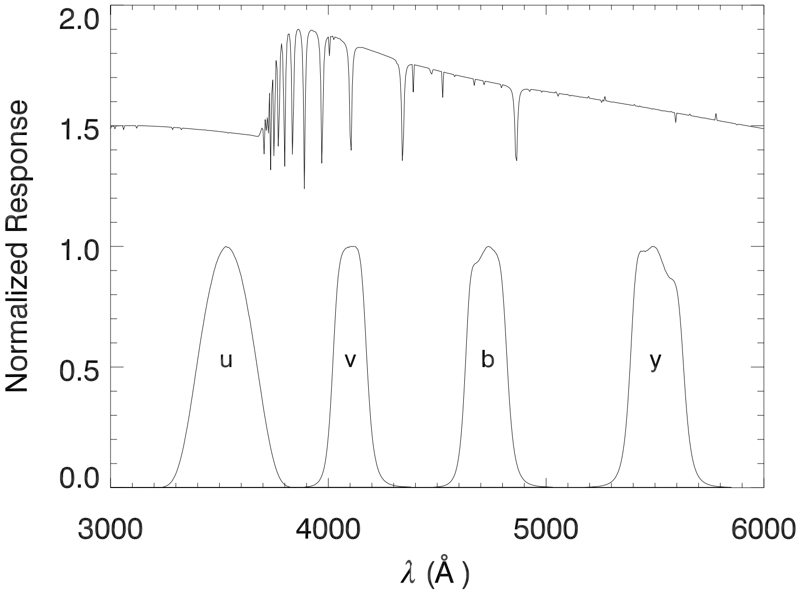

Figure 2.1 Strömgren *uvby* normalized spectral responses as determined for the 4” x 4” Strömgren filters at KPNO. The binned spectrum of a model B-type star of $T_{\text{eff}} = 15000$ K and log $g = 3.80$ dex (TLUSTY BSTAR2006 Lanz & Hubeny 2007) is plotted with the Strömgren filters, illustrating the regions each samples.

reported values together and removed any observations lying more than one standard deviation outside of this mean value. Shown in Figure 2.2(a) are the calculated normalized spectral response curves for a standard set of UBV filters. These curves demonstrate the wide sampling regions of these filters, and their relative transmission [Colina et al., 1996].

2.2.3 2MASS

The Two Micron All Sky Survey (2MASS) is an extensive ground-based near-infrared (near-IR) photometric survey, conducted by the University of Massachusetts and the Infrared Processing and Analysis center at JPL/Caltech. The survey was conducted with two 1.3 m aperture automated telescopes, one in each the Northern and Southern hemispheres, which scanned 99.998% of the sky in three near-IR bands between 1997 and 2001 [Skrutskie et al., 2006]. The complete all-sky data release can be accessed and searched via the online NASA/IPAC Infrared Science Archive (IRSA). Further details of the survey data calibrations can be found in Cohen et al. [2003]. Shown in Figure 2.2(b) are the normalized spectral response curves for the JHK_s bands as determined by the 2MASS calibration team.

2.2.4 *Spitzer*

Spitzer is a space-based infrared telescope, launched in 2003 and operated by NASA. The mission consists of three primary instruments, the Infrared Array Camera (IRAC), the Multi-Band Imaging Photometer for Spitzer (MIPS), and the Infrared Spectrograph (IRS). Both the IRAC and MIPS provide photometry covering the near- to mid-IR spectral regions, while the IRS provides low resolution spectroscopy between $5.2 - 38$ μm. At the time of the writing of this thesis *Spitzer* is still functioning and taking observations. However, the cryogenic coolant onboard has been depleted, leaving only the IRAC instrument available for continued use during the remaining "warm" phase of the mission. As with 2MASS, *Spitzer* data is available for use through the online IRSA database. Details regarding the calibration of IRAC data can be found in Reach et al. [2005], and similar specifications for MIPS data can be found in Rieke et al. [2008]. The *Spitzer* observations used in this work were gathered from the Currie et al. [2007] (IRAC 3.6 μm, 4.5 μm, 5.8 μm) and Currie et al. [2008] (IRAC 8 μm, MIPS 24 μm) surveys of NGC 869 and NGC 884. Shown in Figures 2.2(c) and 2.2(d) are the normalized spectral response curves for both the *Spitzer* IRAC and MIPS filters used in this work.

2.2.5 *WISE*

The Wide-field Infrared Survey Explorer (*WISE*) is another space-based infrared telescope operated by NASA, launched in late 2009. Further details regarding the calibration of WISE data can be found in Wright et al. [2010]. The complete all-sky data release can be accessed and searched via the online NASA/IPAC Infrared Science Archive (IRSA). Shown in Figure 2.2(e) are the normalized spectral response curves for the *WISE* filters. In our initial investigation of the *WISE* photometry, we found the 22 μm band magnitudes to be systematically too high for those of our objects observed by the mission, thus we have excluded them in our analysis.

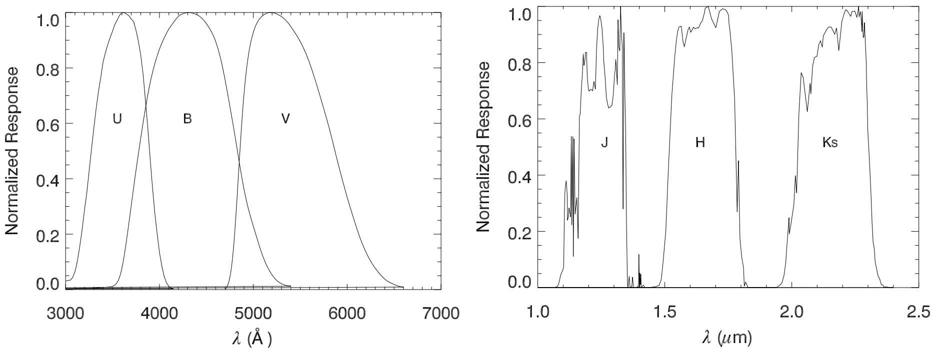

(a) Johnson UBV filter system.

(b) 2MASS filter system.

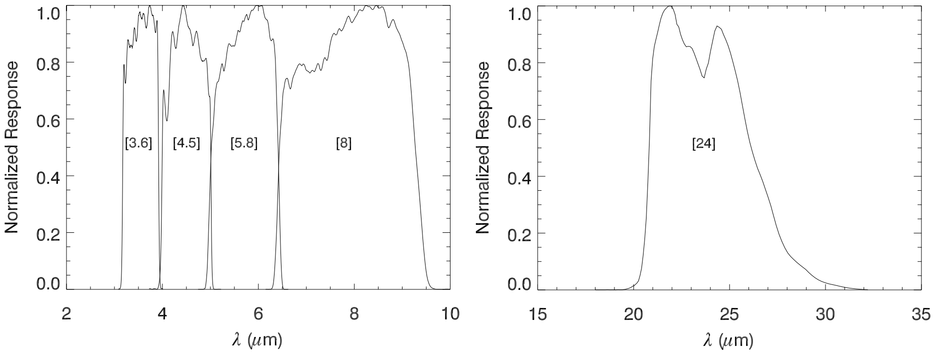

(c) *Spitzer* IRAC 3.6/4.5/5.8/8 μm filters.

(d) *Spitzer* MIPS 24 μm filter.

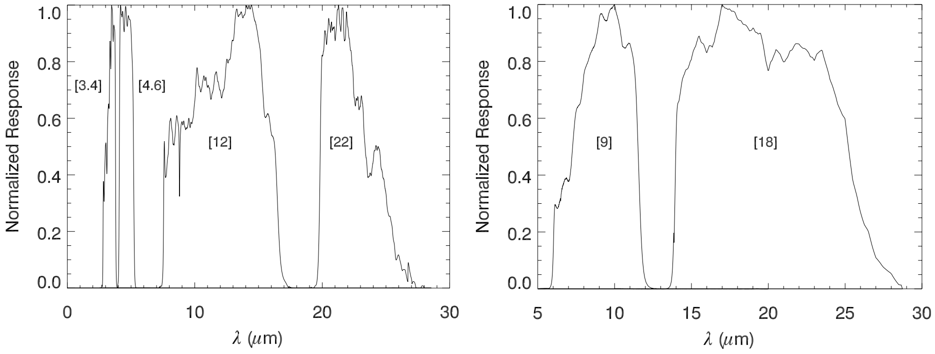

(e) *WISE* filter system.

(f) *AKARI* 9 and 18 μm filters.

Figure 2.2 Normalized spectral response curves for the various filter systems used in this work for SED fitting.

2.2.6 *AKARI*

AKARI, much like *Spitzer* and *WISE*, is a space-based infrared telescope launched and operated by the Japanese Space Agency. Over the course of 18 months, starting in 2006 after its launch, *AKARI* surveyed 94% of the sky, observing across the near-, mid-, and far-IR spectral regions. The satellite carries two instruments, the Infrared Camera (IRC), and the Far-Infrared Surveyor (FIS). The all-sky survey conducted by the satellite utilized the 9 μm and 18 μm filters of the IRC, and the 65 μm, 90 μm, 140 μm, and 160 μm filters of the FIS. For the remainder of this work, only the 9 μm and 18 μm bands will be utilized, and further details regarding the calibration of these observations can be found in Ishihara et al. [2010].

2.3 Precision vs. Accuracy

With any experimentally measured quantity, both the precision and the accuracy of a measurement must be determined in order to gauge it's reliability. Often in everyday conversation these two descriptors are used interchangeably, however, this is incorrect. Precision and accuracy refer to two different measures of error in a measurement. Generally speaking, precision is the repeatability of a measurement, i.e. how close are the resulting numbers if you make the same measurement multiple times. Accuracy is how close a measurement comes to the absolute or true value of a measured quantity.

Determining the precision of different aspects of our analysis requires careful determination of the error being contributed by each parameter in a fit, or possible inaccuracy in a measurement device. In processing our raw data and preparing it for use, we carefully remove erroneous "noise" added to our observations by the wavelength dependent response the CCD detector and the underlying electronic current that powers it. In our fitting routines, which will be described in detail in Chapter 3, we must determine appropriate error bars that account for any imperfections in the fit of our observed stellar spectral line to that produced by a comparable stellar model. The error bars we report are derived by minimizing the χ^2 residual fit of our observations to the model. Our determination of V sin i requires a one parameter fit. This means that an appropriate model is selected by $T_{\rm eff}$ and log g, and different amounts of rotational broadening are incrementally applied to the stellar spectrum. At each step the observed and model fluxes, $F_{\lambda,obs}$ and $F_{\lambda,mod}$ respectively, are compared and normalized across the wavelength region being fit

$$\chi^2 = \sum_{\lambda=1}^{n} \left(\frac{F_{\lambda,obs} - F_{\lambda,mod}}{F_{\lambda,mod}} \right)^2 , \tag{2.10}$$

giving a measure of how well the data is fit by the model, χ^2. The value of V sin i which gives the smallest χ^2 is taken as the resultant fit value, and the reported errors are determined from the offset from this best fit value that increases the rms^2 by 2.7rms$^2/N$, where N is the number of wavelength points within the fit region. Similar two parameter χ^2 residual fits are used to simultaneously determine $T_{\rm eff}$ and log g. Similar incremental steps are taken to vary $T_{\rm eff}$ and log g while honing in on a minimum residual value and adequate error bars.

Gauging the accuracy of the various measurements we make in our analysis requires us to compare them closely with analogous measurements by other studies, or to re-measure the same parameters by different techniques. In our analysis we utilize both of these stratagies as appropriate to determine the accuracy of our measurements. There are two other studies which have measured physical parameters of many of our sample B-type and Be stars. One uses a spectroscopic modeling technique very similar to ours, but different model stellar atmospheres to determine V sin i, $T_{\rm eff}$, and log g for sample stars. The second uses photometry, rather than spectroscopy, to derive $T_{\rm eff}$. Agreement between the resultant parameters for stars common to these studies and our own lends further credence to our results being the "true" values of V sin i, $T_{\rm eff}$, and log g for these stars, and the robustness of our methods. Any discrepancies provide insight into physical differences between models and the stars they represent, or assumptions made that may not be as correct as thought. In Chapter 4 we utilize two independent means of deriving distances to our sample stars, which we then compare to the known distances to the clusters. While these derivations of distance are not as precise as those used to determine the accepted cluster distances, the agreement in the results again gives us confidence in our measurements.

Chapter 3

Determination of Physical Parameters

In order to dive into the details of the Be star disks in our sample, we must first determine what sort of stars we are considering in our sample. To determine the physical characteristics of each star requires careful measurement of physical parameters like V sin i, $T_{\rm eff}$, and log g. Determining these quantities for normal B-type stars will provide a baseline for measuring the same for the stars hosting disks. By carefully determining $T_{\rm eff}$ and log g for our sample Be stars, we will be able to isolate the flux contributions from the Be stars and their disks later in Chapter 5.

There is an on-going debate in the massive star community regarding the evolution of angular momentum of B-type stars. With their abundance of B-type stars, h and χ Per are two of the many stellar clusters at the center of this debate. Strom et al. [2005] find that the present-day rotation rates of these stars are set by environmental characteristics of the natal clouds in which they formed, with little change over the main sequence stellar lifetime. The work of Huang & Gies [2006a] and Huang et al. [2010], however, indicates that the observed rotation rates of B-type stars are due less to the initial birth-line rotational rates of the stars and more to evolutionary spin-down or mass transfer in binaries. Both studies also observe that B-type stars in clusters have, on average, significantly higher rotation rates than field B-type stars. Resolving the angular momentum problem also requires a new examination of the stellar parameters and evolutionary states, which the analysis described in this chapter endeavors to provide for the stars of h and χ Per. The analysis and results detailed in this chapter have been published in Marsh Boyer et al. [2012].

3.1 Spectral Model Fitting for B-type and Non-emission Be Stars

The first component of our population study is to determine basic parameters for the cluster constituents using a methodology devised by McSwain et al. [2008]. Using ground based optical spectroscopy (4000–5200 Å) and model fitting techniques, we can determine V sin i, $T_{\rm eff}$, and log g for each star. To obtain these measurements, we compare our observed spectra to grids of model B-type stars, determining a best fit to the data by minimizing the mean square of the deviations rms^2.

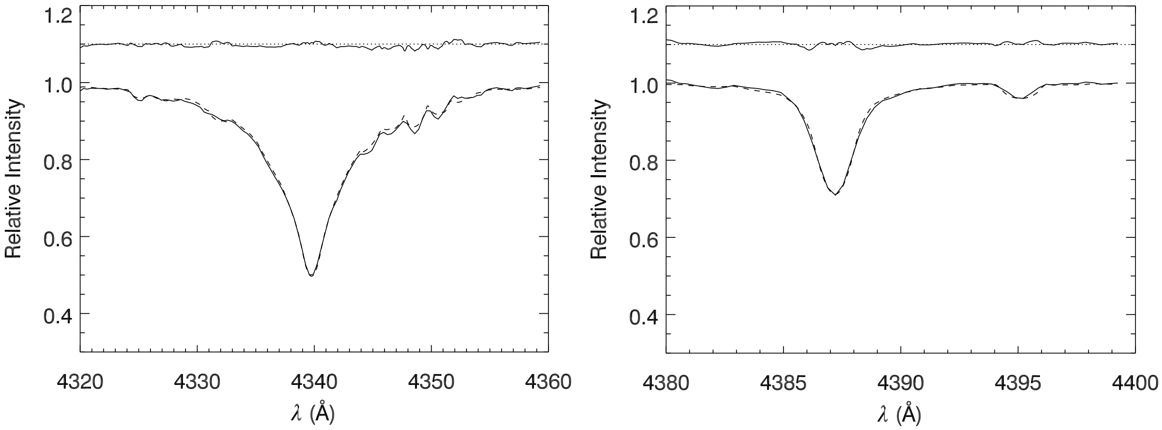

Figure 3.1 Sample spectral line fits for NGC 869-90. Shown on the left is Hγ and on the right is He I λ4378. The solid line is our observed spectrum while the dashed line displays our model fit to the line, with the computed residual shown above, shifted for clarity.

We begin our analysis by making a rough estimate of $T_{\rm eff}$ and log g for a star, and then we compare the He I $\lambda\lambda$4387, 4471, 4713, and Mg II λ4481 lines with the Kurucz ATLAS9 models [Kurucz, 1994] to determine V sin i. These lines are used because their broadening is dominated by the effects of rotation, thus yielding a better indication of V sin i. We then take a weighted average of the four values determined from each of the lines to give our measured value of V sin i. The error, ΔV sin i, is determined by the offset from the measured best-fit value that increases the rms^2 by $2.7\mathrm{rms}^2/N$. Here, N is the number of wavelength points within the fit region. A sample fit determined for He I $\lambda4387$ in NGC 869–90 is shown in the right panel of Figure 3.1. Our results for $V \sin i$ and its errors are listed in columns 2 and 3 of Tables 3.1 and 3.2.

In Be stars it is possible that the He I lines may contain weak emission from the circumstellar disk, which may partially fill the absorption features and narrow the overall line profile. So while we have made measurements of $V \sin i$ where we can for Be stars in our sample, these values should be considered as lower limits.

We measure a mean $V \sin i$ =157 km s^{-1} with a standard deviation of 89 km s^{-1} for the normal B-type stars of both clusters, including binary systems. Assuming an average inclination angle of $i = 60^o$, this gives a mean $V_{\mathrm{eq}} = 181$ km s^{-1} for our sample of B stars. For the Be stars we measure a mean $V \sin i = 205 \pm 81$ km s^{-1}, with a mean $V_{\mathrm{eq}} = 237$ km s^{-1}. From this it is clear that the Be stars in these clusters are, on average, rotating somewhat more rapidly than their B-type counterparts. In comparison to other young open clusters (see McSwain et al. 2009, 2008), we find that the Be star population of NGC 869 and NGC 884 are rotating surprisingly more slowly that expected in comparison to their B-type counterparts. The cumulative $V \sin i$ distributions for all Be and normal B-type stars in both NGC 869 and NGC 884 are shown in Figure 3.2. Using the two-sided Kolmogorov-Smirnov (K-S) statistical test, we investigate the null hypothesis that the distributions of B-type and Be stars differ. The K-S test indicates a 7.6% chance that the two populations are drawn from the same sample.

Table 3.1. Physical Parameters of B-type Cluster Members

WEBDA ID (1)	V **sin** i **(km s^{-1})** (2)	ΔV **sin** i **(km s^{-1})** (3)	$T_{\rm eff}$ **(K)** (4)	$\Delta T_{\rm eff}$ **(K)** (5)	**log** g **(dex)** (6)	Δ **log** g **(dex)** (7)	**log** $g_{\rm polar}$ **(dex)** (8)	$M_\star$ ($M_\odot$) (9)	$\Delta M_\star$ ($M_\odot$) (10)	$R_\star$ ($R_\odot$) (11)	$\Delta R_\star$ ($R_\odot$) (12)
NGC 869											
63[a]	151	8	21800	250	3.81	0.02	3.92	8.7	0.1	5.4	1.7
87	89	16	10060	60	3.83	0.03	3.92	2.8	0.1	3.0	0.3
90	64	6	22350	50	3.65	0.02	3.68	10.7	0.1	7.8	1.4
133[a]	341	19	17500	200	3.92	0.02	4.22	5.4	0.1	3.0	1.2
138	97	12	19400	200	3.93	0.02	3.99	6.9	0.1	4.4	1.3
197	262	25	10340	51	3.89	0.03	4.13	2.6	0.1	2.3	0.1
250	109	25	17750	50	4.00	0.02	4.07	5.9	0.1	3.7	1.1
260	198	13	25200	200	3.33	0.02	3.54	14.9	0.3	10.8	2.0
289	66	10	20100	100	3.95	0.02	3.98	7.4	0.1	4.6	1.4
323[a]	50	7	20700	300	3.78	0.03	3.80	8.6	0.2	6.1	1.2
339	76	7	27000	1000	3.55	0.07	3.58	17.2	1.5	11.1	3.0
350	136	4	18450	50	3.90	0.02	4.00	6.4	0.1	4.2	1.1
380	112	6	19150	50	4.00	0.02	4.07	6.6	0.1	3.9	1.3
530[a]	59	9	24100	350	3.95	0.03	3.97	10.5	0.3	5.5	2.4
551[a]	220	11	20200	350	3.63	0.03	3.83	8.1	0.2	5.7	1.2
590	119	10	24050	50	3.75	0.02	3.82	11.2	0.2	6.8	2.2
662	67	11	24300	650	3.13	0.05	3.17	20.0	1.7	19.2	1.4
678	100	15	22950	50	3.60	0.02	3.67	11.3	0.1	8.1	1.6
692	176	16	25400	400	3.38	0.03	3.55	15.0	0.6	10.7	2.1
731[a]	165	11	21600	250	3.94	0.02	4.05	8.2	0.1	4.5	1.8
748	251	35	10900	78	3.61	0.03	3.89	3.1	0.1	3.3	0.2
768	45	6	17600	200	3.48	0.02	3.51	7.7	0.1	8.1	0.4
769	127	8	22650	50	3.75	0.02	3.84	9.9	0.1	6.3	1.8
789	199	16	17250	50	4.00	0.02	4.15	5.4	0.1	3.2	1.1
803	265	19	23100	150	3.49	0.03	3.75	10.9	0.1	7.3	1.8
843[a]	113	7	21800	100	3.40	0.02	3.50	11.4	0.1	9.9	0.8
859	221	9	22000	400	3.73	0.02	3.91	8.9	0.2	5.5	1.7
864	150	45	22800	400	3.73	0.02	3.84	10.1	0.4	6.3	1.9
922	270	14	25300	300	3.34	0.02	3.62	14.2	0.3	9.6	2.3
1001	61	4	22900	100	3.60	0.02	3.63	11.5	0.1	8.6	1.4
1067[a]	63	8	21800	300	3.72	0.02	3.75	9.6	0.3	6.8	1.4
1078	208	24	24950	50	3.50	0.02	3.69	13.1	0.1	8.6	2.2
1085	88	5	22200	100	3.50	0.02	3.57	11.3	0.1	9.2	1.1

Table 3.1 (cont'd)

WEBDA ID (1)	V **sin** i **(km s^{-1})** (2)	ΔV **sin** i **(km s^{-1})** (3)	$T_{\rm eff}$ **(K)** (4)	$\Delta T_{\rm eff}$ **(K)** (5)	**log** g **(dex)** (6)	Δ **log** g **(dex)** (7)	**log** $g_{\rm polar}$ **(dex)** (8)	$M_\star$ ($M_\odot$) (9)	$\Delta M_\star$ ($M_\odot$) (10)	$R_\star$ ($R_\odot$) (11)	$\Delta R_\star$ ($R_\odot$) (12)
1132	103	7	24300	450	3.18	0.02	3.27	17.9	0.8	16.2	0.9
1141	233	14	20700	150	3.20	0.02	3.49	10.4	0.1	9.6	0.4
1174	65	9	19300	200	3.93	0.02	3.96	6.9	0.1	4.5	1.2
1181	71	6	17300	200	3.97	0.03	4.01	5.9	0.1	4.0	1.0
1364	235	12	20900	150	3.40	0.02	3.66	9.4	0.1	7.5	0.9
1387	79	4	20500	100	3.85	0.02	3.90	8.1	0.1	5.3	1.4
1391	161	9	22300	100	3.55	0.02	3.69	10.6	0.1	7.7	1.4
1482	101	59	10740	72	3.47	0.03	3.61	3.5	0.0	4.9	0.9
1516^{a}	152	17	25400	650	4.24	0.05	4.29	9.9	0.5	3.7	0.2
1548	195	14	13300	171	4.12	0.04	4.23	3.5	0.1	2.4	0.6
NGC 884											
1770	232	7	17650	50	3.75	0.02	3.97	6.2	0.1	4.3	1.0
1793	136	30	–	–	–	–	–	–	–	–	–
1873^{a}	166	8	21600	300	3.83	0.02	3.95	8.5	0.2	5.1	1.7
1899	137	7	23500	700	3.16	0.05	3.31	15.9	1.3	14.6	0.6
2014^{a}	293	8	19000	250	3.64	0.03	3.93	6.9	0.1	4.7	1.1
2048	100	6	19400	250	3.92	0.02	3.98	6.9	0.1	4.4	1.2
2049	413	28	18050	50	2.75	0.02	3.61	7.5	0.1	7.1	0.2
2057	151	10	19450	50	3.80	0.02	3.92	7.2	0.1	4.9	1.1
2085	284	9	19000	250	3.54	0.02	3.85	7.1	0.2	5.3	0.9
2086	146	34	–	–	–	–	–	–	–	–	–
2094	80	3	20350	50	4.00	0.02	4.04	7.4	0.1	4.3	1.6
2112	89	8	22300	150	3.80	0.02	3.85	9.4	0.2	6.0	1.7
2119	50	5	22400	100	3.95	0.02	3.97	8.9	0.1	5.1	1.9
2185	202	12	17000	200	3.93	0.02	4.10	5.5	0.1	3.5	1.0
2190	335	28	20400	450	3.18	0.02	3.67	8.9	0.3	7.2	0.8
2191^{c}	263	16	18050	50	3.80	0.02	4.04	6.2	0.1	3.9	1.1
2218	248	35	10110	57	3.84	0.03	4.07	2.6	0.1	2.5	0.1
2227	62	7	23600	1300	3.00	0.10	3.07	21.0	4.0	22.2	4.8
2232^{c}	115	5	22150	50	3.90	0.02	3.97	8.8	0.1	5.1	1.8
2255	333	15	20200	150	3.38	0.02	3.81	8.2	0.1	5.9	1.1
2311^{b}	51	5	23400	400	3.48	0.02	3.50	13.3	0.5	10.8	1.3
2336^{a}	173	9	19200	200	3.92	0.02	4.05	6.7	0.1	4.0	1.3
2347	84	11	21800	100	4.00	0.02	4.04	8.3	0.1	4.6	1.9
2361	68	8	25500	500	3.37	0.05	3.40	17.7	0.8	13.9	1.9

Table 3.1 (cont'd)

WEBDA ID (1)	V **sin** i **(km s^{-1})** (2)	ΔV **sin** i **(km s^{-1})** (3)	$T_{\rm eff}$ **(K)** (4)	$\Delta T_{\rm eff}$ **(K)** (5)	**log** g **(dex)** (6)	Δ **log** g **(dex)** (7)	**log** $g_{\rm polar}$ **(dex)** (8)	$M_\star$ ($M_\odot$) (9)	$\Delta M_\star$ ($M_\odot$) (10)	$R_\star$ ($R_\odot$) (11)	$\Delta R_\star$ ($R_\odot$) (12)
2392	87	17	21200	150	3.75	0.02	3.81	8.8	0.1	6.1	1.3
2520	45	10	23200	350	3.67	0.02	3.68	11.4	0.3	8.0	1.7
2540	271	23	19800	250	3.53	0.02	3.82	7.9	0.2	5.7	1.1
2555	129	6	18250	50	4.05	0.02	4.13	6.0	0.1	3.5	1.3
2605	54	27	24600	450	3.58	0.02	3.60	13.6	0.5	9.7	1.9
2622	373	35	17200	200	3.38	0.03	3.91	6.1	0.1	4.6	0.8
2716[a]	198	7	19650	50	3.75	0.02	3.92	7.3	0.1	4.9	1.2
2729	208	17	10410	74	3.83	0.03	4.01	2.8	0.1	2.7	0.1
2907	233	52	13700	150	3.86	0.03	4.07	3.9	0.1	3.0	0.4

[a] Proposed spectroscopic binary from Huang & Gies [2006b]

[b] Eclipsing binary from Southworth et al. [2004]

[c] Proposed eclipsing binary from Saesen et al. [2010]

Table 3.2. Physical Parameters of Be Star Cluster Members

WEBDA ID (1)	V **sin** i **(km s^{-1})** (2)	ΔV **sin** i **(km s^{-1})** (3)	$T_{\rm eff}$ **(K)** (4)	$\Delta T_{\rm eff}$ **(K)** (5)	**log** g **(dex)** (6)	Δ **log** g **(dex)** (7)	**log** $g_{\rm polar}$ **(dex)** (8)	$M_\star$ ($M_\odot$) (9)	$\Delta M_\star$ ($M_\odot$) (10)	$R_\star$ ($R_\odot$) (11)	$\Delta R_\star$ ($R_\odot$) (12)	**Notes** (13)
NGC 869												
49	172	21	25400	1790	3.54	0.23	3.54	15.4	2.5	11.0	2.0	No Emission Observed(1); Emission Observed(2,7,8)
146	195	6	25600	600	3.66	0.05	3.80	12.7	0.7	7.4	2.6	No Emission Observed(2,8); Emission Observed(4)
309	–	–	27700	1790	3.74	0.23	3.74	15.8	1.6	8.8	2.1	Emission Observed(1,2,4,5,8)
517	178	13	–	–	–	–	–	–	–	–	–	Emission Observed(4,6,7,8)
566[a]	306	25	22100	100	3.25	0.02	3.63	10.8	0.1	8.4	1.2	No Emission Observed(1,4,8); Emission Observed(2,7,8)
717[b]	126	22	26700	650	3.91	0.05	3.96	12.5	0.8	6.1	3.2	No Emission Observed(6,8); Emission Observed(3)
846	205	19	–	–	–	–	–	–	–	–	–	Emission Observed(4,6,7,8)
847	87	11	23000	1790	3.41	0.24	3.41	13.7	0.2	12.1	2.8	Emission Observed(2,4,6,7,8)
992	–	–	21700	1790	3.60	0.24	3.60	10.7	0.1	8.6	2.0	Emission Observed(6,8)
1057	–	–	21300	1790	2.69	0.25	2.69	29.5	0.2	40.8	9.6	Emission Observed(6,8)
1161	–	–	23400	1790	3.77	0.24	3.77	11.1	0.2	7.2	1.7	Emission Observed(2,4,5,6,7,8)
1261	285	78	26400	1790	3.72	0.23	3.72	14.3	0.6	8.6	2.0	Emission Observed(2,4,5,6,7,8)
1268	151	12	25400	500	3.46	0.05	3.59	14.6	0.6	10.1	2.2	No Emission Observed(6,8); Emission Observed(4)
1278	197	12	25100	1790	4.24	0.24	4.24	9.9	0.5	3.9	0.9	Emission Observed(4,6,7,8)
1282	–	–	22700	1790	3.95	0.24	3.95	9.2	0.2	5.3	1.2	Emission Observed(2,4,5,6,7,8)
NGC 884												
1702[a]	–	–	24400	1790	3.67	0.24	3.67	12.6	0.3	8.6	2.0	Emission Observed(1,2,4,6,7,8)
1772	379	28	–	–	–	–	–	–	–	–	–	No Emission Observed(4); Emission Observed(6,8)
1926[a]	106	17	27400	1790	3.89	0.23	3.89	13.9	1.2	7.0	1.6	Emission Observed(2,4,6,7,8)
1977	–	–	20400	1790	4.27	0.25	4.27	6.8	0.1	3.2	0.7	Emission Observed(2,4,6,7,8)
2088[a]	–	–	21900	1790	3.72	0.24	3.72	10.0	0.1	7.2	1.7	Emission Observed(2,4,5,6,7,8)
2091[a]	236	40	18800	1790	3.97	0.26	3.97	6.7	0.1	4.4	1.0	Emission Observed(4,6,7,8)
2138	153	37	24100	1790	3.53	0.24	3.53	13.8	0.2	10.5	2.5	Emission Observed(1,2,4,5,7,8)
2165	–	–	24800	1790	3.79	0.24	3.79	11.9	0.3	7.3	1.7	Emission Observed(2,4,5,6,7,8)
2262	265	19	24900	1400	3.51	0.08	3.75	12.3	1.4	7.7	2.2	No Emission Observed(4,8); Emission Observed(2,6)
2284	–	–	26500	1790	3.77	0.23	3.76	14.0	0.7	8.1	1.9	Emission Observed(2,4,5,6,7,8)

Table 3.2 (cont'd)

WEBDA ID (1)	V **sin** i **(km s^{-1})** (2)	ΔV **sin** i **(km s^{-1})** (3)	$T_{\rm eff}$ **(K)** (4)	$\Delta T_{\rm eff}$ **(K)** (5)	**log** g **(dex)** (6)	Δ **log** g **(dex)** (7)	**log** $g_{\rm polar}$ **(dex)** (8)	$M_\star$ ($M_\odot$) (9)	$\Delta M_\star$ ($M_\odot$) (10)	$R_\star$ ($R_\odot$) (11)	$\Delta R_\star$ ($R_\odot$) (12)	**Notes** (13)
2468	134	46	10070	48	3.88	0.03	4.00	2.7	0.1	2.7	0.1	No Emission Observed(8); Emission Observed(7)
2563	308	74	26100	1790	4.02	0.23	4.02	11.6	1.5	5.5	2.7	Emission Observed(2,4,6,7,8)
2771	–	–	21800	1790	3.99	0.24	3.99	8.5	0.1	4.9	1.1	Emission Observed(2,4,7,8)

References: (1) Schild [1966], (2) Slettebak [1985], (3) Fabregat et al. [1994], (4) Keller et al. [2001], (5) Slesnick et al. [2002], (6) Bragg & Kenyon [2002], (7) Be candidate with observed IR excesses in Currie et al. [2008], (8) This work.

[a] Proposed spectroscopic binary from Huang & Gies [2006b]

[b] Candidate spectroscopic binary from Strom et al. [2005]

Using the values of mass, $M_\star$, and radius, $R_\star$, discussed below for all stars in our sample, we can determine the critical velocity

$$V_{\rm crit} = \sqrt{\frac{GM_\star}{R_{\rm e}}} \tag{3.1}$$

for our stars. V_{crit} is the rotational velocity at which the centripetal and gravitational forces keeping the star together would become imbalanced, resulting in the destruction of the star. For simplicity in this expression, we assume that the polar radius of the star, $R_{\rm p}$, is equal to $R_\star$, and that a rotationally distorted star has an equatorial radius $R_{\rm e} = 1.5R_{\rm p}$. With this, we find a mean $V_{\rm crit}$ of 430 km s^{-1} for the B-type and Be stars in these clusters.

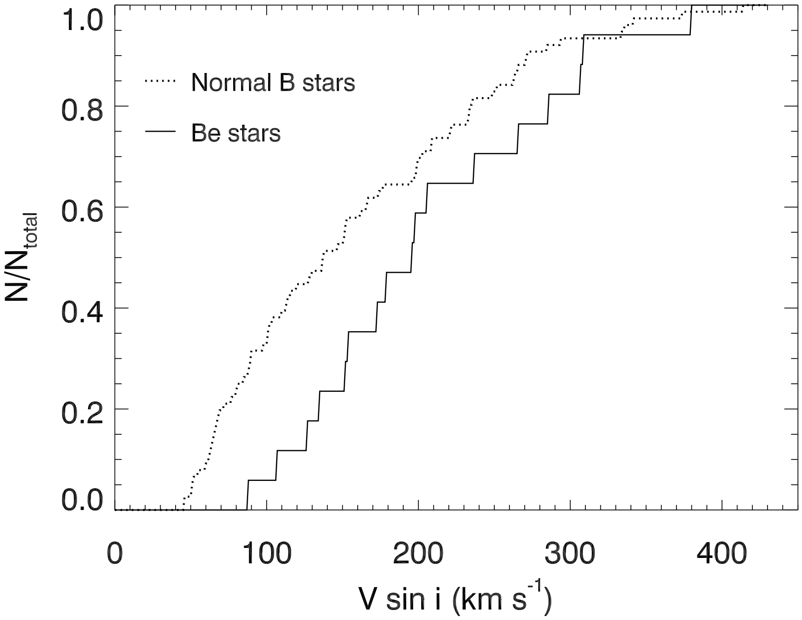

Figure 3.2 Cumulative distribution function of V sin i for the Be stars (*dashed line*) and the normal B-type stars (*dotted line*) of both NGC 869 and NGC 884.

Having determined values of V sin i for each star, we turn again to model spectral fitting to determine values for $T_{\rm eff}$ and log g from the Hγ line at 4340Å. The hydrogen Balmer lines are particularly sensitive to $T_{\rm eff}$ and log g, making them ideal for determining these quantities accurately. The method outlined here was employed for normal B-type stars and Be stars with no emission present in our 2005 observations.

For stars having $T_{\rm eff} \leq 15000$ K we employ the methods of Huang & Gies [2006a], who use Hγ line profiles generated by the line-blanketed, local thermodynamic equilibrium (LTE) Kurucz ATLAS9 and SYNSPEC codes. The "virtual star" models produced by their code simulate spherically symmetric stars with constant $T_{\rm eff}$ and log g across their surface, and the spectra of these model stars are then used to determine these values and their errors for our observed spectra, similar to our procedure for V sin i. The errors $\Delta T_{\rm eff}$ and Δlog g are determined from the quadratic sum of the V sin i propagated errors and the errors due to the intrinsic noise in the observed spectra. For hotter stars, LTE models should systematically underestimate $T_{\rm eff}$ as non-LTE effects alter the equivalent width of the Hγ line we are measuring. Hence for stars having $T_{\rm eff} \geq 15000$ K, we use instead the metal line-blanketed, non-LTE, plane-parallel, hydrostatic TLUSTY BSTAR2006 model spectra [Lanz & Hubeny, 2007]. A sample fit of the Hγ line in NGC 869–90 is shown in the left panel of Figure 3.1. The errors $\Delta T_{\rm eff}$ and Δlog g are determined from the values that produce an rms^2 no more than 2.7rms$^2/N$ greater than the minimum rms^2. Our results for $T_{\rm eff}$, log g, and their respective errors are shown in columns 4–7 of Table 3.1.

29% of the stars in our sample are rapid rotators, having measured values of V sin i in excess of 200 km s^{-1}. At such significant rotational velocities, the assumption of a spherical shape for these stars is no longer plausible given the substantial centrifugal forces distorting the stars into oblate spheroids. This rotational distortion produces significant differences in both the temperatures and surface gravities at the polar and equatorial regions. As the measured values of $T_{\rm eff}$ and log g are averages across the visible stellar hemisphere, these rotational effects produce lower values than expected, a phenomenon known as gravitational darkening. As the rotation rate for a star approaches its critical velocity, the equatorial radius may increase by as much as 50%, while the polar radius remains unchanged. For these reasons, we convert our measured log g to log $g_{\rm polar}$, as detailed in Huang & Gies [2006a]. The authors produce detailed spectroscopic models to investigate the effects of such rotational distortions and determine a statistical correction factor for log g. This factor is averaged over all possible values of inclination angle, i, for a variety of stellar models. By bilinearly interpolating between their models, we converted our measured value of log g to log $g_{\rm polar}$. This value of log $g_{\rm polar}$ is a better measure of the true surface gravity of the star, untainted by the effects of rapid rotation, and provides us a more accurate means of comparison between slowly and rapidly rotating stars. The log g_{polar} correction is therefore most significant for stars rotating more rapidly than 50% of V_{crit}. We assume that this conversion produces a negligible change to the value determined previously for Δlog g. Our derived values of log g_{polar} are listed in column 8 of Table 3.1.

Once we have measured parameters for all of the B-type stars, we can then determine $M_\star$ and $R_\star$ for each of them by interpolating values from the Schaller et al. [1992] non-rotating evolutionary tracks, consistent with the slow rotation of most of our targets. These evolutionary tracks are shown plotted with T_{eff} and log g_{polar} in Figure 3.3. The errors $\Delta M_\star$ and $\Delta R_\star$ correspond to our measured ΔT_{eff} and Δlog g. Additionally, we have compared our results with the rotating models of Ekström et al. [2012], and we find agreement between the models to within 10%. The resulting values of $M_\star$, $R_\star$, and their respective errors are listed in columns 9–12 of Tables 3.1 and 3.2. We have also checked the accuracy of our results by comparing the TLUSTY BSTAR2006 model SEDs with the observed SEDs for our B-type sample stars, and find excellent agreement between our derivations of distance and reddening with the accepted values of Currie et al. [2010]. These results will be discussed further in Chapter 4.

3.2 Strömgren Photometric Method for Emission Be Stars

We note that star NGC 869–566 did not show any signs of emission in our initial observations, but has since exhibited progressively stronger emission in our more recent 2010 and 2012 observations; hence we include it among the non-emission Be stars and have measured T_{eff} and log g from the Hγ line in its 2005 blue spectrum. Given the poorer resolution of 2009 and 2010 blue WIRO spectra, we cannot use these data with our spectral fitting techniques. We therefore use only the blue and red WIRO spectra from these observing runs to identify Be stars exhibiting emission at the time of our observations.

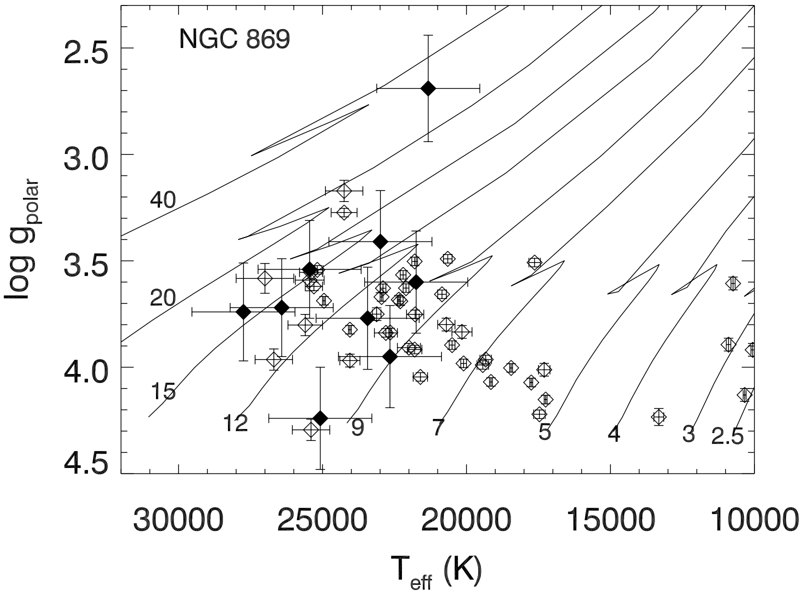

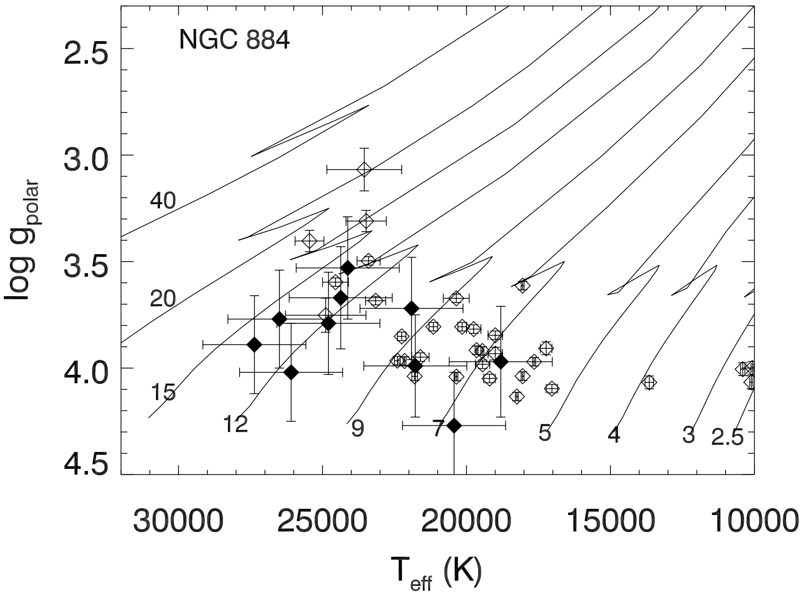

Figure 3.3 For both NGC 869 (top) and NGC 884 (bottom), T_{eff} and log g_{polar} are plotted with the evolutionary tracks of Schaller et al. (1992). The zero age main sequence (ZAMS) mass of each evolutionary track is labeled along the bottom. Normal B-type stars are shown as open diamonds while Be stars are filled diamonds.

For the other Be stars in our sample we cannot determine accurate values for T_{eff} and log g via the same model fitting technique, as hydrogen absorption line profiles are altered by emission during disk phases of these stars. Instead we can use Strömgren photometry available from the WEBDA[5] database to correlate T_{eff} and log g for all of the B-type and Be stars in our sample. Non-emission B stars with both available Strömgren photometry and spectral model fits were included as calibration stars for the photometric technique. To this we add eight additional stars from Napiwotzki et al. [1993] with well-known T_{eff} and available Strömgren data. We use *ubvy* magnitudes to first determine the Strömgren indices m_1 and c_1, given by equations 2.4 and 2.5. The calculation of T_{eff} determined by Balona [1984] requires us to convert the c_1 index to the dereddened index c via the expressions

$$E(b-y) = E(B-V) \times 0.754 \tag{3.2}$$

$$c_0 = c_1 - 0.19[E(b-y)] \tag{3.3}$$

$$c = \log(c_0 + 0.200), \tag{3.4}$$

which use the reddening values of the clusters, E$(B-V) = 0.55$ and E$(B-V) = 0.52$ for h and χ Per, respectively [Bragg & Kenyon, 2005, Currie et al., 2010]. Using these indices and the Hβ line magnitude (β), we can then calculate T_{eff} via the relationship

$$\begin{aligned}\log T_{\text{Balona}} =& 3.9036 - 0.4816(c) - 0.5290(\beta)\\ &- 0.1260(c)^2 + 0.0924(\beta)(c) - 0.4013(\beta)^2\end{aligned} \tag{3.5}$$

given by Balona [1984].

McSwain et al. [2008] found that this calculated value, T_{Balona}, slightly underestimates the true T_{eff} of the B-type stars. Thus, we performed a linear fit to the data, shown in Figure 3.4(a), and determined a correction factor that will bring the two independent measurements into agreement. In this way, we are able to use the B-type stars measured by both methods as a calibration to yield values of T_{eff} for the otherwise immeasurable Be stars. These T_{eff} and our calculated errors are listed in columns 4 and 5 of Table 3.2.

To determine log g, Balona [1984] advocate using β and c_0. Given that β serves

---

[5] Available online at www.univie.ac.at/webda and maintained by Ernst Paunzen.

as an indicator of log g via spectra line width, and c_0 is an indicator of temperature in hot stars, the relationship between these two values can serve as a Hertzsprung-Russell diagram for the cluster providing a means for investigating the temperature and evolutionary trends of the stellar population. In more evolved giant or supergiant stars (luminosity classes III and I, respectively), the hydrogen lines are very narrow due to the lower densities in the outer atmospheres of these stars, decreasing the collisional rates that produce the pressure broadening mechanism. Main sequence stars (luminosity class V), which host more dense atmospheres and thus higher collisional rates and higher pressures, have broader hydrogen lines. In general, we do see that the values of c_0 and β for the B-type calibrators shown in Figure 3.4(b) agree with the relations for class V and III stars of Balona & Shobbrook [1984]. However, the circumstellar disks present in Be stars (shown as filled diamonds in Figure 3.4(b)) will artificially brighten the β magnitudes of these stars, contaminating the $c_0 - \beta$ relation for these stars and our calculated values of log g. The spread in log g of the B-type calibration stars prevents us from simply applying either of the $c_0 - \beta$ relations shown in Figure 3.4(b) to the population. Instead, we perform a linear fit to the calibration star data and obtain a corrected value of β which we then use to correct our calculated T_{Balona} and finalize our calibrated, calculated temperatures and surface gravities for the Be stars exhibiting emission in our data. Since the clusters are approximately the same age, this single fit is appropriate. Additional details regarding the method to determine T_{eff}, log g, $M_\star$, $R_\star$, and their respective errors for the Be stars can be found in McSwain et al. [2008]. We do not perform any further correction to obtain log g_{polar} for the Be stars measured with this technique, given the large scatter between the calibrators' log g_{polar} and their Strömgren log g. The final results for log g and Δlog g of the Be stars are listed in columns 6–7 of Table 3.2.

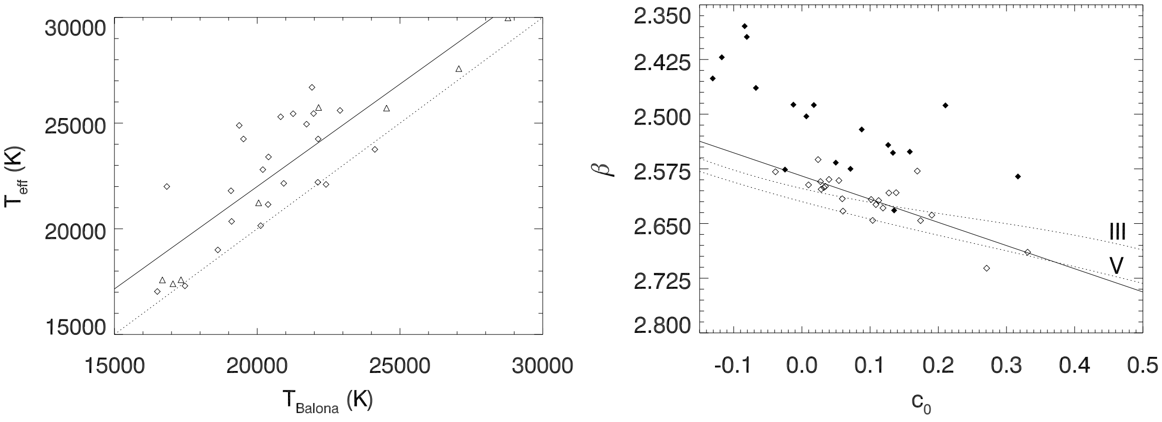

Figure 3.4 (left): $T_{\rm eff}$ measured for the B-type temperature calibration stars from our work (*diamonds*) and from Napiwotzki et al. (1993; *triangles*) compared to their calculated $T_{\rm Balona}$ (Balona 1984). A linear fit of the two temperature scales (*solid line*) and the 1:1 agreement (*dotted line*) are also shown. (right): Strömgren c_0 index and β magnitude are plotted with the $c_0 - \beta$ relations for luminosity class V and III stars (Balona & Shobbrook 1984; *dotted lines*). The B-type temperature calibration stars from this work (*diamonds*) are plotted with 18 Be stars (*filled diamonds*) to demonstrate that the Be star β magnitudes are brightened due to the disk emission present. A best fit line for the calibration stars is also shown (*solid line*).

We highlight our results regarding the Be star population in Table 3.2, and we note that these Be stars were selected from the literature based on previous observations of spectral line emission or via photometric surveys needing spectroscopic confirmation. Presented within Table 3.2 are a total of 28 known or proposed Be stars within our sample of 104 stars. For these objects we were able to examine the state of emission from our observations, and then determine their stellar parameters by our spectral modeling or Strömgren photometry methods as detailed earlier in this section. The broad-band Strömgren indices used to derive their $T_{\rm eff}$ and log g are not likely to be affected by their rapid rotation. We do see evidence of emission in 22 of these Be stars. Interestingly, we see evidence in our data for at least 8 "transient" Be stars [McSwain et al., 2008]. The stars NGC 869–146, NGC 869–717, NGC 869–1268, and NGC 884–2262 were observed as Be stars in the past [Bragg & Kenyon, 2002, Fabregat et al., 1994, Keller et al., 2001, Slettebak, 1985], and the star NGC 884–2468 is a proposed candidate Be star [Currie et al., 2008]. However, we do not see evidence of emission in our observations of these objects. As mentioned previously, the known Be star NGC 869–566 was initially observed by us in 2005 and showed no sign of emission in its spectrum. However, it has since developed increasingly stronger emission in our 2010 and 2012 observations. For the other two transient Be stars (NGC 869–49, NGC 884–1772), we do see emission in our spectra, however other authors have noted them in non-emission phases in the past [Bragg & Kenyon, 2002, Keller et al., 2001, Schild, 1966, Slettebak, 1985].

3.3 Comparison with Other Studies

Previous studies, such as Strom et al. [2005] and Huang & Gies [2006a], have investigated some of our B star targets to determine the same basic stellar parameters we have, however their analyses employed LTE atmospheric models or quantitative corrections to LTE model measurements to account for non-LTE effects. Between these two studies there are clear discrepancies in their measurements and the conclusions each draws regarding the natal rotation rates and angular momentum evolution of the clusters' massive stars. An accurate determination of a given star's surface gravity is essential to the evaluation of stellar radius and evolutionary state. As we show here, non-LTE effects can contribute to significant errors in measurements of log g.

3.3.1 Huang & Gies 2006

Amongst the 54 stars common to our sample and to that of Huang & Gies [2006a], we find some discrepancies between our respective results. As can be seen in Figure 3.5(a), there is very good agreement in our determinations of V sin i. This is to be expected since we both used LTE models to fit the He I and Mg II lines to measure V sin i. The differences at low V sin i may be due to a difference in spectral resolution between our respective datasets.

However, differences in our measured temperatures for stars with $T_{\rm eff} \geq 15000$ K and in our measured log g values are clearly apparent in Figures 3.5(b) and 3.5(c), respectively. Given that our general methodology for measuring $T_{\rm eff}$ and log g is the same as Huang & Gies [2006a], the source of these discrepancies lies partially in our use of different stellar models. While Huang & Gies [2006a] employ the LTE Kurucz ATLAS9 models [Kurucz, 1994], we use the more recently available non-LTE TLUSTY BSTAR2006 models of Lanz & Hubeny [2007] for those stars in our sample with $T_{\rm eff} \geq 15000$ K. In their analysis Huang & Gies [2006a] acknowledge that their derived temperatures are likely to be slightly lower and gravities slightly higher compared to measurements derived from non-LTE model atmospheres, as shown by the comparative analysis of Lanz & Hubeny [2007].

Lanz & Hubeny [2007] find that in the non-LTE models the hydrogen Balmer lines tend to be broader and stronger due to the overpopulation of the $n = 2$ energy state, thus LTE models will yield overestimated surface gravities due to the altered shape of the Balmer line wings. Przybilla et al. [2011] compared LTE ATLAS9 models to non-LTE TLUSTY models for temperatures between 15000–35000 K. They found that non-LTE effects are significant above 22,000 K, affecting both the cores and wings of the Balmer lines. They find that LTE Balmer line profiles have equivalent widths up to 30% lower than in non-LTE line profiles. This would cause a non-LTE model to find a higher temperature for the same observed line, or conversely for an LTE model to underestimate the temperature. Przybilla et al. [2011] also find that LTE models of the Hγ line may overestimate log g by up to 0.2 dex.

While the expected temperature disagreement is opposite of the trend we find in our comparison of our work with the results of Huang & Gies [2006a], several of our common sample stars with temperatures greater than 24,000K are Be stars, some of which we find to exhibit transient behavior. It is likely that emission has subtly filled in or otherwise altered the Hγ line profile, which would result in the overestimation of $T_{\rm eff}$ for these stars by Huang & Gies [2006a]. We also find one proposed spectroscopic binary among this common sample, so the Hγ line profiles may be further altered by variable line blending effects. For the remaining B-type stars in this region it is possible that our temperature discrepancy is due to variable emission in unknown Be stars, unresolved binaries, clumping in the hot stellar wind, or differences in the atomic species included in our respective atmospheric models that affect hydrogen Stark broadening [Przybilla & Butler, 2004].

With the quantified disagreement in $T_{\rm eff}$ and log g shown here, the anticipated effect of non-LTE atmospheres on the measurement results is more significant than initially assumed by Huang & Gies [2006a]. The effects of these overestimated temperatures and gravities also affect their determined stellar masses, their usage of log g as an indicator of stellar evolutionary status, and their determined spin-down rates of B and Be stars. We find that cluster members are more evolved than indicated by Huang & Gies [2006a]. These B stars may spin down more slowly than the rates observed by Huang & Gies [2006a] and Huang et al. [2010].

3.3.2 Strom et al. 2005

We also compare our results to those presented by Strom et al. [2005], who adopt the $T_{\rm eff}$ values derived from UBV photometry by Slesnick et al. [2002]. In their study they find reasonable agreement between their measurements of V sin i and those of Huang & Gies [2006a], though their results are systematically 5% smaller than the results of Huang & Gies [2006a]. Comparing the results for the 26 stars common to our two samples, we find a similar agreement and systematic underestimation of Strom et al.'s V sin i values when compared to our measurements, as is expected given the excellent agreement of our results with those of Huang & Gies [2006a]. Upon further comparison of our results, we find that Strom et al. [2005] and Slesnick et al. [2002] have overestimated $T_{\rm eff}$ for hotter stars as well. We note that the two most discrepant stars are both Be stars, suggesting that their Hβ emission contaminates the B-band brightness used to derive $T_{\rm eff}$. Thus $M_\star$ and $R_\star$ for the Be stars as shown in Figure 3.5(d) are also likely overestimated.

Finally, we note that many of our Be stars were found to be possible spectroscopic binaries by Huang & Gies [2006a] and Strom et al. [2005]. Since Huang & Gies [2006a] did not present measurements of $T_{\rm eff}$ or log g for many of their spectroscopic binaries, not all of our measurements could be directly compared. Their classification as binaries may be inaccurate due to variable emission in their spectral lines. Further monitoring of their radial velocities as well as their emission will clarify their status.

3.4 Chapter Summary

We have determined V sin i, $T_{\rm eff}$, log $g_{\rm polar}$, $M_\star$, and $R_\star$ for 104 B-type and Be star members of NGC 869 and NGC 884 using spectroscopic modeling techniques and

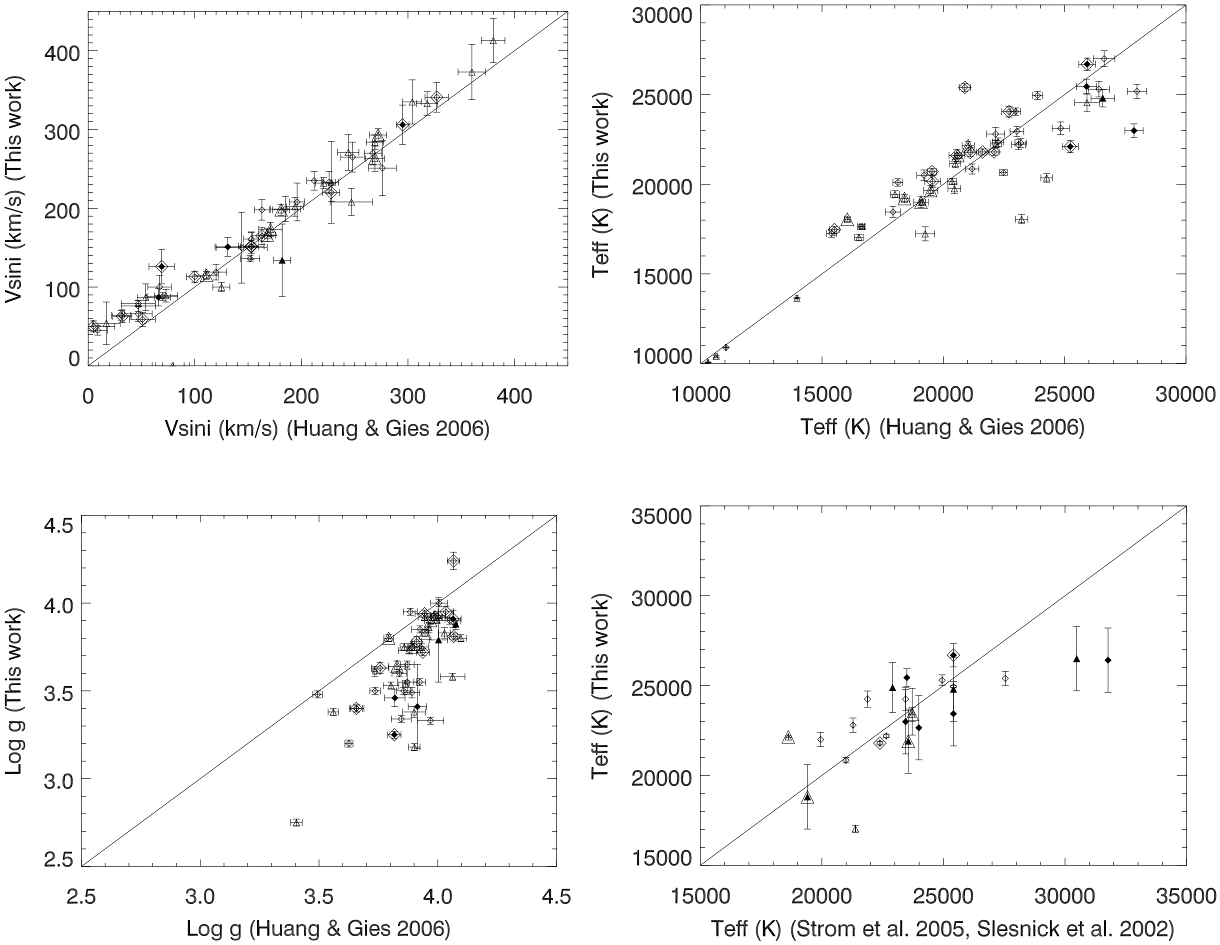

Figure 3.5 Comparisons of the resultant $V \sin i$ (top left), $T_{\rm eff}$ (top right), and log g (bottom left) measurements from this work and Huang & Gies [2006a], as well as a comparison of our $V \sin i$ results with those of Strom et al. [2005], and Slesnick et al. [2002] (bottom right). NGC 869 cluster members are shown as open diamonds, while NGC 884 members are shown as open triangles. Be stars are shown as filled diamonds and triangles. Spectroscopic binaries, as noted in Tables 3.1 and 3.2, are highlighted by double-sized symbols.

calculations from Strömgren photometry. Our determined values for $V \sin i$ are in good agreement with the earlier results of Huang & Gies [2006a], though there is some discrepancy in our measured temperatures and surface gravities due to our use of the more recently available non-LTE BSTAR2006 stellar models of Lanz & Hubeny [2007] and the possible contamination of Be stars and spectroscopic binaries. Because of the resulting over-estimation of log g, Huang & Gies [2006a] have underestimated the retention of initial angular momentum by the cluster members.

We find that the cluster members are significantly more evolved than found by previous measurements. We also identify 8 transient Be stars in h and χ Per. The Be stars in these clusters are also rotating more slowly than expected based upon other young open clusters. Further monitoring of the massive stellar constituents of these clusters, and their rotation rates is well warranted.

Chapter 4

Stellar Distances

With the reliable values for $V \sin i$, T_{eff}, $\log g$, $M_\star$, and $R_\star$ established in Chapter 3 for our sample stars, we can now develop a means for separating the flux produced by our sample stars and flux being contributed from other sources in the star's environment. These parameter measurements will now be utilized in conjunction with photometric magnitudes gathered from several optical and IR surveys to examine the total flux emitted by our B-type sample stars, and to the determine distance to each cluster.

4.1 Spectral Energy Distributions of B-type Stars

In general, an SED demonstrates the total flux being emitted by a source across the electromagnetic spectrum. This flux can be modeled based upon the stellar temperature and surface gravity, and observed by determining photometric magnitudes for the source in the UV, optical, and IR regions of the spectrum.

In order to compare the flux of a model SED to that of an observed star, we must take into account the observed angular size of our target star. The amount of flux observed from a given star decreases with distance as an inverse square law,

$$F_{obs} = \frac{L}{4\pi r^2} = \frac{4\pi R^2 \sigma T^4}{4\pi r^2}. \tag{4.1}$$

In this expression R is the stellar radius, T is the stellar temperature, and r is the distance to the star. As the distance between the star and observer increases, the flux received by the observer decreases by a factor of r^2. Therefore, before using our model flux we must normalize it to this same angular size we perceive our observed star to have. In this way we can determine how much flux would be received from our model star if it were sitting at the same location as our observed star, and make a direct comparison between the model and observed SEDs. The relevant quantities for this geometric calculation are shown in the Figure 4.1 schematic, and for our purposes we define θ_c as half the angular diameter of the resolved stellar disk. Using the tangent trigonometric relation and a small angle approximation, which is valid given the large distances involved, it can be shown that the angular diameter is given by

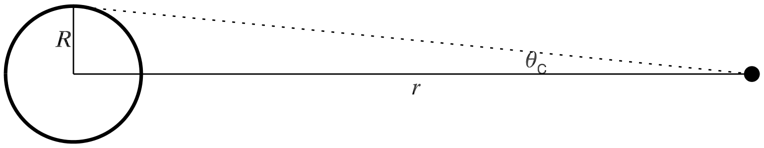

Figure 4.1 Illustration of the relevant geometric quantities for determining stellar distance via angular diameter.

$$\theta_D = 2\theta_c = 2\left(\frac{R}{r}\right). \tag{4.2}$$

To determine the total flux emitted by the star across all wavelengths, ie. the bolometric flux, we integrate the observed flux over all frequencies

$$F = \int F_\nu d\nu = \left(\frac{R}{r}\right)^2 \sigma T_{\text{eff}}^4, \tag{4.3}$$

where T_{eff} is the effective surface temperature. Using this result, the angular diameter of the star, θ_D, can now be expressed as

$$\theta_D = \frac{2R}{r} = 2\left(\frac{\int F_\nu d\nu}{\sigma T_{\text{eff}}^4}\right)^{1/2}, \tag{4.4}$$

which is in terms of the bolometric stellar flux observed here on Earth. Finally, interstellar extinction must be taken into account in our calculation, as it will significantly alter the flux observed at bluer wavelengths. To determine the actual stellar flux one needs to utilize model stellar atmospheres to yield the model flux distribution. Interstellar extinction is applied to the appropriate stellar model, giving the reddened bolometric flux, F_{red}. In practice, the model continuum is then matched with the observed SED so that the ratio, $F_{\nu,obs}/F_{\nu,mod}$, which is independent of ν, can be used in our expression

$$\theta_D = \frac{2R}{r} = 2\left(\frac{F_{\nu,obs}}{F_{\nu,mod}}\right)^{1/2}. \tag{4.5}$$

For our sample B-type stars with $T_{\rm eff} \geq 15000$ K, stellar flux models are selected from the TLUSTY BSTAR2006 grid of SED models [Lanz & Hubeny, 2007], based on the values of $T_{\rm eff}$ and log $g_{\rm pol}$ determined in Chapter 3 for each star. Using the reported E$(B-V)$ values from Currie et al. [2010], we applied the galactic reddening model of Fitzpatrick [1999], with the ratio of total extinction in V to the selected extinction $A_V/\mathrm{E}(B-V) = 3.1$, to our model flux. Recall from Chapter 1 that reddening or extinction is the preferential scattering of bluer wavelengths of light by interstellar material between observer and object, thus resulting in an object appearing to emit fewer short wavelength photons that it truly does. The model SED flux is then normalized to the angular size of the star, as described above, using the value of $R_\star$ determined in Chapter 3. After interpolating the reddened model flux, F_{red}, onto the same wavelength scale as the observed flux points, the average of the ratio F_{red}/F_{obs} gives the needed normalization factor. Shown in Figure 4.2 are the normalized reddened model flux and observed flux points for the B-type star NGC 869–864. The dotted and dashed model SEDs illustrate the error in the reported E$(B-V)$ values, and the effect this reddening has on an SED.

For B-type stars with $T_{\rm eff} \leq 15000$ K, stellar flux models are selected from the ATLAS9 SED models [Castelli & Kurucz, 2004], based on the $T_{\rm eff}$ and log $g_{\rm pol}$ determined in Chapter 3 for each star. The same method described above for the hotter B star SEDs was utilized, however we found that the resultant distances were systematically too low for the observed fluxes for these stars, suggesting that they may be foreground objects. These foreground stars simply lie along a similar line of sight as h and χ Per, but are significantly closer to us and are not gravitationally bound to the clusters (ie. not cluster members). For this reason we exclude the few cooler stars in our sample from further analysis.

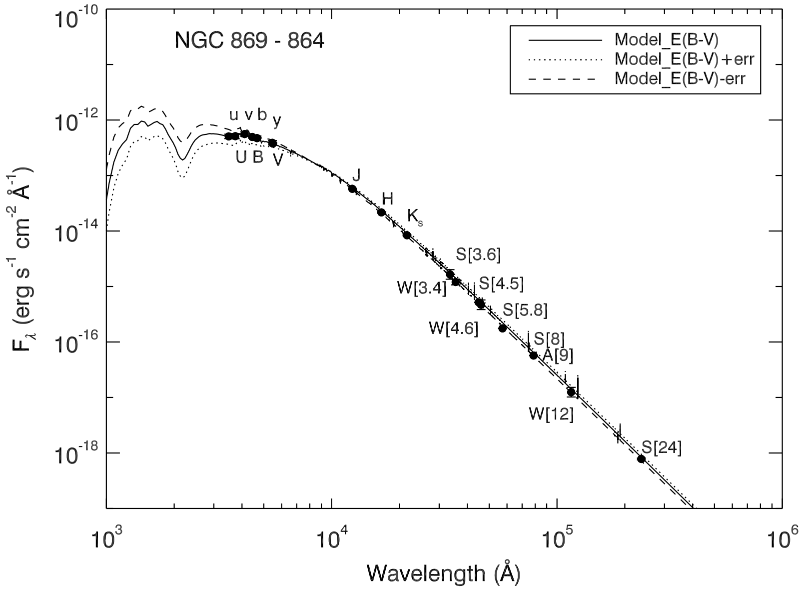

Figure 4.2 Example SED of B-type star NGC 869 - 864.

4.2 Distance from Absolute Flux

After producing the normalized SEDs of the previous section, solving Equation 4.5 for r yields the distance to the star in question. Having calculated distances for all B-type sample stars via their SEDs, the complied histograms for each cluster are shown in Figure 4.3. The lighter histograms of each plot indicate the high and low distance distributions utilizing the high and low values of E$(B-V)$ as determined by Currie et al. [2010]. The distribution for each cluster has been fit with a Gaussian profile, shown in the figure, for comparison. The distribution mean provides the measured cluster distance, and the 1σ standard deviation of the histogram then provides a measurement of the error for this method. The slight bimodality of these distributions suggest that some of the stars in our sample may be foreground objects rather than cluster members, but firm conclusions regarding their membership to either cluster cannot be proposed with our small sample size.

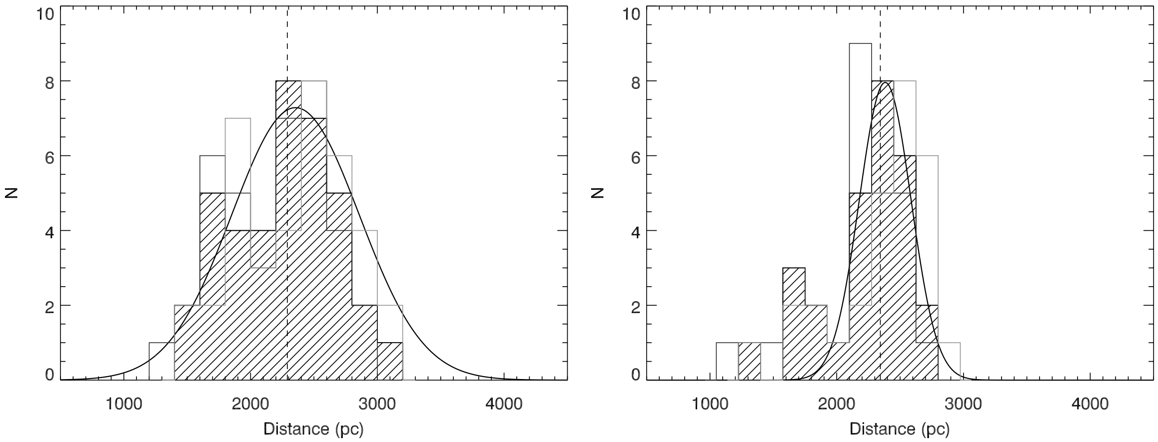

Figure 4.3 Histograms illustrating the distances determined for B-type cluster members via the absolute flux method. Shown on the left is the distribution for NGC 869 ($r = 2260 \pm 426$ pc), and the distribution for NGC 884 ($r = 2239 \pm 371$ pc) is on the right. Un-filled histograms illustrate the high and low distance distribution results using the high and low errors of E($B - V$) from Currie et al. [2010]. The vertical dashed line indicates the cluster distance reported by Currie et al. [2010].

4.3 Distance from Spectroscopic Parallax

A second method of determining stellar distance, utilizing luminosity and absolute magnitude, will provide us with a means of checking the accuracy of our distance measurements from absolute fluxes. Stellar luminosity, as discussed in Chapter 1, is given by the expression

$$L = 4\pi R^2 \sigma T^4, \tag{4.6}$$

where T is the stellar temperature, and R is the stellar radius. The luminosity of any star can be related to that of the Sun, via the dimensionless ratio of $L_\star/L_\odot$. Taking the log of both sides of this expression gives

$$\log\left(\frac{L_\star}{L_\odot}\right) = 2\log R_\star + 4\log T_\star - 4\log T_\odot - 2\log R_\odot. \tag{4.7}$$

The $\log(L_\star/L_\odot)$ is then related to the absolute bolometric magnitudes of the star in question and the Sun, via

$$M_{bol,\star} - M_{bol,\odot} = -2.5 \log \left(\frac{L_\star}{L_\odot} \right). \tag{4.8}$$

To determine the absolute V band magnitude needed for the following step, the bolometric correction (BC) is applied,

$$M_V = M_{bol,\star} - BC. \tag{4.9}$$

By substituting Equations 4.7 and 4.9 into our luminosity–absolute magnitude relation, we can now determine the distance modulus (DM)

$$\begin{aligned} DM = V - M_V = & 5 \log R_\star + 10 \log T_\star - 10 \log T_\odot \\ & - M_{bol,\odot} + BC + V - 3.1[E(B-V)]. \end{aligned} \tag{4.10}$$

Finally, the distance modulus calculated above is used with the magnitude–distance relation,

$$DM = 5 \log \left(\frac{r}{10pc} \right), \tag{4.11}$$

where r is the stellar distance in units of parsecs.

To apply this method to our sample stars we utilize the values of T_{eff} and $R_\star$ determined in Chapter 3, and the reported V magnitude from WEBDA for each of our sample stars. We then interpolate a BC for each star from the TLUSTY BSTAR2006 grid of stellar models provided by Lanz & Hubeny [2007] based on our determined values of T_{eff} and $\log g$. Using the reported E$(B-V)$'s from Currie et al. [2010], we use the above equations to determine the distance to each star. The results of these calculations are compiled for each cluster in Figure 4.4, which follows the same format as Figure 4.3. The distribution of distances for each cluster has been again fit with a Gaussian profile, shown in the figure for comparison. The distribution mean provides the measure cluster distance, and the 1σ standard deviation of the histogram then provides a measurement of the error for this method.

The resulting distance distributions from the spectroscopic parallax technique are comparable to those achieved in Section 4.2 using absolute fluxes, with the results

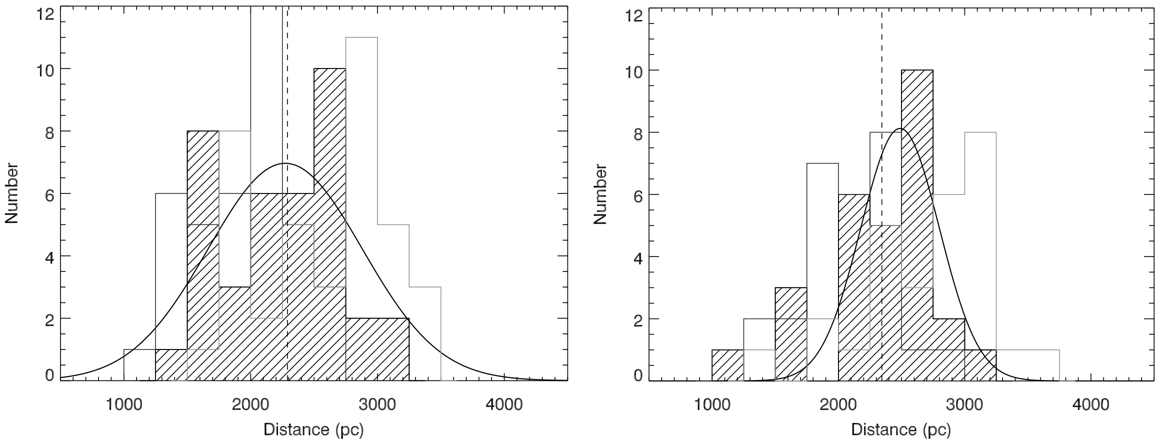

Figure 4.4 Histograms illustrating the distances determined for B-type cluster members via the spectroscopic parallax method. Shown on the left is the distribution for NGC 869 ($r = 2246 \pm 443$ pc), and the distribution for NGC 884($r = 2357 \pm 429$ pc) is on the right. Un-filled histograms illustrate the high and low distance distribution results using the high and low errors of E($B - V$) from Currie et al. [2010]. The vertical dashed line indicates the cluster distance reported by Currie et al. [2010].

for each cluster falling within the error bars of both techniques. The distributions produced by both methods show a very similar slight bimodality, further suggesting that some stars in our sample may not be true cluster members. These results are also in good agreement with those of Currie et al. [2010], who find distances of 2290 ± 87pc for NGC 869, and 2344 ± 88 pc for NGC 884, giving us further confidence in our physical parameter measurements and model SEDs.

4.4 Summary/Conclusions

We find our determined distances from both the absolute magnitude and spectroscopic parallax methods to be consistent with the accepted cluster distances as determined by Currie et al. [2010]. Additionally, with the excellent agreement of the model SEDs, selected by our determined physical parameters, and the observed SEDs, we can be confident in our ability to accurately model the stellar flux of our B-type stars. This will allow us to further investigate the disks of our Be stars, as we can now extract the stellar flux contribution and examine the contribution of the disks to the total system flux.

Chapter 5

Be Star Disk Models

With the ability to confidently model and remove the stellar contribution to the total Be star flux, we can begin to look more closely at the Be star disks themselves. Measuring the strength of Hα line emission present in Be stars provides a quick measure of the relative strength and size of the disk present. When used in conjunction with numerical disk structure models, we can place limits on the disk radius, density, and mass. This chapter details the measured Hα strengths for multiple observations of each of our sample Be stars, and the results we obtain from two different disk models for the physical parameters of our sample Be disks.

5.1 Disk Variability

As discussed previously in Chapter 1, Be star disks exhibit a wide range of variability over both short and long time scales. One means of tracing this variability over time is monitoring of the Hα line strength. With a significant fraction of Be stars known in NGC 869 and NGC 884, there is a wealth of observations in the literature quantifying the strength of the Balmer lines in these stars. By compiling the results from a number of these studies, we find evidence for longterm variability in a number of our sample Be stars (denoted in column 11 of Table 3.2). To further investigate and quantify the variability of these Be star disks, we have conducted a 4 year spectroscopic monitoring campaign, in which we have repeatedly observed the hydrogen Balmer lines of our sample stars using a variety of instruments, detailed in Chapter 2.

We use the Hα equivalent width ($W_{H\alpha}$) as a means of quantifying the strength of the Hα line and any emission present. Equivalent width is proportional to the measured area contained within a spectral line, up to the continuum. The reported value is given as the width of a rectangle, 0 to continuum, that contains the same area as the spectral line, as illustrated by Figure 5.1. More formally, equivalent width can be expressed as

$$W_\lambda = \int \frac{F_c - F_\lambda}{F_c} d\lambda, \tag{5.1}$$

where F_λ is the intensity of the spectrum at a given wavelength and F_c is the continuum intensity. For instances of emission, this yields a negative value for W_λ. In the remainder of this work, we will employ the convention that a negative value of W_λ indicates a line in emission, while a positive value indicates a line in absorption.

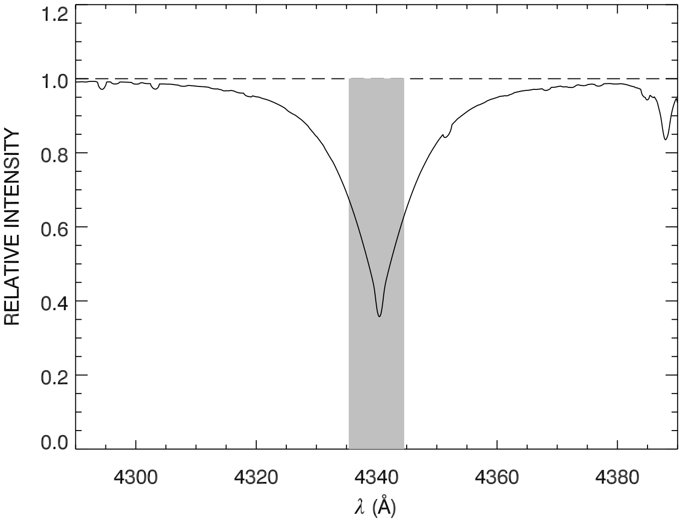

Figure 5.1 Integrating over a line profile to yield a measure of the line $W_{H\alpha}$, which corresponds to the width of a rectangular box having the same area as the spectral line.

We have measured $W_{H\alpha}$ for our sample of Be stars from multiple observing runs: 2009 October, 2009 December, 2010 August, and 2012 August using WIRO; 2012 January using the KPNO CF. Details for these observations can be found in Table 2.1. The results of our measurements are compiled in Table 5.1. Shown in Figure 5.2 are compilations of Hα observations for NGC 884–1702 and NGC 884–1926. These plots provide examples of the significant variability we have found in these cluster Be stars. A complete set of Hα spectra for our sample Be stars is included in Appendix

A.

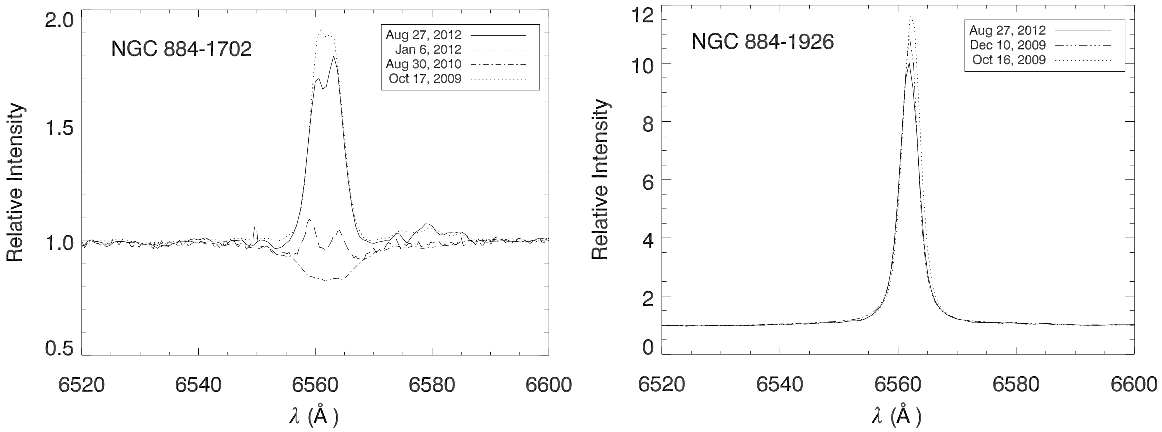

Figure 5.2 Hα spectra of the stars NGC 884–1702 (left) and NGC 884–1926 (right) are shown as examples of the variability of disk strengths observed.

To consider our results further, we combine stars from both clusters and determine their average and maximum $W_{H\alpha}$ from all available observations. We also compute the 1σ variance of $W_{H\alpha}$ for each star, to be used as a measure of observed variability. Shown in Figure 5.3 are the compilations of the combined results for both clusters. These plots illustrate that most Be stars in our sample have disks of moderate strength, and exhibit some level of variability. A few stars in our sample have exceptionally strong disks and/or show large variations over the course of our observations.

Given our relatively small sample size it is difficult to determine if any trend is present in our data between $T_{\rm eff}$ (ie. spectral type) and average $W_{H\alpha}$, maximum $W_{H\alpha}$, or 1σ variance of $W_{H\alpha}$. In an effort to broaden our sample, we also include the results of 29 Be stars from several southern open clusters observed by McSwain et al. [2009]. The plots of Figure 5.4 combine our NGC 869 and NGC 884 results with those of McSwain et al. [2009]. Although it does appear that the hotter stars in our sample have the largest disk structures, for the bulk of our sample and that of McSwain et al. [2009] there is a wide range of disk sizes for a given spectral type. Overall, we find no significant trends between average $W_{H\alpha}$, maximum $W_{H\alpha}$, or 1σ variance of $W_{H\alpha}$ and spectral type.

Table 5.1. Be Star Hα Equivalent Widths

WEBDA ID	**HJD -2,455,000 (2009 Oct.)**	$W_{H\alpha}$ **(Å)**	**HJD -2,455,000 (2009 Dec.)**	$W_{H\alpha}$ **(Å)**	**HJD -2,455,000 (2010 Aug.)**	$W_{H\alpha}$ **(Å)**	**HJD -2,455,000 (2011 Nov.)**	$W_{H\alpha}$ **(Å)**	**HJD -2,455,000 (2012 Jan.)**	$W_{H\alpha}$ **(Å)**	**HJD -2,455,000 (2012 Aug.)**	$W_{H\alpha}$ **(Å)**
NGC 869												
49	122.787	-21.56	...	...	437.751	-17.42	872.835	-10.37	...	...	1167.653	-11.51
146	...	...	...	...	437.765	3.39	...	...	928.718	3.22	1167.662	3.18
309	...	...	...	...	437.780	-43.75	...	...	...	...	1167.679	-39.70
517	121.910	-4.97	...	...	439.733	-2.14	...	...	930.656	-7.50	1167.688	-4.57
566	121.839	1.20	...	...	437.792	-0.86	...	...	930.640	-5.20	1167.573	-2.05
717	...	...	...	...	437.832	3.55	871.832	2.61	930.694	2.76	1167.588	3.34
846	...	...	176.608	-3.85	437.873	-4.37	...	...	...	...	1168.603	-2.27
847	122.796	-4.64	...	...	437.853	-4.61	871.810	-5.00	...	...	1168.585	-4.21
992	...	...	...	...	437.906	0.71	...	...	...	...	1168.656	0.45
1057	...	...	...	...	437.737	-0.53	...	...	928.747	-0.13	1167.583	-0.87
1161	121.892	-16.15	...	...	440.848	-15.45	...	...	...	...	1168.644	-15.83
1261	122.881	-67.70	176.588	-69.43	437.927	-68.75	...	...	...	...	1168.630	-69.35
1268	...	...	...	...	437.940	3.18	...	...	932.618	2.48	1168.636	3.15
1278	...	...	176.713	-4.17	440.902	-4.92	...	...	...	...	1169.610	-1.15
1282	...	...	176.644	-6.60	440.870	-10.87	...	...	...	...	1169.584	-6.93
NGC 884												
1702	122.860	-5.86	...	...	439.784	2.94	...	...	932.645	0.48	1167.596	-4.90
1772	...	...	...	...	...	...	...	...	...	...	1169.643	-0.60
1926	121.852	-48.89	176.846	-44.77	...	...	...	...	...	...	1167.614	-43.38
1977	...	...	176.782	-27.19	...	...	...	...	...	...	...	...
2088	122.837	-9.22	...	...	439.837	-5.65	...	...	...	...	1167.620	-10.57
2091	...	...	176.736	-26.27	...	...	...	...	...	...	1167.634	-26.07
2138	122.806	-22.72	176.837	-24.64	439.856	-23.38	...	...	...	...	1168.677	-23.80
2165	121.872	-11.87	...	...	439.876	-11.44	...	...	934.803	-16.13	1168.680	-16.50
2262	...	...	...	...	440.739	3.19	...	...	...	...	1169.672	3.27
2284	121.828	-72.90	176.598	-74.96	439.892	-76.20	...	...	...	...	1168.691	-73.22
2563	123.928	-49.80	...	...	...	...	...	...	...	...	...	...
2771	...	...	176.858	-25.12	...	...	...	...	...	...	...	...

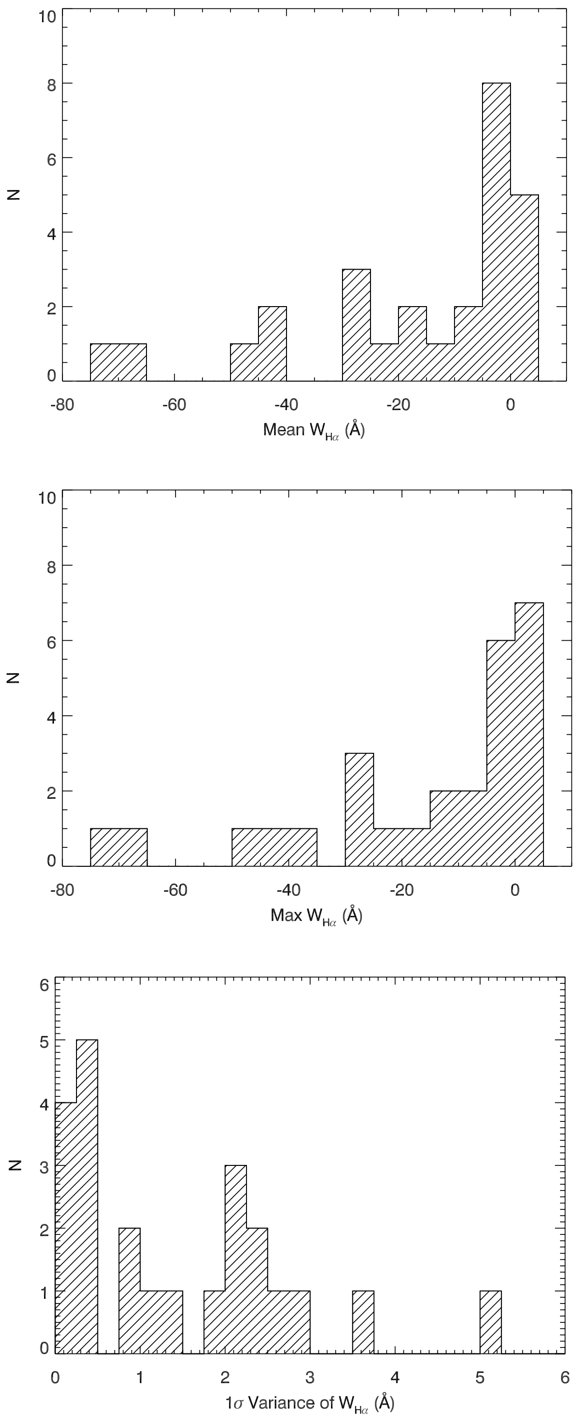

Figure 5.3 Histograms illustrating the average $W_{H\alpha}$, maximum $W_{H\alpha}$, and 1σ variance of $W_{H\alpha}$ of Be star disks in NGC 869 and NGC 884.

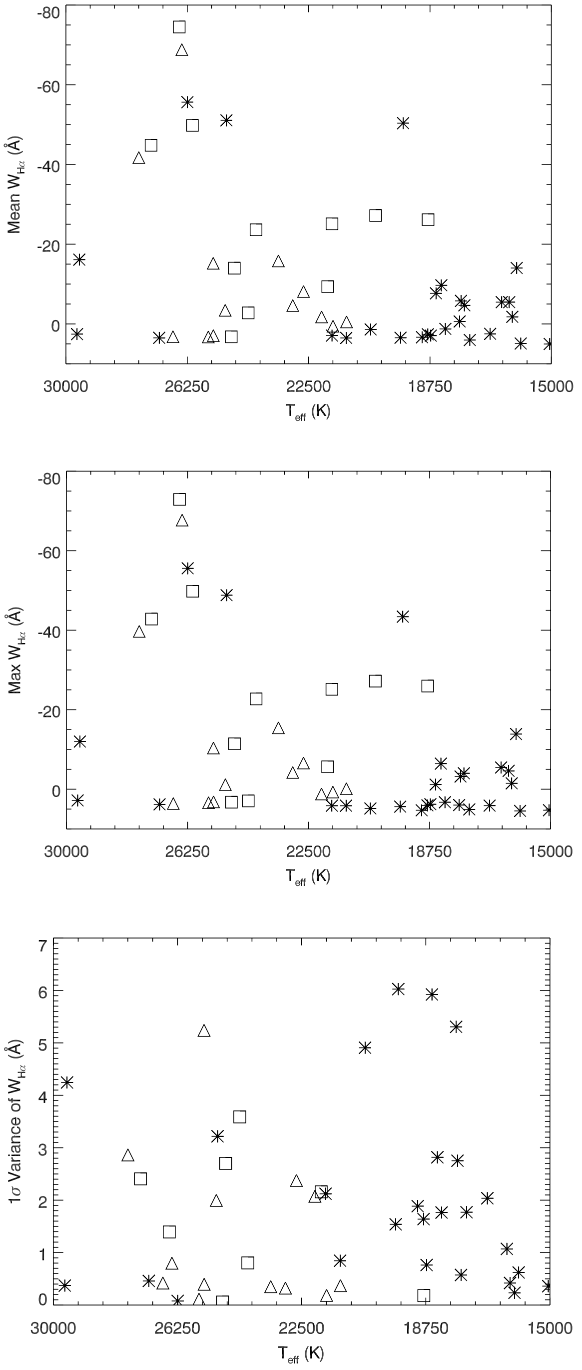

Figure 5.4 Plots of T_{eff} and average $W_{H\alpha}$, maximum $W_{H\alpha}$, and 1σ variance of $W_{H\alpha}$ for NGC 869 *(triangles)*, NGC 884 *(squares)*, and the results of McSwain et al. [2009] *(asterisks)*.

5.2 Modeling Be Stars from $H\alpha$ Emission

Using our $H\alpha$ observations, we can further quantify the physical parameters of the Be star disks by utilizing the numerical circumstellar disk models of Grundstrom & Gies [2006]. These models use observed $W_{H\alpha}$ to determine the radius of half light, R_d, and disk base density, ρ_0 for a given Be star.

In their models it is assumed that the disk is isothermal and geometrically thin, and that an inner optically thick region of the disk, which appears as an ellipse when projected onto the plane of the sky, dominates the $H\alpha$ line emission. To further simplify the analysis, the specific intensity of the disk emission, I_λ^d, is assumed to be isotropic. With these assumptions in place, the $H\alpha$ flux integrated over wavelength then depends on the product of the surface flux, the wavelength range over which $H\alpha$ is optically thick, and the projected solid angle, given as

$$F(H\alpha) = \pi I_\lambda^d \left\langle \Delta\lambda \right\rangle \cos i \left(\frac{R_{disk}}{r} \right)^2 , \tag{5.2}$$

where $\langle \Delta\lambda \rangle$ is the wavelength region over which the line is optically thick, i is the disk inclination, R_{disk} is the radius of the optically thick disk, and r is defined as the distance to the star. This flux is measured via the equivalent width of emission, W_λ, given in wavelength units relative to the local continuum flux, thus the above equation can be rewritten as

$$F(H\alpha) = |W_\lambda|(1+\epsilon)\pi I_\lambda^\star \left(\frac{R_\star}{r} \right)^2 . \tag{5.3}$$

Here ϵ defines the ratio of disk continuum flux to stellar flux within the $H\alpha$ region, $I_\lambda^\star$ is the stellar specific intensity near $H\alpha$, and $R_\star$ is the radius of the star. Equating these two expressions of $F(H\alpha)$ then provides the predicted relationship between the ratio of the disk to stellar radius, and $W_{H\alpha}$,

$$\frac{R_{disk}}{R_\star} = \sqrt{\frac{I_\lambda^\star}{I_\lambda^d} \frac{W_\lambda (1+\epsilon)}{\langle \Delta\lambda \rangle \cos i}}. \tag{5.4}$$

To further account for the model specific dependencies on disk temperature, inclination, and density, Grundstrom & Gies [2006] adopt the disk model approach of

Hummel & Vrancken [2000], which is detailed in Chapter 1. In this model approach the disk is assumed to be axisymmetric (symmetric about the vertical axis), and centered over the stellar equator. The disk gas density is given by Equation 1.19,where the disk base density at the stellar equator is given by ρ_0, and $H(r)$ defines the disk scale height, which is given by Equation 1.20. By equating the photoionization and recombination rates, as described by Gies et al. [2007], the neutral hydrogen population within the disk can be found. These models are used to produce a large grid of radial and surface elements, where the equation of radiative transfer is then solved along a ray passing through the center of each element. This spatial image produced of the star + disk system in the plane of the sky is then collapsed and summed as described in their work to determine where the summed intensity drops to half of its maximum value. This value is adopted as the effective radius of the disk, R_{disk}.

For the model inputs, we use our determined values of $T_{\rm eff}$ and $R_\star$, measured $W_{H\alpha}$, disk inclination, i, disk outer boundary of 100 $R_\star$, and disk continuum dilution factor of 0.0033 [Dachs et al., 1988]. Shown in Figures 5.5(a) and 5.5(b) are the resulting effective radii and disk base densities of our sample Be stars. These results suggest, in agreement with our $W_{H\alpha}$ analysis, that a majority of our sample Be stars have disks less than a few stellar radii in size.

With the resulting estimates of disk radius and disk base density, we can further estimate the mass contained in each Be star disk at the time of each of our H_α observations following the method detailed by McSwain et al. [2008]. To determine disk mass, we use an axisymmetric, isothermal density distribution [Carciofi & Bjorkman, 2006] given by Equation 1.19. The disk scale height, $H(r)$ is given by Equations 1.21 -1.23. Analytically integrating this distribution over the full radius and thickness of the disk gives the total mass contained in the disk, and is done for each observation of $W_{H\alpha}$. With multiple epochs of $W_{H\alpha}$ observations for our sample Be stars, we can examine the changes in disk radius and density over time, and therefore investigate the disk mass loss and or gain at the time of each measurement. Shown in Figure 5.5(c) is a zoomed in portion of the plot demonstrating the changes in disk mass over time for sample Be stars. We find that nearly all of our sample Be star disks are gaining or losing mass to some degree over the 4 year span of our observations. The resultant values of R_{disk}, ρ_0, and M_{disk} with $i = 60^\circ$ for each observation of the sample Be stars are given in Table 5.2.

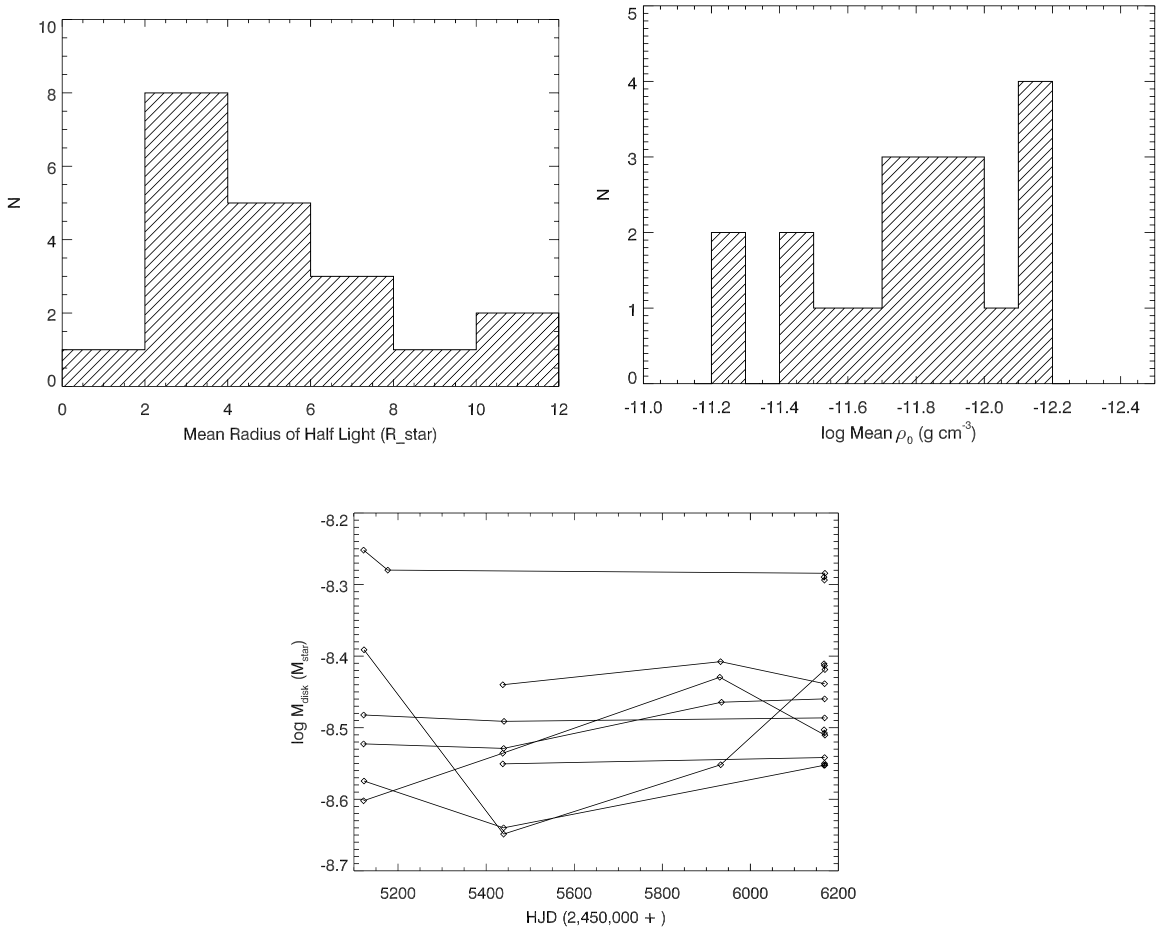

Figure 5.5 Top: Histograms of mean effective radius, in units of $R_\star$ (left), and log mean ρ_0 (right). Bottom: Zoomed in portion of $\log M_{disk}$ vs. HJD plot.

Table 5.2. Be Star Disk Parameters from Hα Equivalent Widths

WEBDA ID	**HJD -2,455,000**	$\mathbf{R}_{disk}$ $i = 0^\circ$ (R$_\odot$)	$\mathbf{R}_{disk}$ $i = 30^\circ$ (R$_\odot$)	$\mathbf{R}_{disk}$ $i = 60^\circ$ (R$_\odot$)	$\mathbf{R}_{disk}$ $i = 80^\circ$ (R$_\odot$)	ρ_0 1.0×10^{-12} (g cm^{-3})	$\mathbf{M}_{disk}$ $i = 60^\circ$ (M$_\odot$)
NGC 869							
49	122.788	51.1	54.4	65.7	77.7	2.3	2.3e-07
49	437.752	47.1	50.1	60.0	70.5	2.1	2.1e-07
49	872.836	39.7	42.1	49.6	57.4	1.6	1.6e-07
49	1167.654	41.0	43.5	51.4	59.6	1.7	1.7e-07
146	437.766	14.2	14.1	14.6	15.4	0.7	1.6e-08
146	928.719	14.3	14.3	14.9	15.8	0.7	1.7e-08
146	1167.662	14.4	14.3	15.0	15.9	0.7	1.7e-08
309	437.780	54.2	58.1	71.8	86.4	3.5	1.8e-07
309	1167.679	51.7	55.4	68.2	81.8	3.3	1.7e-07
566	121.840	19.8	20.5	22.7	25.0	0.9	2.7e-08
566	437.793	22.4	23.5	26.6	29.7	1.0	3.1e-08
566	930.640	27.3	28.9	33.6	38.4	1.3	4.0e-08
566	1167.573	23.9	25.1	28.6	32.2	1.1	3.4e-08
566	1168.501	23.7	24.9	28.3	31.8	1.1	3.4e-08
566	1169.500	23.5	24.8	28.2	31.6	1.1	3.3e-08
717	437.832	11.4	11.3	11.6	12.1	0.7	8.2e-09
717	871.833	12.1	12.1	13.0	14.1	0.8	9.1e-09
717	930.695	12.0	12.0	12.8	13.8	0.8	9.0e-09
717	1167.589	11.6	11.5	11.9	12.5	0.7	8.4e-09
717	1168.516	11.4	11.2	11.5	11.9	0.7	8.2e-09
717	1169.514	11.5	11.4	11.9	12.5	0.7	8.4e-09
847	122.797	37.6	39.7	45.8	52.0	1.3	1.6e-07
847	437.853	37.5	39.6	45.7	52.0	1.3	1.6e-07
847	871.811	38.1	40.3	46.5	53.0	1.3	1.6e-07
847	1168.586	36.9	39.0	44.8	50.9	1.3	1.6e-07
992	437.907	21.2	22.0	24.6	27.2	0.9	3.0e-08
992	1168.657	21.5	22.4	25.1	27.8	0.9	3.1e-08
1161	121.892	31.0	32.9	39.5	46.5	2.0	3.7e-08
1161	440.849	30.5	32.4	38.9	45.7	1.9	3.6e-08
1161	1168.644	30.8	32.7	39.2	46.2	2.0	3.6e-08
1261	122.882	67.5	72.7	93.0	114.9	5.0	2.1e-07
1261	176.588	68.6	73.9	94.7	117.2	5.2	2.1e-07
1261	437.927	68.2	73.4	94.0	116.3	5.1	2.1e-07
1261	1168.630	68.6	73.9	94.6	117.1	5.2	2.1e-07
1268	437.941	19.7	19.6	20.6	21.8	0.7	5.3e-08
1268	932.618	20.6	20.7	22.3	24.1	0.8	5.7e-08
1268	1168.636	19.7	19.6	20.6	21.9	0.7	5.3e-08
1278	176.714	11.5	12.1	13.9	15.7	1.3	2.7e-09
1278	440.902	11.8	12.4	14.4	16.3	1.3	2.8e-09

Table 5.2 (cont'd)

WEBDA ID	**HJD -2,455,000**	$\mathbf{R}_{disk}$ $i = 0^\circ$ ($R_\odot$)	$\mathbf{R}_{disk}$ $i = 30^\circ$ ($R_\odot$)	$\mathbf{R}_{disk}$ $i = 60^\circ$ ($R_\odot$)	$\mathbf{R}_{disk}$ $i = 80^\circ$ ($R_\odot$)	ρ_0 1.0×10^{-12} (g cm^{-3})	$\mathbf{M}_{disk}$ $i = 60^\circ$ ($M_\odot$)
1278	1169.611	9.9	10.4	11.7	13.1	1.1	2.2e-09
1282	176.644	17.9	18.9	22.1	25.4	1.4	8.0e-09
1282	440.871	20.4	21.6	25.6	29.9	1.7	9.5e-09
1282	1169.585	18.1	19.1	22.3	25.7	1.4	8.1e-09
NGC 884							
1702	122.860	27.3	28.9	33.5	38.2	1.4	5.1e-08
1702	439.785	17.2	17.3	18.3	19.6	0.8	2.8e-08
1702	932.646	20.2	20.9	23.2	25.7	0.9	3.5e-08
1702	1167.596	26.3	27.8	32.0	36.5	1.3	4.9e-08
1702	1168.527	26.2	27.6	31.9	36.2	1.3	4.8e-08
1702	1169.527	26.0	27.3	31.5	35.8	1.3	4.8e-08
1926	121.852	45.2	48.5	60.4	73.0	3.8	7.8e-08
1926	176.846	43.3	46.4	57.5	69.3	3.6	7.3e-08
1926	1167.615	42.6	45.7	56.5	68.0	3.5	7.1e-08
1926	1168.537	42.4	45.4	56.1	67.5	3.5	7.1e-08
1926	1169.537	43.0	46.1	57.1	68.7	3.6	7.2e-08
1977	176.783	18.2	19.4	23.9	28.8	2.6	2.1e-09
2088	122.838	27.0	28.6	33.9	39.4	1.6	2.7e-08
2088	439.837	24.0	25.4	29.6	33.9	1.4	2.3e-08
2088	1167.621	28.1	29.8	35.4	41.3	1.7	2.8e-08
2088	1168.548	28.2	29.9	35.6	41.6	1.7	2.8e-08
2088	1169.544	28.1	29.8	35.4	41.4	1.7	2.8e-08
2091	176.737	25.6	27.4	33.9	40.8	2.6	5.9e-09
2091	1167.635	25.6	27.3	33.8	40.7	2.5	5.8e-09
2091	1168.558	25.5	27.3	33.7	40.6	2.5	5.8e-09
2091	1169.557	25.7	27.4	33.9	40.9	2.6	5.9e-09
2138	122.806	51.3	54.6	66.3	78.7	2.4	1.9e-07
2138	176.838	53.0	56.5	68.7	81.8	2.5	2.0e-07
2138	439.857	51.9	55.3	67.1	79.8	2.4	1.9e-07
2138	1168.677	52.3	55.7	67.7	80.5	2.4	2.0e-07
2165	121.872	27.8	29.4	34.8	40.5	1.7	3.6e-08
2165	439.877	27.4	29.1	34.4	40.0	1.7	3.5e-08
2165	934.804	30.7	32.6	39.1	45.9	2.0	4.1e-08
2165	1168.681	31.0	32.9	39.4	46.3	2.0	4.1e-08
2262	440.739	15.1	15.0	15.8	16.7	0.7	1.9e-08
2262	1169.673	15.0	14.9	15.6	16.5	0.7	1.8e-08
2284	121.828	66.6	71.8	92.4	114.7	5.4	1.8e-07
2284	176.598	67.9	73.2	94.5	117.5	5.6	1.8e-07
2284	439.893	68.7	74.1	95.7	119.1	5.6	1.9e-07
2284	440.767	68.1	73.4	94.7	117.8	5.6	1.9e-07

Table 5.2 (cont'd)

WEBDA ID	**HJD -2,455,000**	$\mathbf{R}_{disk}$ $i = 0°$ (R$_\odot$)	$\mathbf{R}_{disk}$ $i = 30°$ (R$_\odot$)	$\mathbf{R}_{disk}$ $i = 60°$ (R$_\odot$)	$\mathbf{R}_{disk}$ $i = 80°$ (R$_\odot$)	ρ_0 1.0×10^{-12} (g cm^{-3})	$\mathbf{M}_{disk}$ $i = 60°$ (M$_\odot$)
2284	1168.692	66.8	72.1	92.8	115.1	5.4	1.8e-07
2563	123.928	36.6	39.3	49.1	59.6	3.9	3.0e-08
2771	176.859	26.0	27.7	34.0	40.6	2.5	1.0e-08

We note that varying the value of the disk inclination in these models has no effect on the resultant density. Realistically this is likely to be incorrect, however these calculated disk base densities do provide a first-order estimate that will allow us to place further constraints on the disk parameters.

5.3 Be Star SEDs

To examine the observed SEDs for our sample Be stars, we utilize the same method described for the sample B-type stars to normalize the model flux to angular size but now fix the cluster distance at the mean value determined by the resultant distributions of distances yielded from the absolute magnitude method described in Chapter 4. An example of a resultant Be SED is shown in Figure 5.6. The 1σ variance of the absolute magnitude distance distributions are used as error bars for the cluster distances to produce high and low error SEDs, shown as the dotted and dashed model SEDs, respectively, in Figure 5.6. A complete set of SEDs for our sample Be stars can be found in Appendix A. We find good agreement between the optical region of the observed SEDs, where the disk contribution to the flux is negligible, and results of our normalized models. The observed IR flux excess of each star is then determined by taking the difference between the observed fluxes and the corresponding model flux as determined by our measurements of T_{eff} and log g_{pol}. These observed IR flux excesses will be utilized in the following section to compare to the predicted IR flux excesses of the Touhami et al. [2011] models.

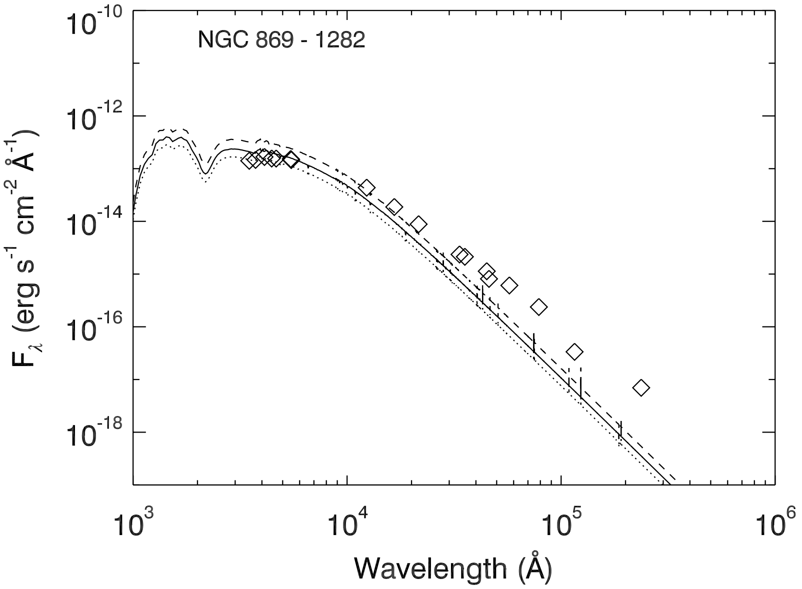

Figure 5.6 Example SED of Be Star NGC 869 - 1282. Observed photometric magnitudes (diamonds) shown with model SED using measured $T_{\rm eff}$ and log $g_{\rm pol}$ (solid line) from Chapter 3. SEDs using high and low E$(B-V)$ errors shown by dotted and dashed lines, respectively.

5.4 Modeling Be Star Disks Using IR Excesses

To further constrain the predicted disk parameters from Section 5.2, we employ the radiative transfer models of Touhami et al. [2011]. These models provide a parameterization of an assumed isothermal viscous decretion disk. These models are parameterized by the physical parameters ρ_0, n, the disk-to-star temperature ratio $T_{disk}/T_\star$, and the outer boundary disk radius R_{disk}, as well as the observable parameters of λ and i. Like the work of Grundstrom & Gies [2006], these models use a gas density distribution given by Equation 1.19. The disk base density is ρ_0, and the radial density exponent is given as $n = 3$. The disk scale height, $H(r)$, is again defined by Equation 1.20. The Touhami et al. [2011] models, again, follow the methods detailed by Hummel & Vrancken [2000] for solving the equation of radiative transfer along a grid of sight lines through elements surrounding the star and disk. Analytically solving this equation at each point of this grid provides a solution to how photons of different wavelengths are transported through the gaseous disk material to the surface and radiated away.

To understand the physical basis for these models, we begin by considering the equation of radiative transfer

$$\frac{dI_\nu}{d\tau_\nu} = S_\nu - I_\nu. \tag{5.5}$$

By introducing an integrating factor e^τ, this expression becomes

$$\frac{d}{d\tau}(I_\nu e^\tau) = e^\tau \frac{\partial I_\nu}{\partial \tau} + I_\nu e^\tau = e^\tau S_\nu. \tag{5.6}$$

Integrating this expression from 0 to τ yields the integral solution to the transfer equation

$$I_\nu(\tau) = I_\nu(0)e^{-\tau} + \int_0^\tau S_\nu e^{-(\tau-\tau')} d\tau'. \tag{5.7}$$

Assuming the source function S_ν is constant, this expression becomes the general solution to the equation of radiative transfer

$$I_\nu(\tau_\nu) = I_\nu(0)e^{-(\tau_c+\tau_\nu)} + S_\nu(1 - e^{-\tau_\nu}), \tag{5.8}$$

where the total optical depth τ is produced by contributions from both the continuum optical depth τ_c and frequency-dependent line optical depth τ_ν, such that $\tau = \tau_c + \tau_\nu$. The first term of this expression accounts for the attenuation of the incident intensity by both the continuum and line sources, while the second describes the emission produced by line sources.

For these Be star models the resultant continuum-subtracted intensity emerging from the emission layer in consideration is given by [Horne & Marsh, 1986]

$$I_\nu = [I_\nu(0)e^{-\tau_\nu} + S_L(1 - e^{-\tau_\nu})]e^{-\tau_c} - I_\nu(0)e^{-\tau_c}. \tag{5.9}$$

The total opacity in the IR is primarily produced by free-free and bound-free emission processes. The line source function of the emission layer is given by S_L, which is assumed to be constant throughout the layer, and the intensity of the background radiation is given by $I_\nu(0)$. Comparing this expression that derived in Equation 5.8 we see that the first term describes the absorption of incident stellar radiation by line sources in the disk, and further attenuation by the continuum. The second term accounts for the line emission produced by the disk, which is also attenuated by the continuum as it may be absorbed in other physical regions of the disk. The $-I_\nu(0)e^{-\tau_c}$ term removes the stellar continuum contributions from the total system intensity, thus leaving us with the intensity contributions from the disk.

Given our determined values of $T_{\rm eff}$, $R_\star$, and $M_\star$, mean predicted ρ_0 from the Grundstrom & Gies [2006] models, and inclination, i, the modeled IR excess for six wavelength bands is calculated. This approximate disk SED is then plotted against the available observed IR excesses, determined from the Be SEDs described in the previous section.

Shown in Figure 5.7 are the resultant models of IR flux excess for the value of ρ_0 as determined by the models of Grundstrom & Gies [2006], and for the value of ρ_0 which fits the observed IR flux excess. Similar figures are available for the remaining sample Be stars in Appendix A. We find that this second value of ρ_0 is typically ~ 1 order of magnitude larger than that given by the Grundstrom & Gies [2006] models, which suggests that there is some systematic discrepancy between the two disk models. It is also apparent from this figure that there is a strong correlation between i and ρ_0 which must be resolved before firm disk parameters can be established. The disk parameters determined for the average $W_{H\alpha}$ of each star are compiled in Table 5.3, along with the the value of ρ_0 that yields an approximate fit to the observed IR flux excesses for $i = 30^\circ$, 60°, and 80°.

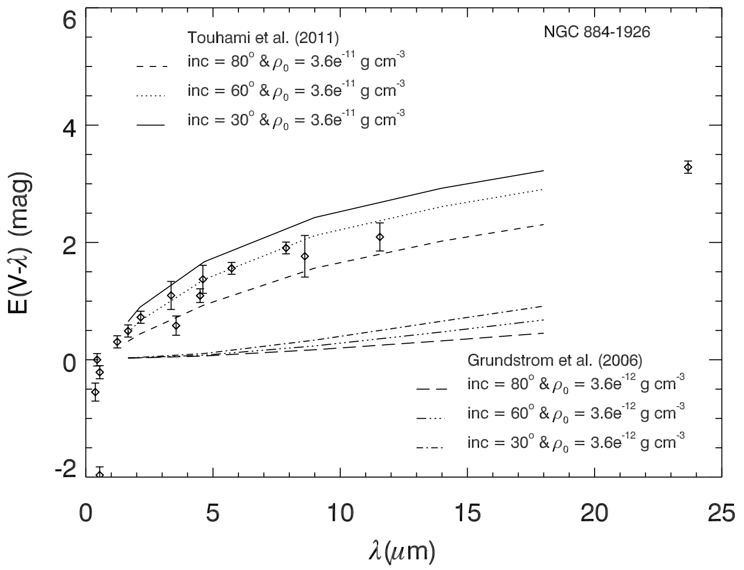

Figure 5.7 Example Be disk SED of NGC 884-1926. Here the stellar flux contribution has been subtracted out of the total system flux, leaving only the IR flux produced by the disk. Observed disk flux (diamonds) is shown with multiple models of the IR excess using different values of i and ρ_0, as noted in the plot legend.

Table 5.3. Be Star Disk Parameters from IR Excesses

WEBDA ID	**Mean W$_{H\alpha}$ (Å)**	**Mean R$_{disk}$** (R$_\odot$)	**Mean ρ_0** 1.0×10^{-12} (g cm^{-3})	**Mean M$_{disk}$** (M$_\odot$)	ρ_0 1.0×10^{-11} (g cm^{-3})
NGC 869					
49	-10.86	56.7	1.9	1.9e-07	1.9
309	-19.85	70.0	3.4	1.7e-07	3.4
566	-0.89	28.0	1.1	3.3e-08	1.1
847	-3.46	45.7	1.3	1.6e-07	1.3
992	0.22	24.8	0.9	3.0e-08	0.9
1161	-10.66	39.2	2.0	3.6e-08	2.0
1261	-51.62	94.1	5.1	2.1e-07	5.1
1278	-1.77	13.3	1.2	2.5e-09	1.2
1282	-4.51	23.4	1.5	8.5e-09	1.5
NGC 884					
1926	-44.80	57.5	3.6	7.3e-08	3.6
1977	-27.19	23.9	2.6	2.1e-09	2.6
2088	-8.22	34.0	1.6	2.7e-08	1.6
2091	-26.16	33.8	2.5	5.8e-09	2.5
2138	-17.79	67.5	2.4	1.9e-07	2.4
2165	-9.95	36.9	1.9	3.8e-08	1.9
2284	-44.22	94.0	5.5	1.8e-07	5.5
2563	-49.80	49.1	3.9	3.0e-08	3.9
2771	-25.12	34.0	2.5	1.0e-08	2.5

5.5 Summary/Conclusions

Through our 4 year baseline of Hα observations, and those compiled from the literature, we find that a large number of the Be stars in our sample exhibit a wide range of variability. With the significant number of transient Be stars residing in these clusters, h and χ Per provide an excellent northern hemisphere laboratory for investigating the mechanisms spurring Be star disk formation and loss. In our efforts to place constraints on the radii and densities of these Be star disks, we find significant discrepancies between current Be disk models. The densities yielded by the models of Grundstrom & Gies [2006] are ~ 1 order of magnitude lower than those which produce IR disk excesses via the Touhami et al. [2011] models that match the IR excesses we observe in these Be stars. Finding a reliable means for constraining the disk inclination is another pressing issue for these cluster stars, which are well beyond the current reach of IR interferometry.

Chapter 6

Conclusions and Further Work

With their plethora of massive stars, the double clusters h & χ Persei are an ideal laboratory in which to study a number of physical phenomena. While the field of massive star study is relatively small, and far less “sexy” than studies of exoplanets or dark matter, there are still a wide variety of open questions and unexplained physics to be found amongst these stars. Their brightness makes them ideal targets for smaller telescopes like those found on university campuses, which is incredibly advantageous given the current funding climate.

B-type and Be stars have become important targets for asteroseismology. In hot stars, different pulsation frequencies provide information about different layers of the stellar interior. The information gleaned from studies targeting B stars with NRPs is being used to improve current stellar structure and stellar evolution models. Doing so, however, requires accurately determined stellar surface parameters in order to set appropriate boundary conditions for these models. Accurate measures of effective temperature and surface gravity are essential to determining stellar radii for these models, as well as for determining stellar ages and evolutionary spin-down. Many B-type and Be stars in h and χ Per have been found to host NRPs, and there are on-going campaigns to observe and characterize the nature of the variable pulsations found in these stars [Krzesiński & Pigulski, 1997, Krzesiński et al., 1999, Saesen et al., 2010]. The interest in the pulsating stars of h and χ Per has necessitated improved measurements of stellar parameters for the cluster.

In this work we have measured V sin i, $T_{\rm eff}$, log $g_{\rm polar}$, $M_\star$, and $R_\star$ for 104 B-type and Be star members of NGC 869 and NGC 884 using spectroscopic modeling techniques and calculations from Strömgren photometry. Our determined values for $V \sin i$ are in good agreement with the earlier results of Huang & Gies [2006a], although there are some discrepancies in our measured temperatures and surface gravities due to our use of the more recently available non-LTE BSTAR2006 stellar models of Lanz & Hubeny [2007] and the possible contamination with Be stars and spectroscopic binaries. Because of the resulting over-estimation of log g, Huang & Gies [2006a] have underestimated the retention of initial angular momentum by the cluster members.

We find that the cluster members are significantly more evolved than found by previous measurements. We also identify 8 transient Be stars in h and χ Per. The Be stars in these clusters are also rotating more slowly than expected based upon other young open clusters. Further monitoring of the massive stellar constituents of these clusters and their rotation rates is well warranted.

The methods we have developed for modeling the stellar flux of B-type stars based upon our physical parameter measurements and the models of Lanz & Hubeny [2007], have allowed us to separate the stellar and disk flux contributions of observed Be star SEDs. With these techniques in hand, we can now conduct a survey of Northern hemisphere B and Be stars, providing a broader sample of stars for studies of massive star structure, evolution, and the Be phenomenon.

The substantial amount of variability we observe in the strength of the Hα emission in our sample Be stars further demonstrates the utility of these clusters to the Be star community. What better location to study the formation and dissipation mechanisms of these disk structures than a pair of clusters hosting a large fraction of B-type and Be stars, which are exhibiting high levels of short term (NRP's, line profile variations) and long term (disk growth and weakening, transients) variability.

We are hopeful that obtaining spectropolometric observations of these Be stars will allow us to constrain the disk inclination, breaking the model correlation with disk density and allowing us to unravel the order of magnitude discrepancy between the models of Grundstrom & Gies [2006] and Touhami et al. [2011]. In the future, we will also continue to work with Dr. Yamina Touhami to extend her disk excess models to longer IR wavelengths (i.e. 24μm *Spitzer*).

Observation of the full Balmer series and the decrement of the emission in these lines with progressively shorter wavelengths may provide further insight into the physical structure of these disks. In the near future, we are also seeking to form a collaboration with one of the two research camps producing Be disk atmospheric models, so that we may compare our observations to physical models as a further independent means of constraining the physical properties of the disks.

Appendix A

The Be Stars of h and χ Persei

Included in this appendix is a compilation of data and results for each of the 26 Be stars in our observed sample. For each star there is a stack of $H\alpha$ spectra from multiple observations spanning 4 years. Also included are the observed spectral energy distributions (SEDs) complied from the WEBDA, 2MASS, *Spitzer*, *WISE*, and *AKARI* databases.

A.0.1 Star 1057

Compiled spectroscopic observations of NGC 869-1057. From the spectral observations of this star it appears to be a more evolved giant type. It is likely that this star has been misclassified as a Be star due to the IR excess produced by it's stellar wind. We exclude it from any further Be star analysis.

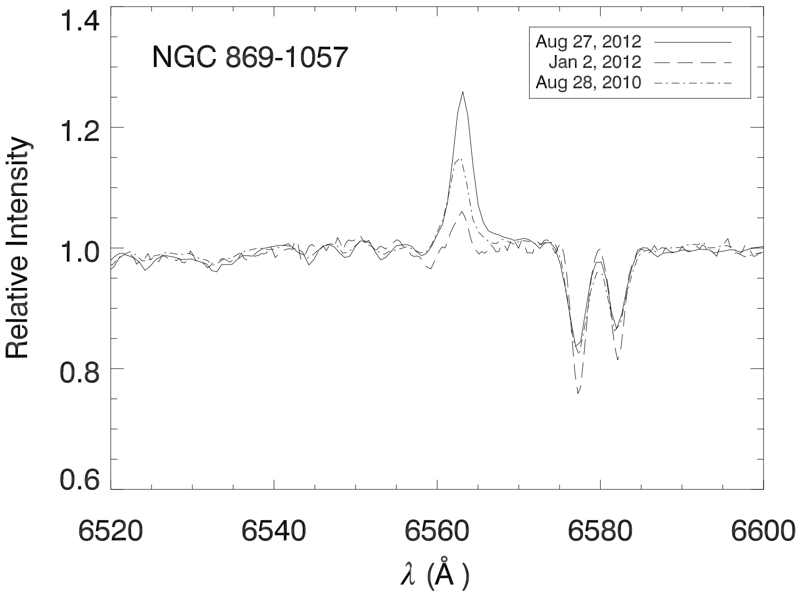

Figure A.1 Hα spectra of NGC 869-1057 in same format as Figure A.3.

A.0.2 Stars With Only Hα Observations

With the lack of available Strömgren photometry available for stars NGC 869–517, NGC 869–846, and NGC 884–1772, and the emission present in their Balmer lines, we are unable to determine appropriate values of $T_{\rm eff}$ and log g for them at this time. Without these measurements, we are unable to model the SEDs or IR excesses of these stars. Here we present the compilation of our Hα observations for these stars in Figure A.2.

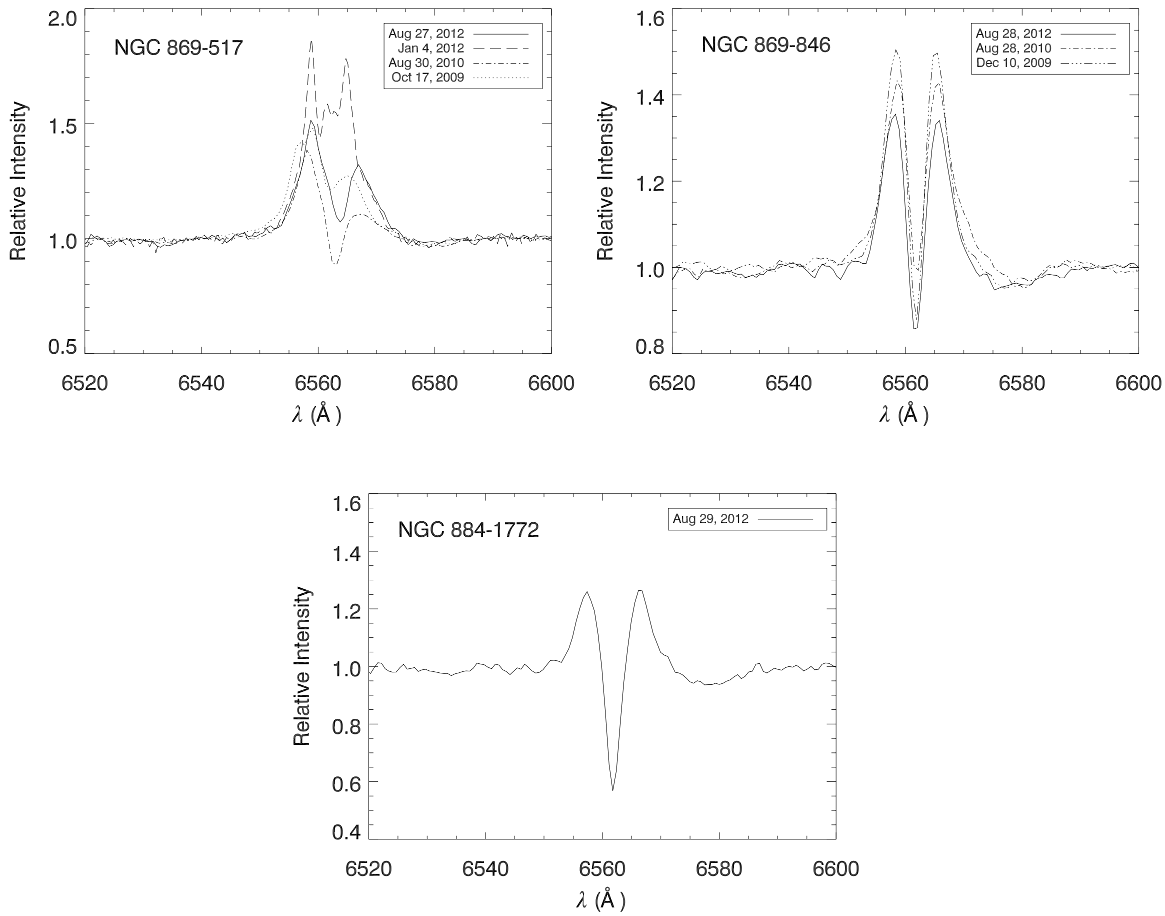

Figure A.2 Observed Hα spectra of NGC 869–517 (top left), NGC 869–846 (top right), and NGC 884–1772 (bottom). The different line styles correspond to different times of observation, as denoted in the legend of each plot.

A.1 NGC 869: h Per

A.1.1 Star 49

Compiled spectroscopic and photometric observations of NGC 869-49. With the determined temperature and surface gravity of this star, and its placement among the evolutionary tracks of Schaller et al. [1992], this star may be leaving the main sequence and moving onto the giant branch. Some variability is observed in the Hα emission of this star, as well in the observed SED, which may be due to a Be disk or a weak stellar wind if this star is more evolved.

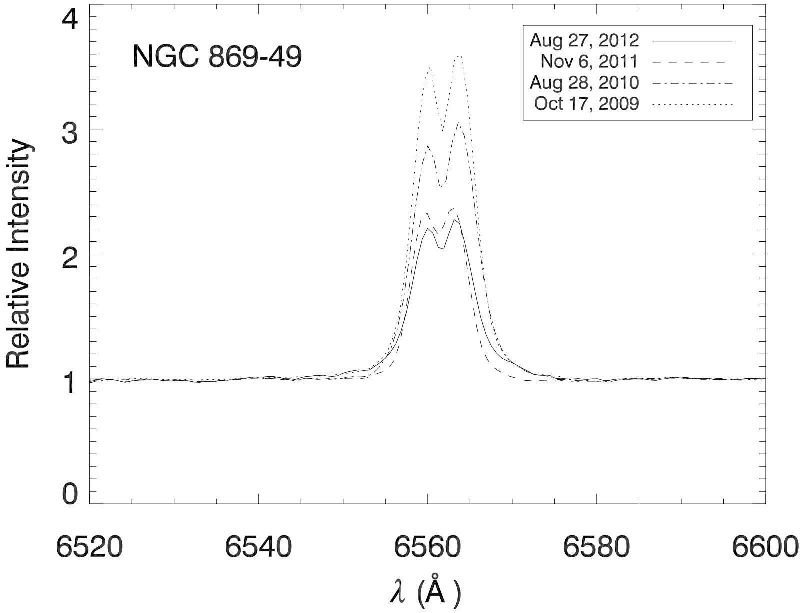

Figure A.3 Observed Hα spectra of NGC 869–49. Different line styles correspond to different times of observation, as noted in the plot legend.

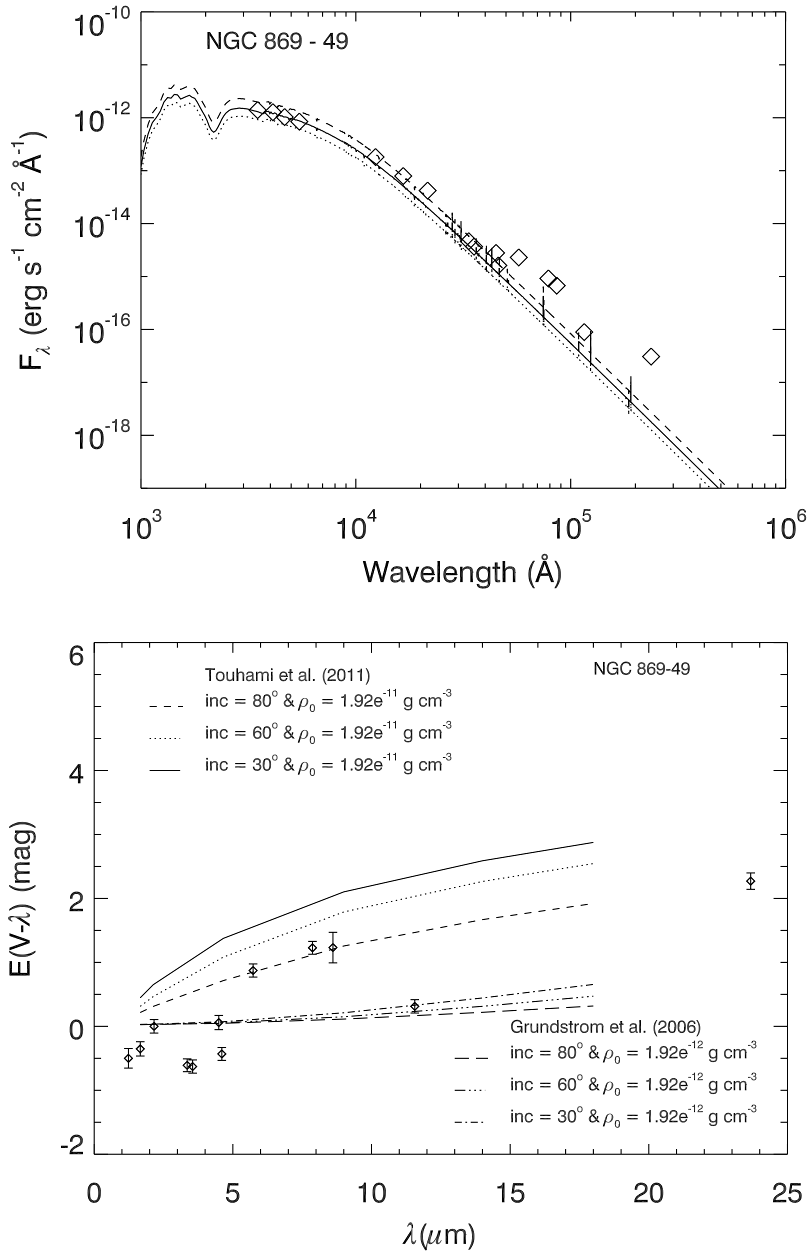

Figure A.4 *Top:* Observed photometric magnitudes (diamonds) with model SED using measured $T_{\rm eff}$ and log $g_{\rm pol}$ (solid line) from Chapter 3. SEDs using high and low E($B-V$) errors shown by dotted and dashed lines, respectively. *Bottom:* Observed IR flux excess as determined from photometric magnitudes and model SED (diamonds). Model IR excess for multiple values of i and ρ_0 (lines) as noted by plot legend.

A.1.2 Star 146

Compiled spectroscopic and photometric observations of NGC 869-146. This star neither exhibited any emission indicative of a Be disk at the times of our observations, nor does its observed SED show any signs of IR excess. This, with the observation of emission by Keller et al. [2001], is suggestive of this star being a transient Be star. As there is no observed IR excess for this star, we do not present any modeling of the IR excess.

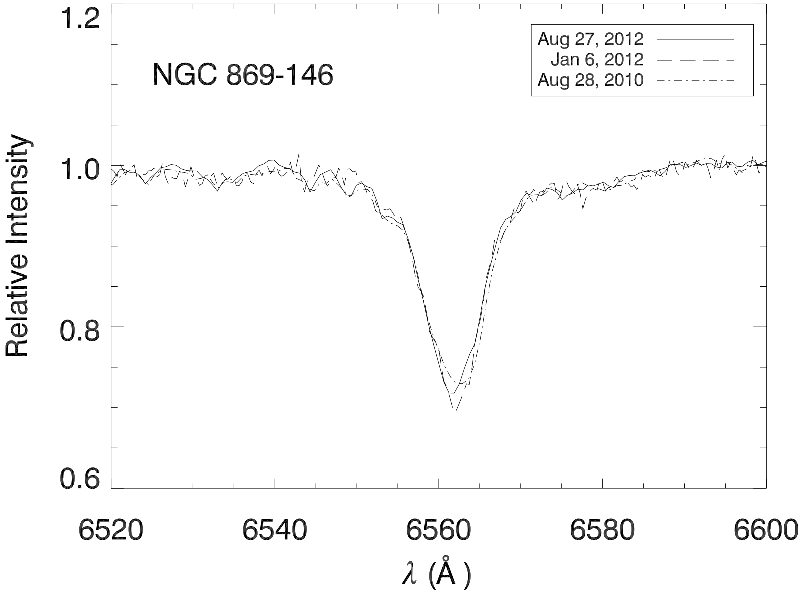

Figure A.5 Hα spectra of NGC 869-146 in same format as Figure A.3.

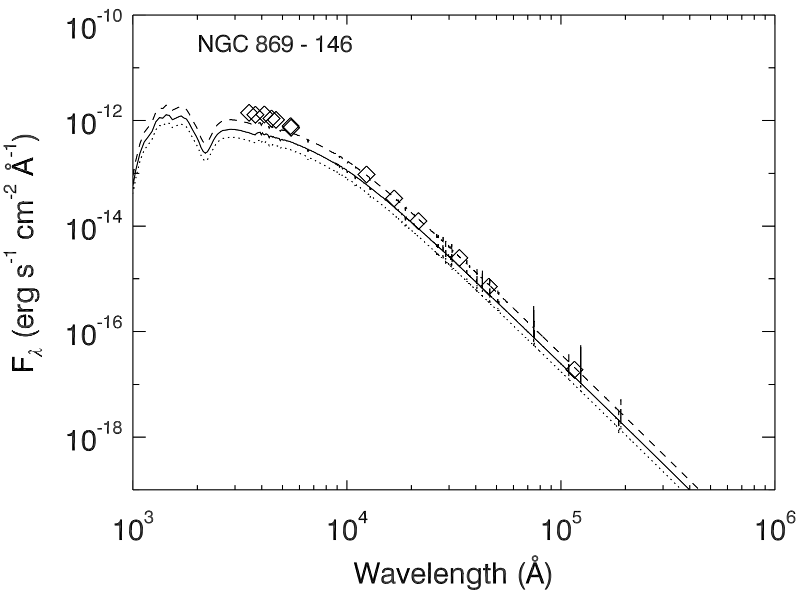

Figure A.6 Observed SED of NGC 869-146 in same format as Figure A.4.

A.1.3 Star 309

Compiled spectroscopic and photometric observations of NGC 869-309. This star has exhibited strong Hα emission at both times of our observations, showing some subtle variability in strength. The observed IR excess is well matched by the models of Touhami et al. [2011].

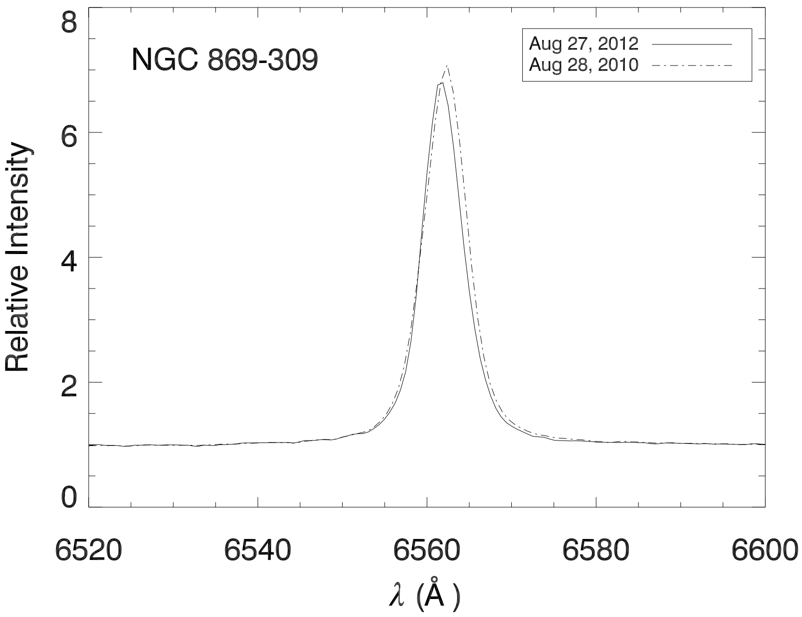

Figure A.7 Hα spectra of NGC 869-309 in same format as Figure A.3.

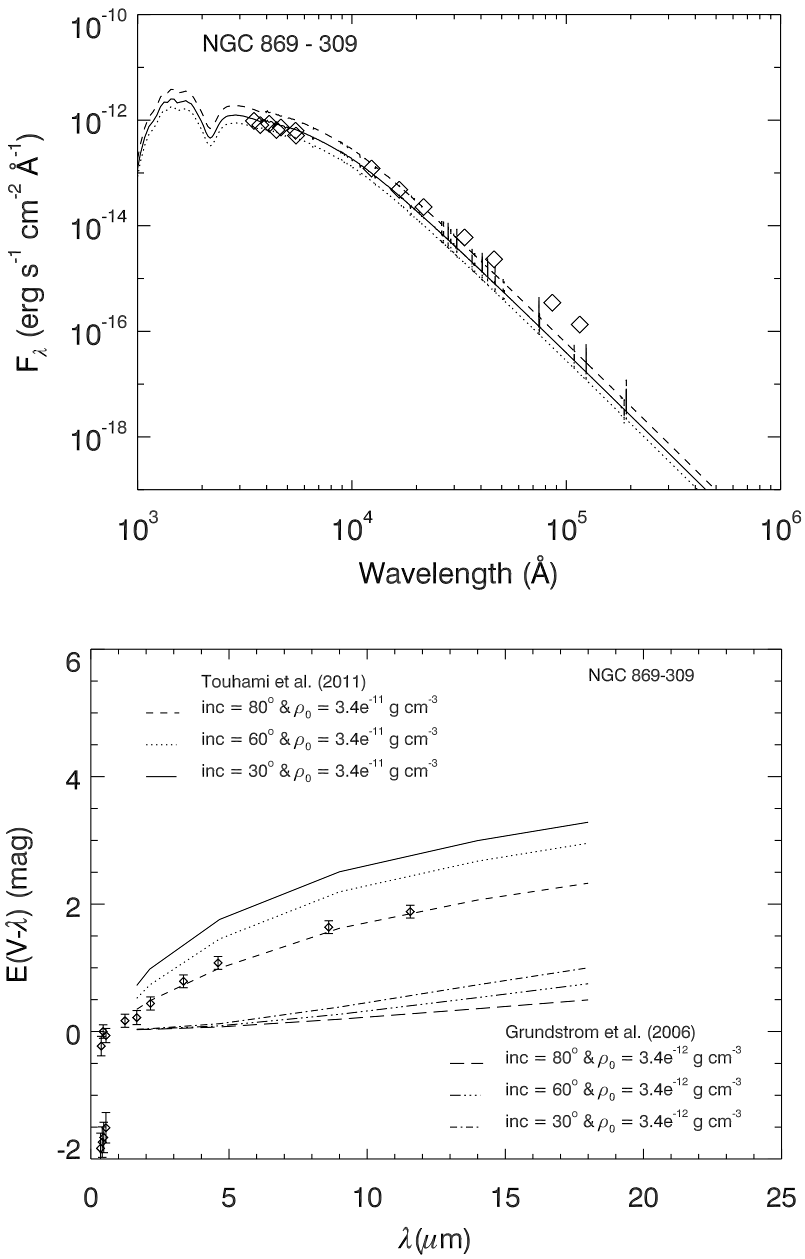

Figure A.8 Observed SED and disk excess of NGC 869-309 in same format as Figure A.4.

A.1.4 Star 566

Compiled spectroscopic and photometric observations of NGC 869-566. This Be star shows very clear variations in disk strength over the course of our Hα observations. Our review of the literature finds that it has been observed with and without signs of a disk on multiple occasions, making this a transient Be star. The majority of the photometric observations available appear to have been taken during phases with only a very weak disk, or no disk at all, preventing us from successfully modeling the IR excess of this star. However, with the highly transient nature of this star it would be an excellent target for investigating disk growth/loss events.

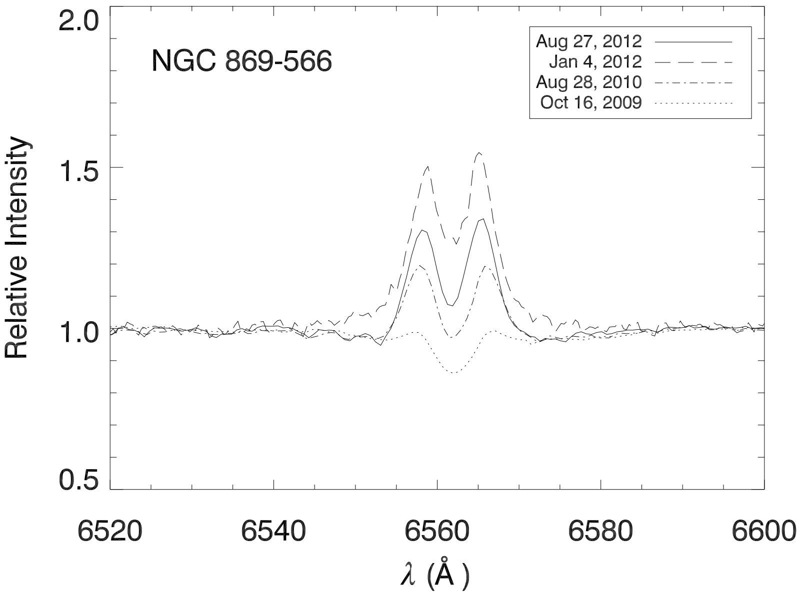

Figure A.9 Hα spectra of NGC 869-566 in same format as Figure A.3.

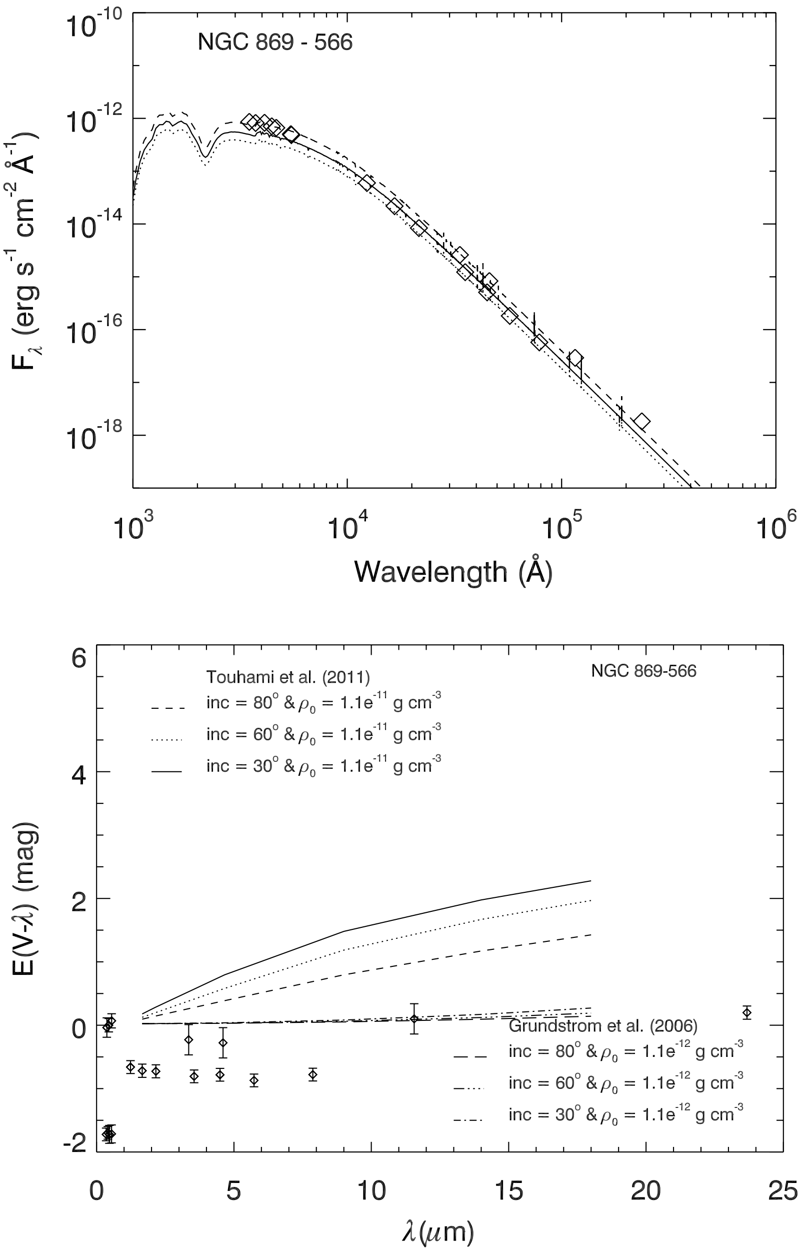

Figure A.10 Observed SED and disk excess of NGC 869-566 in same format as Figure A.4.

A.1.5 Star 717

Compiled spectroscopic and photometric observations of NGC 869-717. This star neither exhibited any emission indicative of a Be disk at the times of our observations, nor does its observed SED show any signs of IR excess. There does appear to be some small changes in the depth of the line core over time, but not enough to suggest the presence or growth of a disk. The observation of emission by Fabregat et al. [1994], is suggestive of this star possibly being a transient Be star. As there is no observed IR excess for this star, we do not present any modeling of the IR excess.

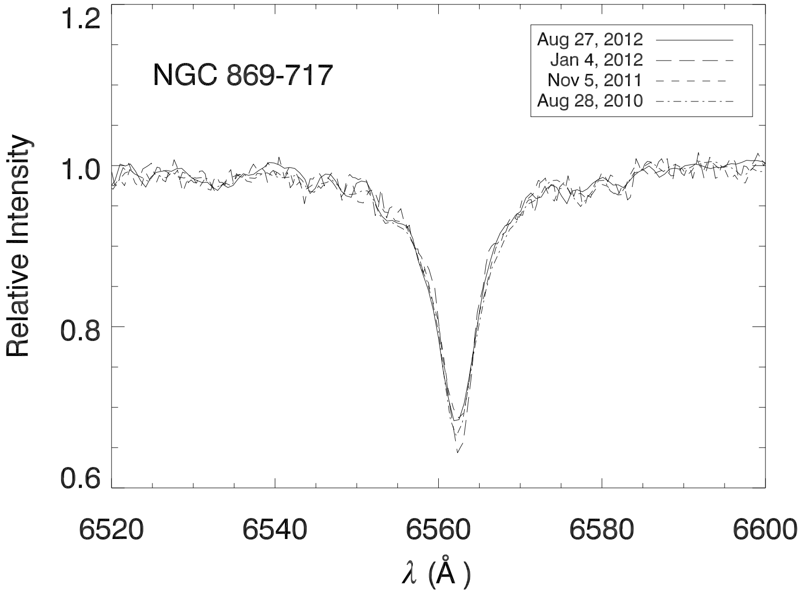

Figure A.11 Hα spectra of NGC 869-717 in same format as Figure A.3.

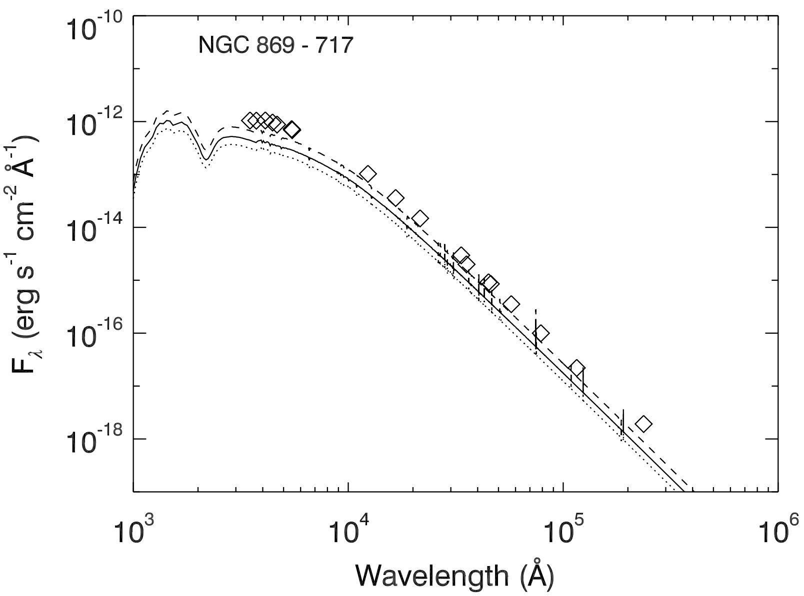

Figure A.12 Observed SED of NGC 869-717 in same format as Figure A.4.

A.1.6 Star 847

Compiled spectroscopic and photometric observations of NGC 869-847. The Hα emission line profile shape of this star suggests that it may be a shell star, with a low inclination to our line of sight. Some variability is observed in the line strength over the course of our observations, particularly in the more or less symmetric shifting of the red-to-violet emission peak ratio, which is suggestive of a more dense spiral structure within the rotating disk. The photometric observations available appear to have been taken during weaker disk phases, making it difficult to model the expected IR excess of this Be star.

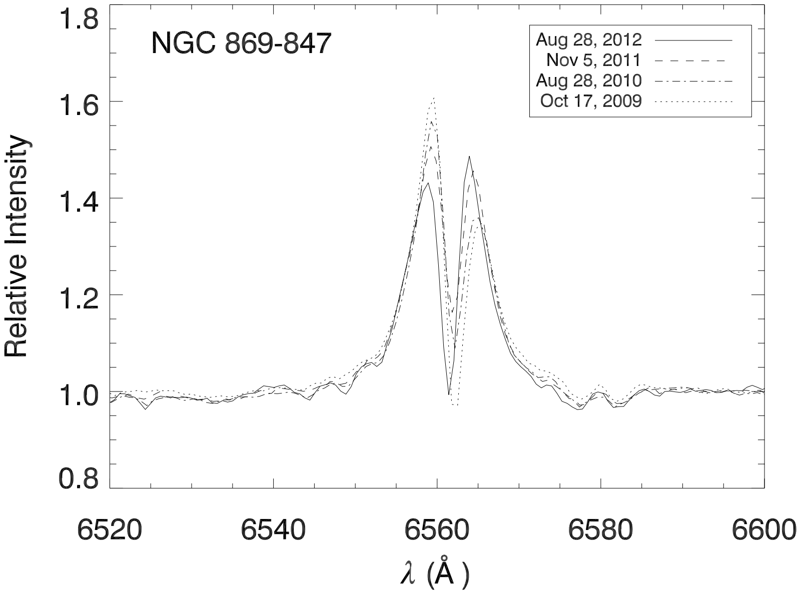

Figure A.13 Hα spectra of NGC 869-847 in same format as Figure A.3.

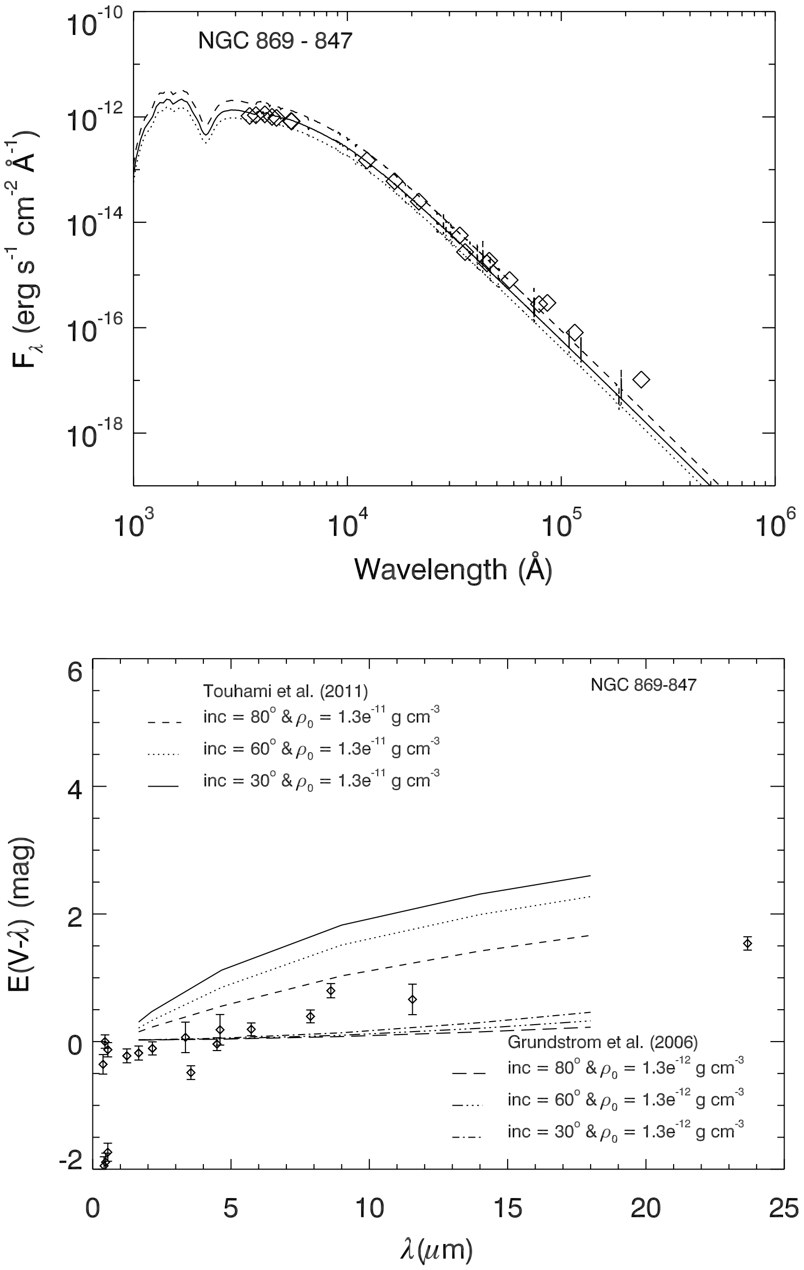

Figure A.14 Observed SED and disk excess of NGC 869-847 in same format as Figure A.4.

A.1.7 Star 992

Compiled spectroscopic and photometric observations of NGC 869-992. Some variation in the strength of Hα emission is observed in this star, however, the emission signature is weak, with a shape suggestive of a very low inclination shell Be star. There appears to be some small amount of observed disk excess for a few of the photometric observations, but most appear to have been taken during weak disk phases, preventing us from successfully modeling the expected IR excess.

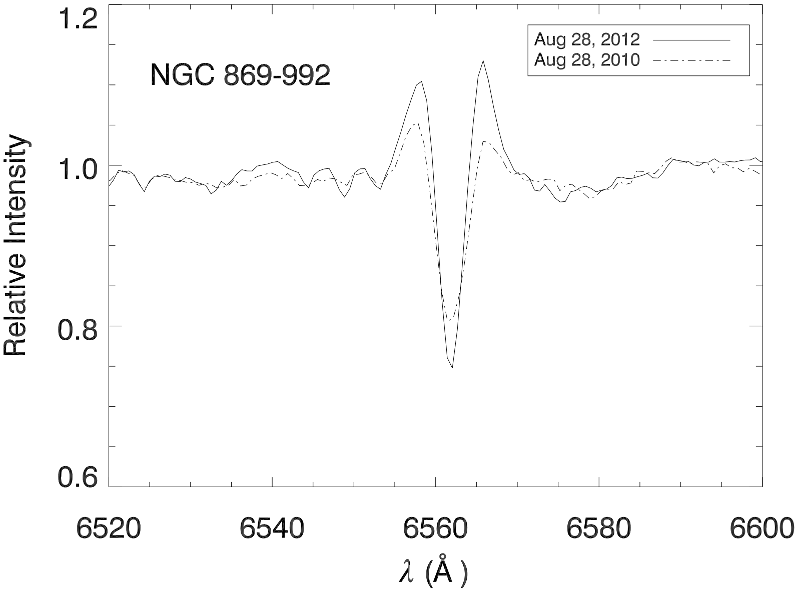

Figure A.15 Hα spectra of NGC 869-992 in same format as Figure A.3.

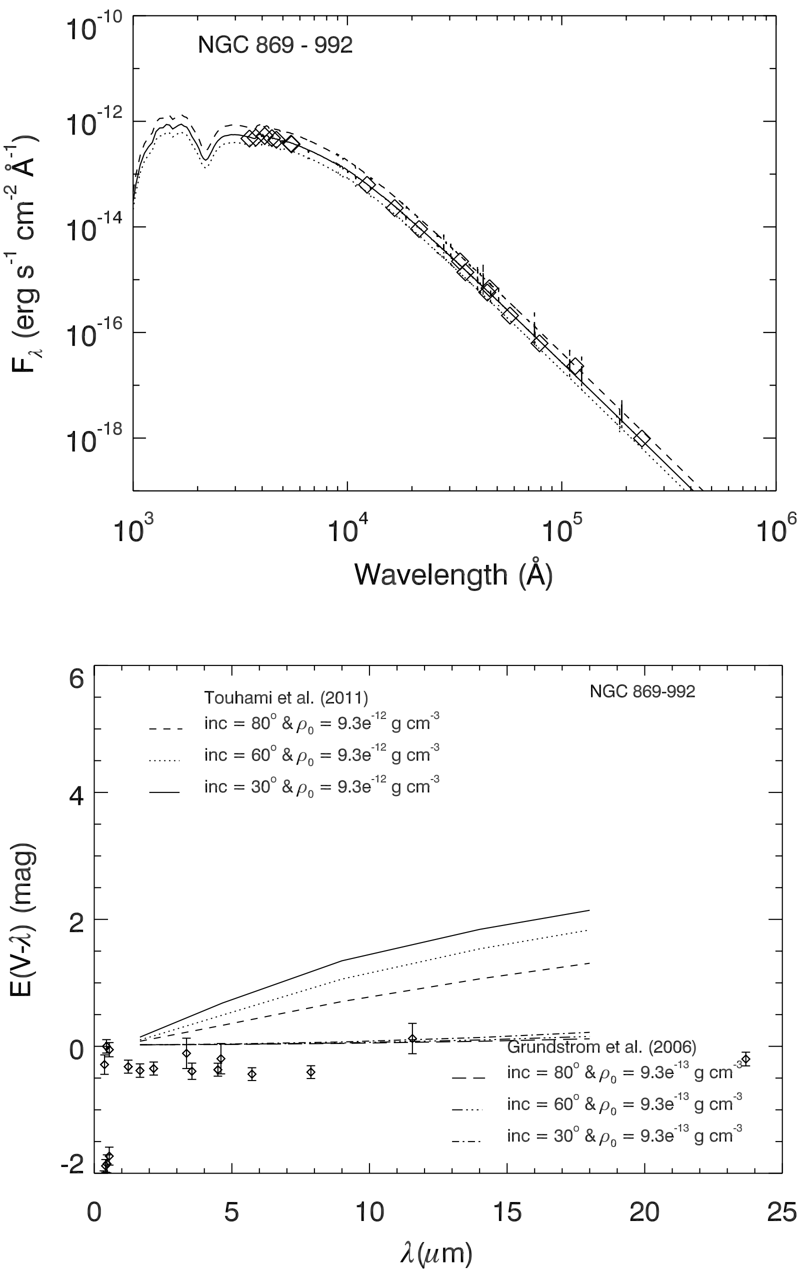

Figure A.16 Observed SED and disk excess of NGC 869-992 in same format as Figure A.4.

A.1.8 Star 1161

Compiled spectroscopic and photometric observations of NGC 869-1161. Smaller variations are observed in the prominent Hα line of this Be star. The clear IR disk excess of this star is well matched by the models of Touhami et al. [2011].

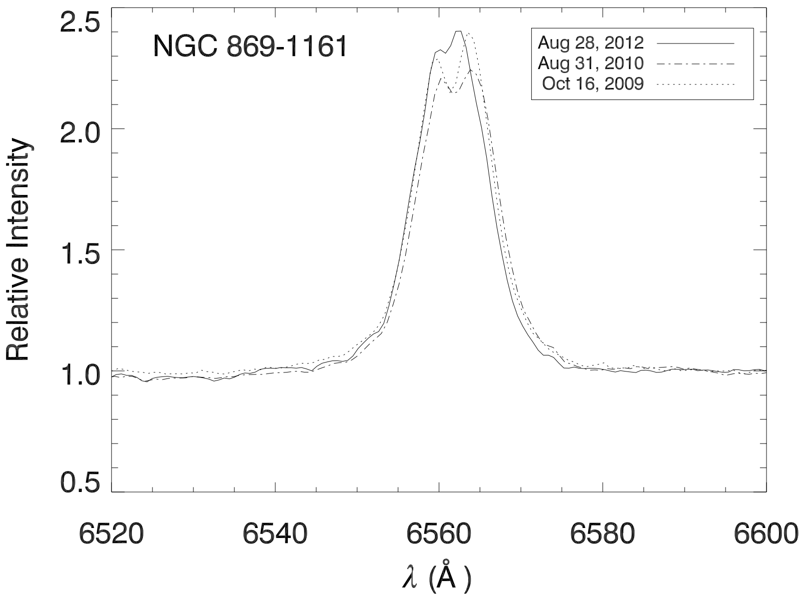

Figure A.17 Hα spectra of NGC 869-1161 in same format as Figure A.3.

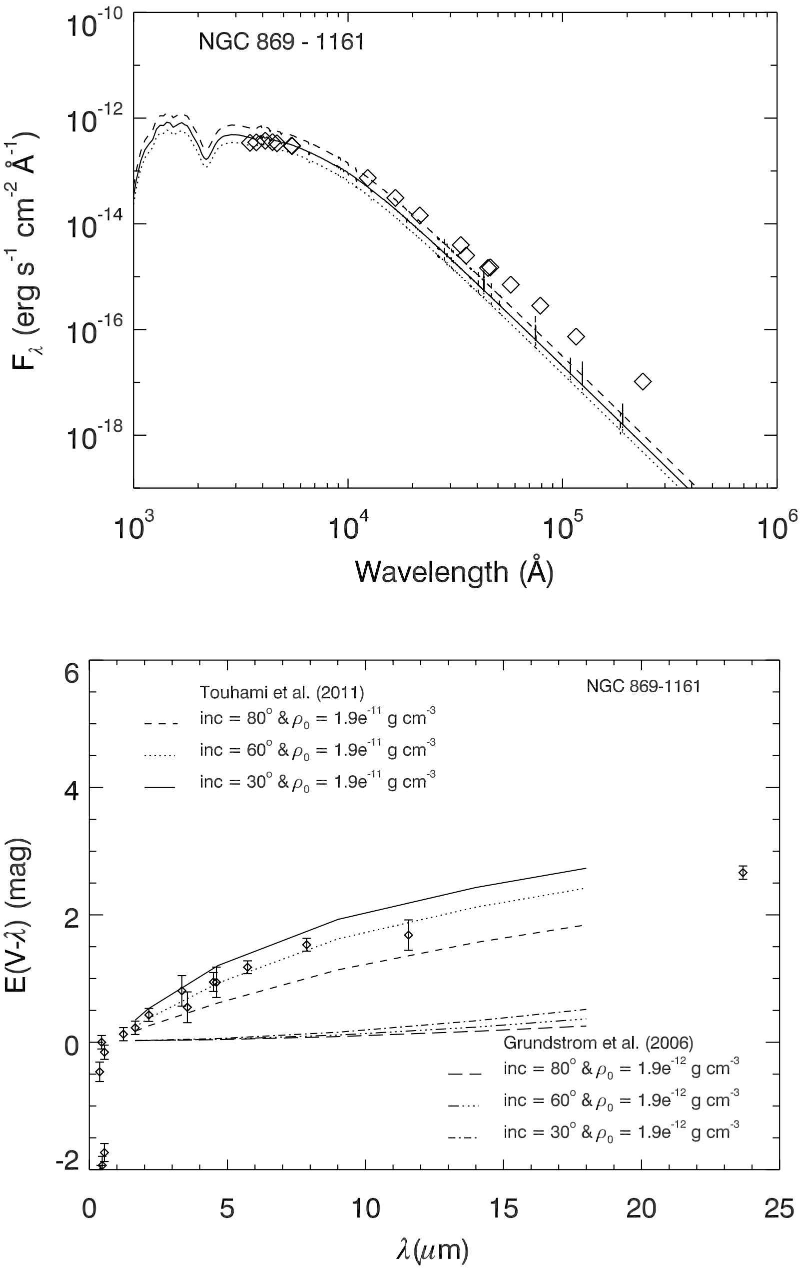

Figure A.18 Observed SED and disk excess of NGC 869-1161 in same format as Figure A.4.

A.1.9 Star 1261

Compiled spectroscopic and photometric observations of NGC 869-1261. The very strong disk present in this Be star shows very small variations over the course of our observations, while a few of the photometric measurements seem to show a little more variation. The observed IR excess of this Be disk is well matched by the models of Touhami et al. [2011], with the exception of the few points suggesting variability.

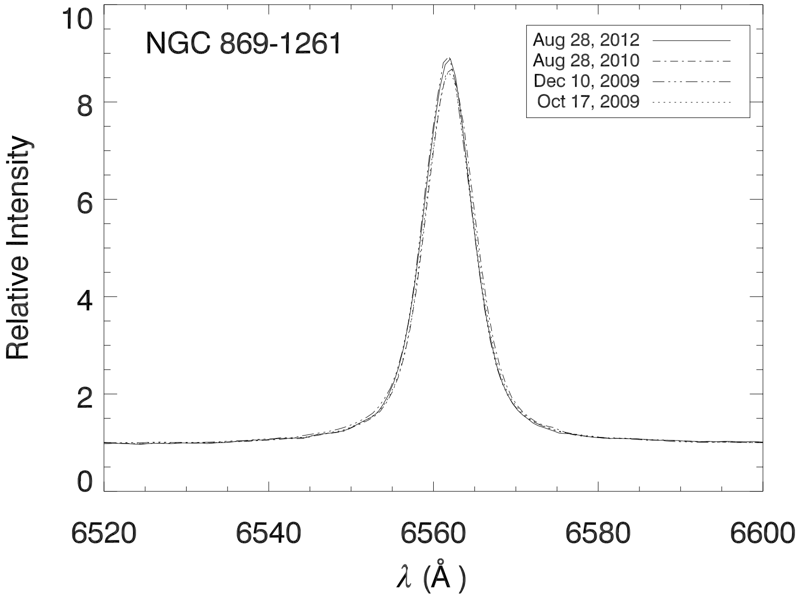

Figure A.19 Hα spectra of NGC 869-1261 in same format as Figure A.3.

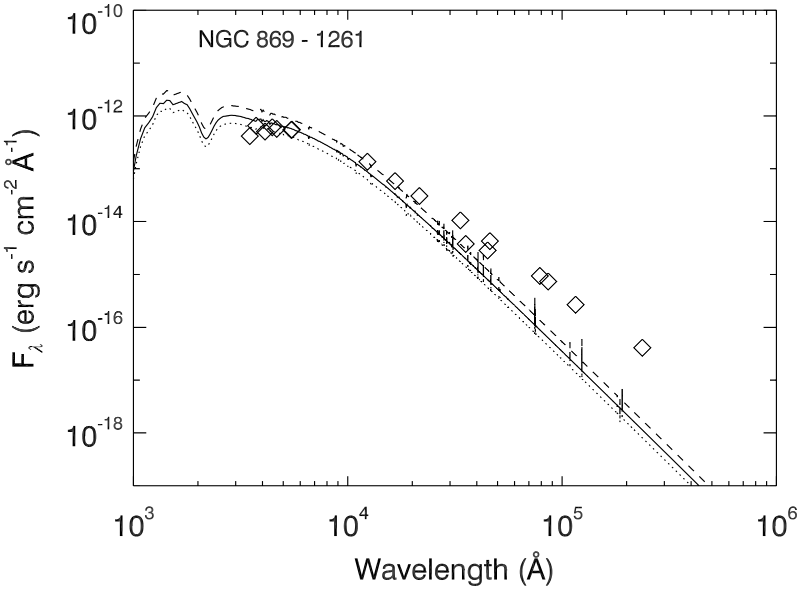

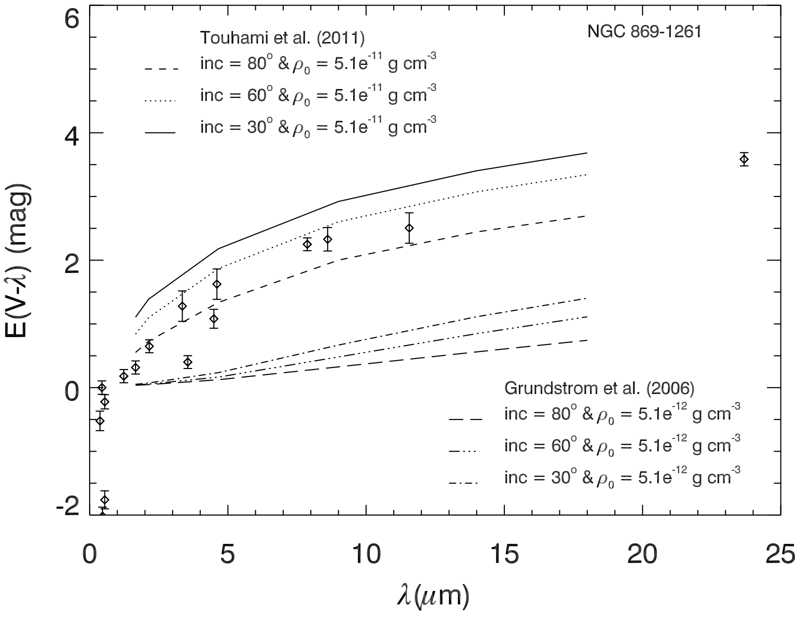

Figure A.20 Observed SED and disk excess of NGC 869-1261 in same format as Figure A.4.

A.1.10 Star 1268

Compiled spectroscopic and photometric observations of NGC 869-1268. This star neither exhibited any emission indicative of a Be disk at the times of our observations, nor does its observed SED show any signs of IR excess. There does appear to be some small changes in the depth of the line core over time, but not enough to suggest the presence or growth of a disk. The observation of emission by Keller et al. [2001], is suggestive of this star possibly being a transient Be star. As there is no observed IR excess for this star, we do not present any modeling of the IR excess.

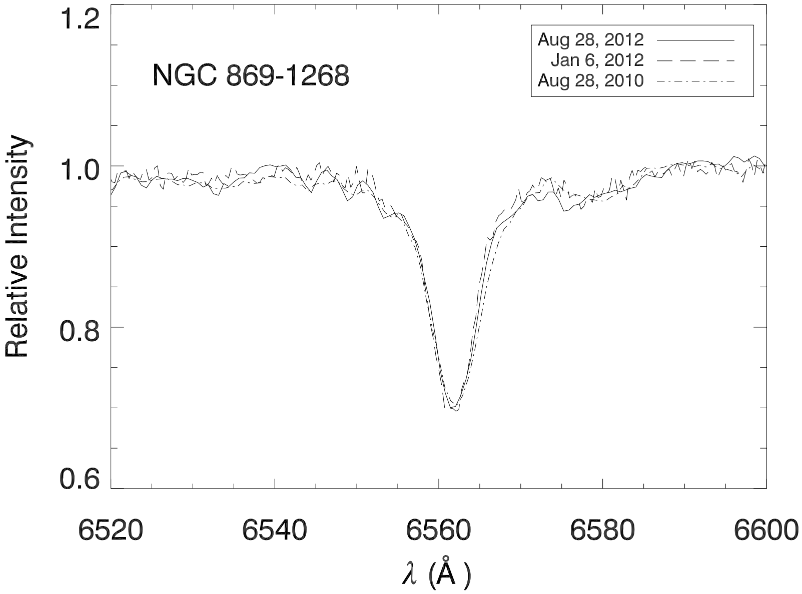

Figure A.21 Hα spectra of NGC 869-1268 in same format as Figure A.3.

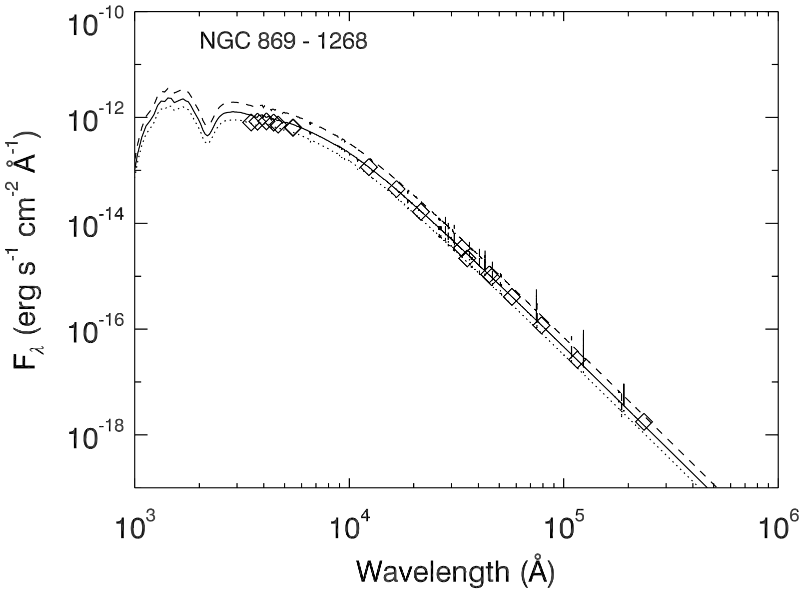

Figure A.22 Observed SED of NGC 869-1268 in same format as Figure A.4.

A.1.11 Star 1278

Compiled spectroscopic and photometric observations of NGC 869-1278. We observe a significant decrease in disk strength in our most recent observation of this star, in comparison to those made in 2009 and 2010. A few of the available photometric observations for this star also seem to show a change in the disk strength.

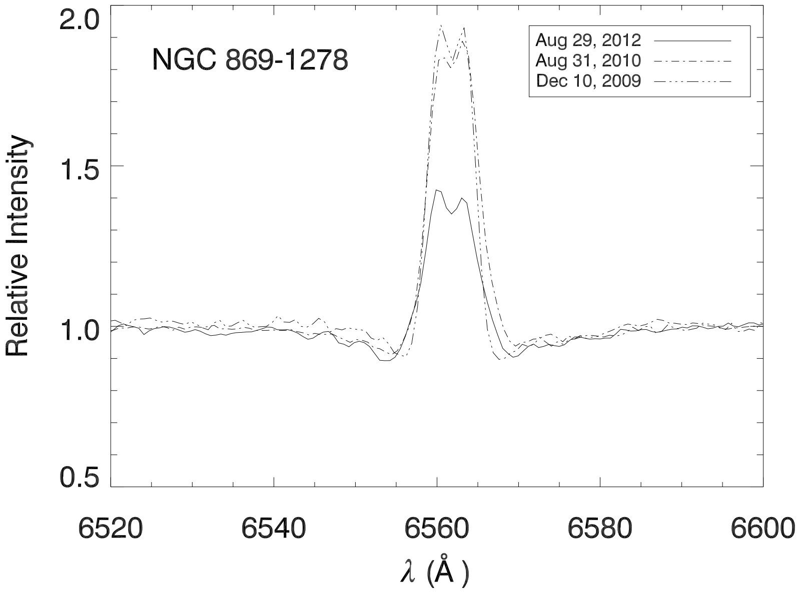

Figure A.23 Hα spectra of NGC 869-1278 in same format as Figure A.3.

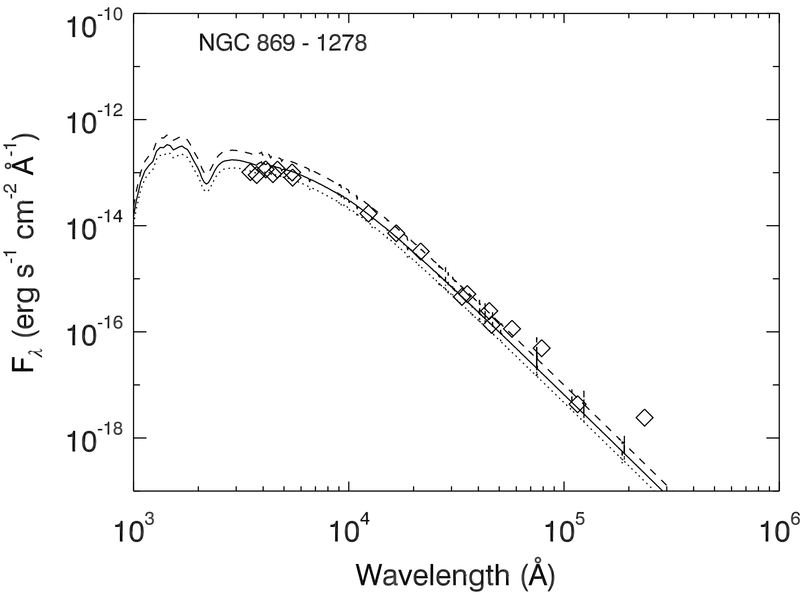

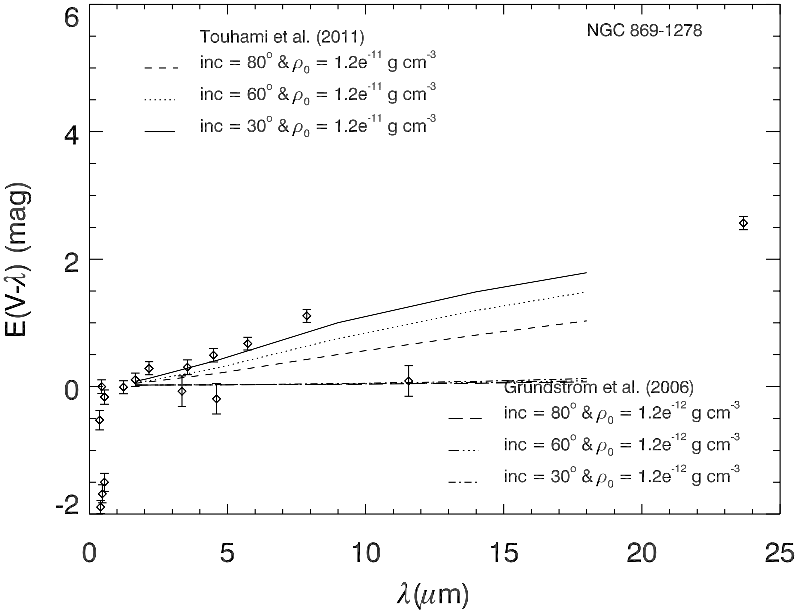

Figure A.24 Observed SED and disk excess of NGC 869-1278 in same format as Figure A.4.

A.1.12 Star 1282

Compiled spectroscopic and photometric observations of NGC 869-1282. Variability in the overall Hα line strength very apparent in the spectra plot, and in a few of the observed photometric magnitudes of this star. The observed IR excess can be matched by the models of Touhami et al. [2011].

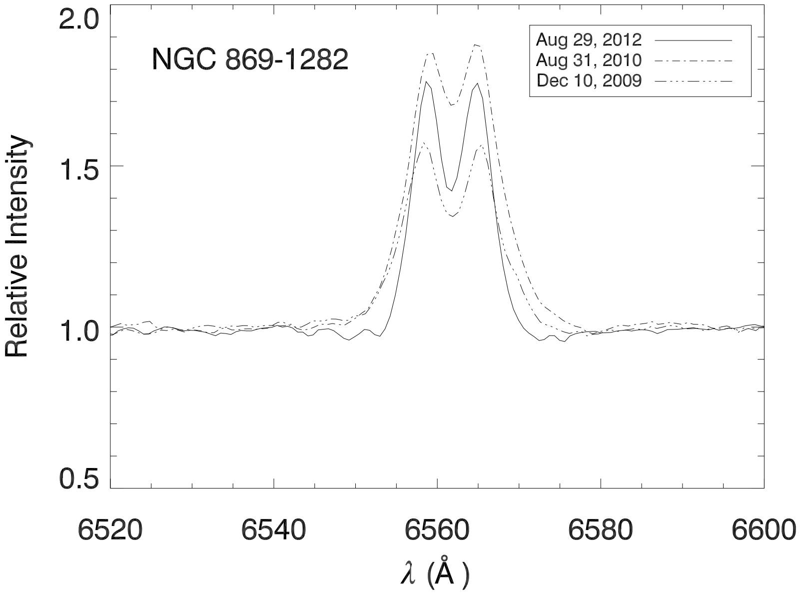

Figure A.25 Hα spectra of NGC 869-1282 in same format as Figure A.3.

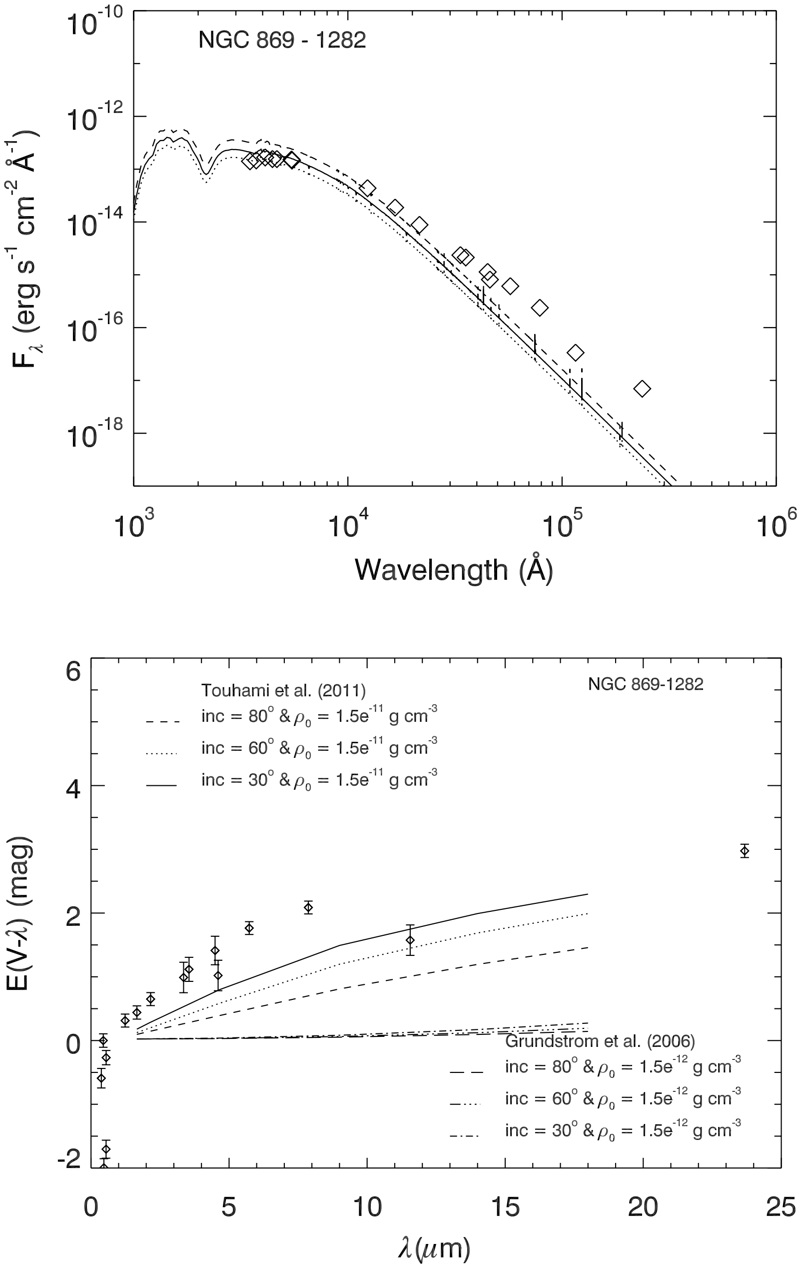

Figure A.26 Observed SED and disk excess of NGC 869-1282 in same format as Figure A.4.

A.2 NGC 884: χ Per

A.2.1 Star 1702

Compiled spectroscopic and photometric observations of NGC 884-1702. From our observations, it is very apparent that this is actually a transient Be star exhibiting a significant amount of variability. However, the available photometric observations appear to have been taken during diskless phases, preventing us from modeling the expected IR excess. Like NGC 869-566, this would make an excellent target for studying disk growth/loss.

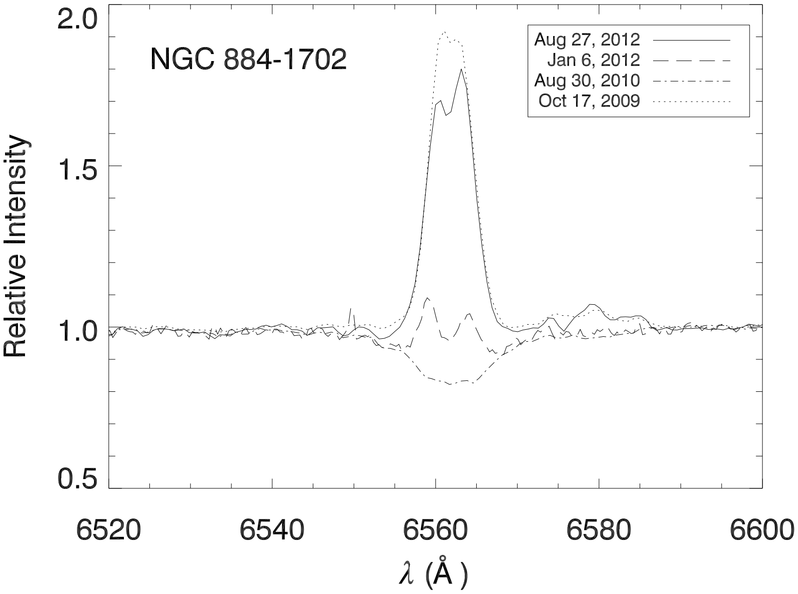

Figure A.27 Hα spectra of NGC 884-1702 in same format as Figure A.3.

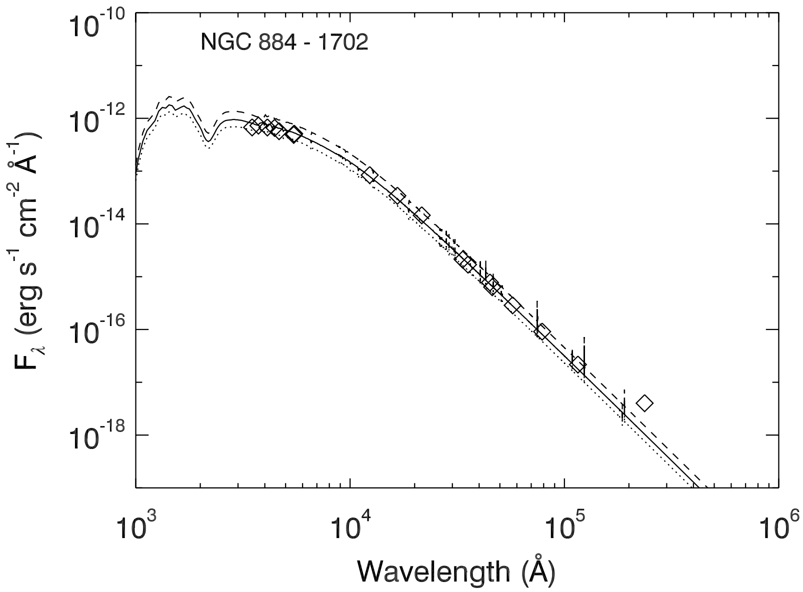

Figure A.28 Observed SED of NGC 884-1702 in same format as Figure A.4.

A.2.2 Star 1926

Compiled spectroscopic and photometric observations of NGC 884-1926. Some variation evident in our observations of Hα and the available photometric measurements. The observed disk excess is well matched by the models of Touhami et al. [2011].

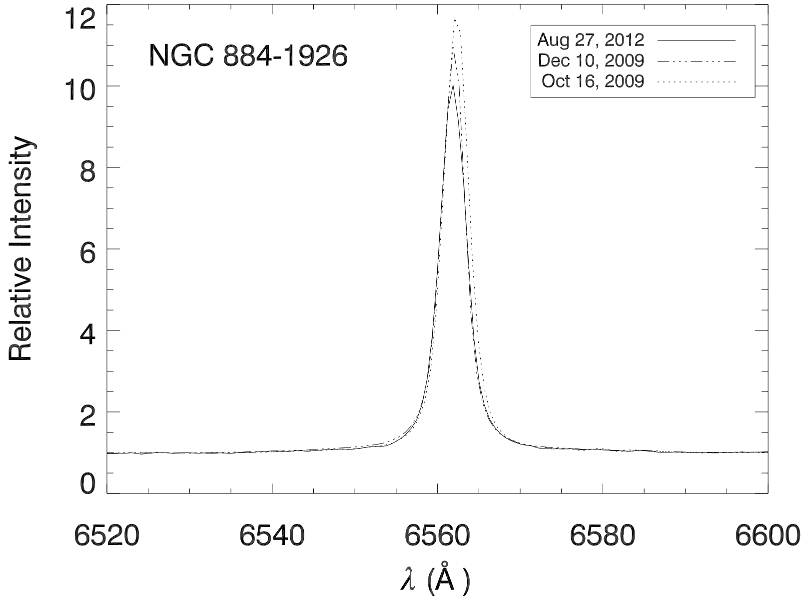

Figure A.29 Hα spectra of NGC 884-1926 in same format as Figure A.3.

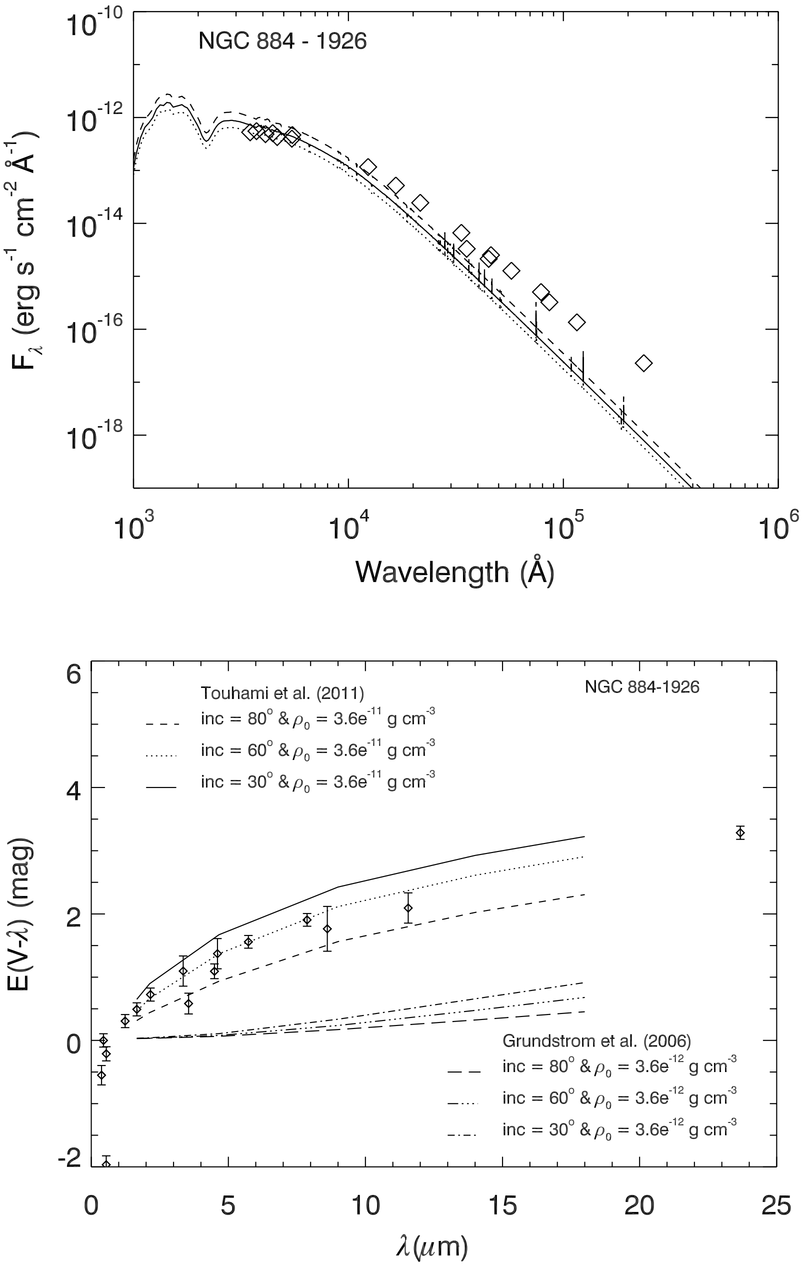

Figure A.30 Observed SED and disk excess of NGC 884-1926 in same format as Figure A.4.

A.2.3 Star 1977

Compiled spectroscopic and photometric observations of NGC 884-1977. With only one observation available for this star in our data, we cannot speak to any variability it may in fact exhibit. The observed SED clearly shows some excess produced by the disk. The observed disk excess can be well matched by the models of Touhami et al. [2011].

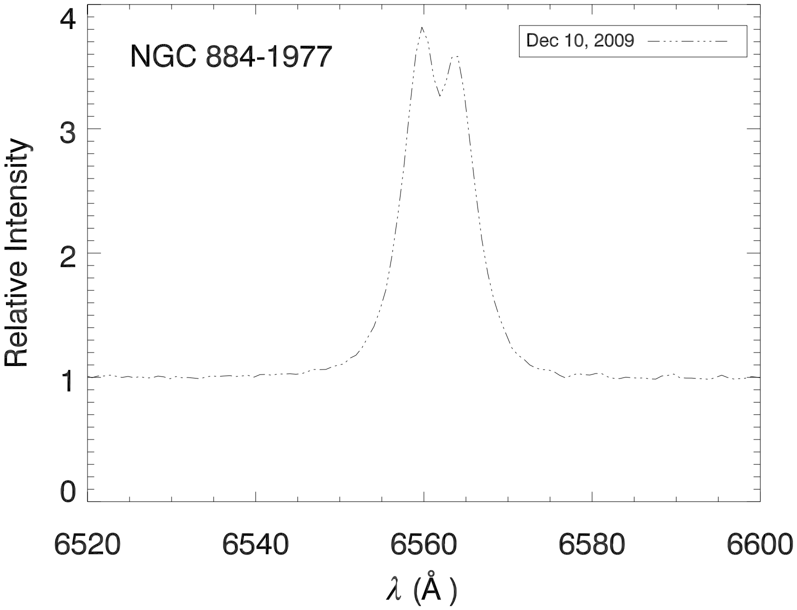

Figure A.31 Hα spectra of NGC 884-1977 in same format as Figure A.3.

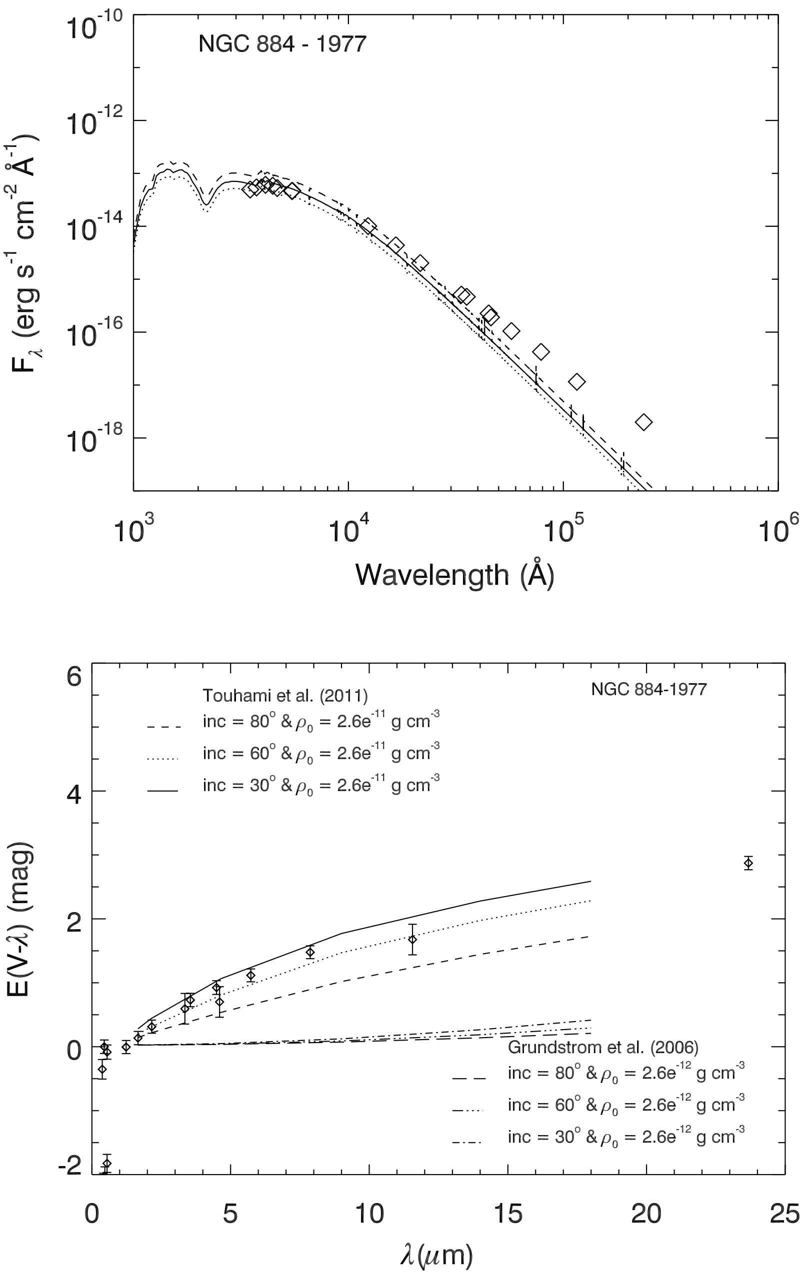

Figure A.32 Observed SED and disk excess of NGC 884-1977 in same format as Figure A.4.

A.2.4 Star 2088

Compiled spectroscopic and photometric observations of NGC 884-2088. This is another Be star showing significant variation in the strength of it's Hα emission, as well as in it's observed SED. It is unclear whether the differences in the observed *uvby* and *UBV* magnitudes are real, however it is very unlikely to be related to the disk structure present as it would contribute a negligible amount of flux at optical wavelengths. With the variations in the observed photometric magnitudes, it is difficult to model the IR excess of this star successfully.

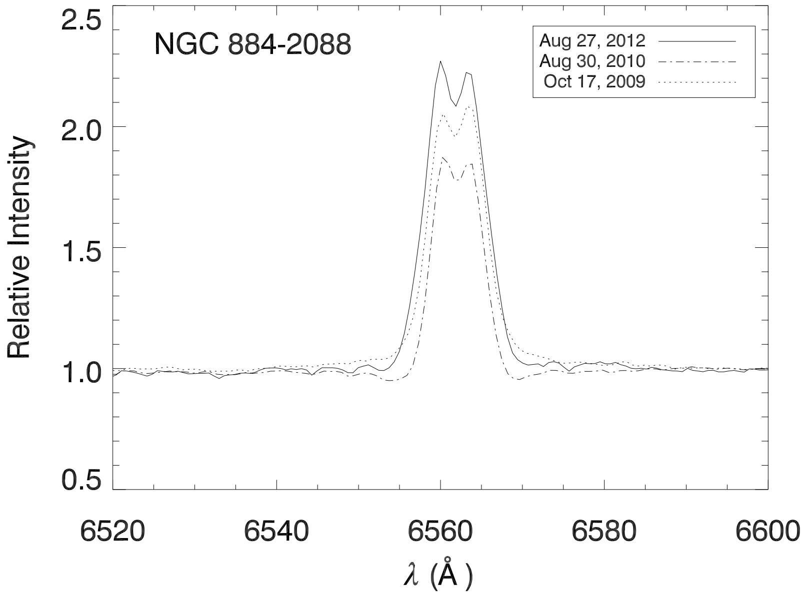

Figure A.33 Hα spectra of NGC 884-2088 in same format as Figure A.3.

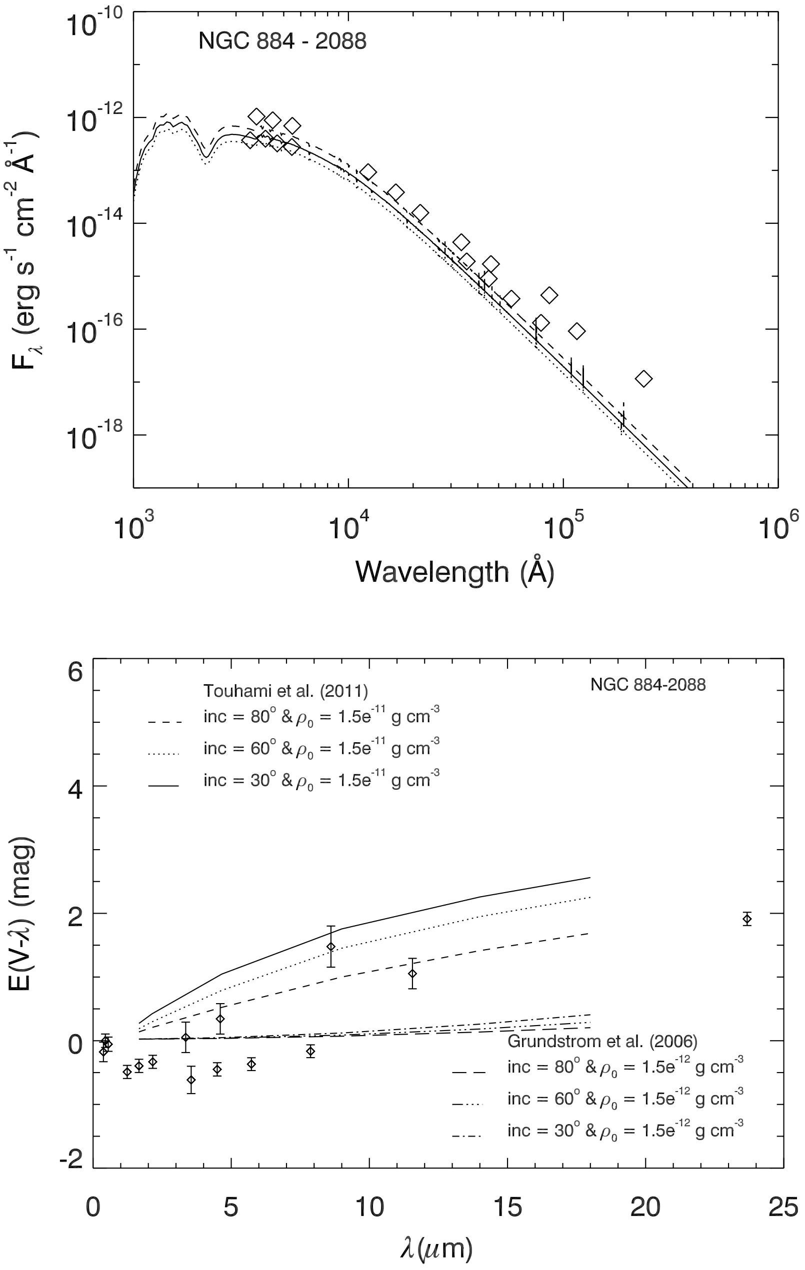

Figure A.34 Observed SED and disk excess of NGC 884-2088 in same format as Figure A.4.

A.2.5 Star 2091

Compiled spectroscopic and photometric observations of NGC 884-2091. The prominent Hα emission line of this star shows little change between the two times of our observation. A clear IR excess is seen in the observed SED, which is matched well by the models of Touhami et al. [2011].

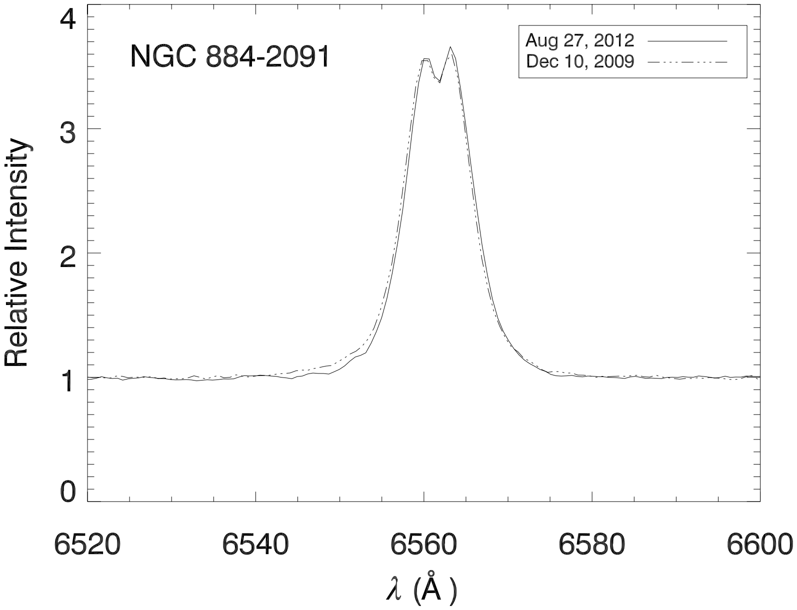

Figure A.35 Hα spectra of NGC 884-2091 in same format as Figure A.3.

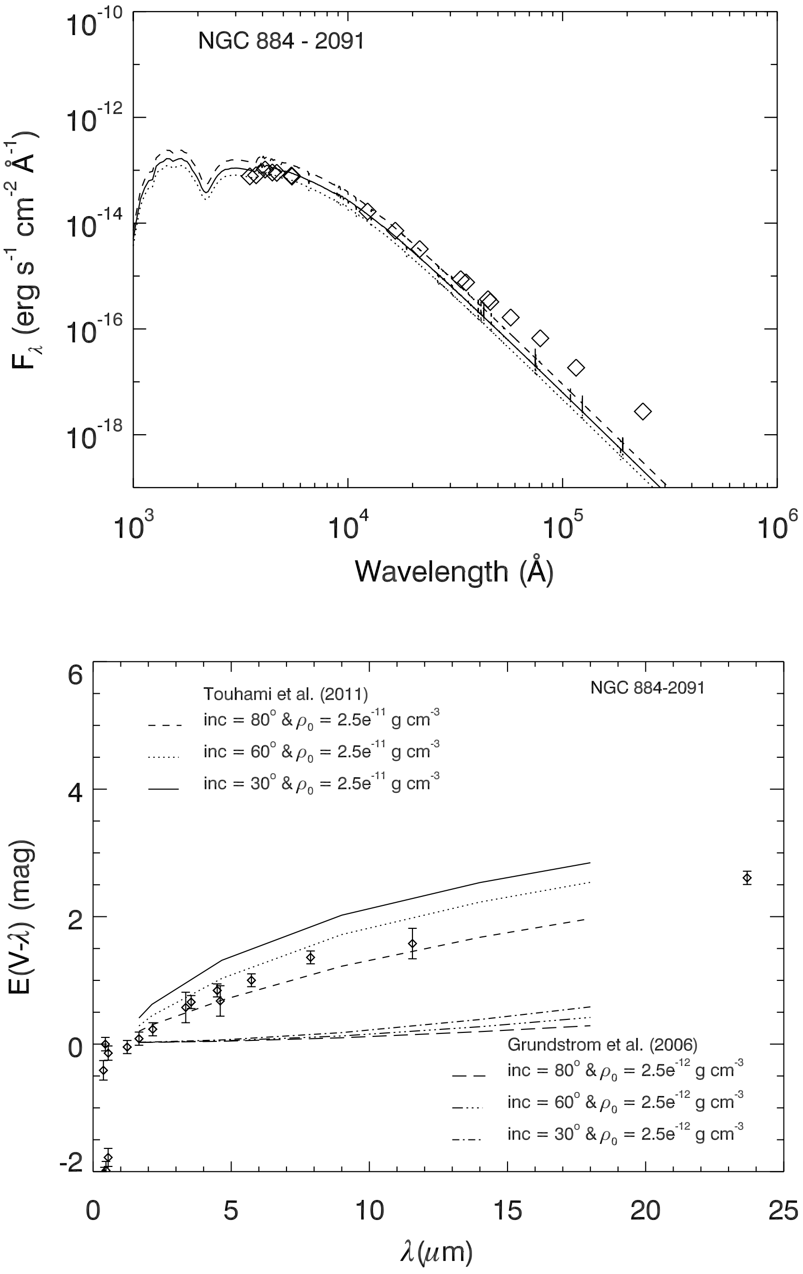

Figure A.36 Observed SED and disk excess of NGC 884-2091 in same format as Figure A.4.

A.2.6 Star 2138

Compiled spectroscopic and photometric observations of NGC 884-2138. Some variation evident in our observations of Hα and the available photometric measurements. The observed disk excess is somewhat difficult to match with the models of Touhami et al. [2011], given the more significant variations in the observed IR excess between different times of measurement.

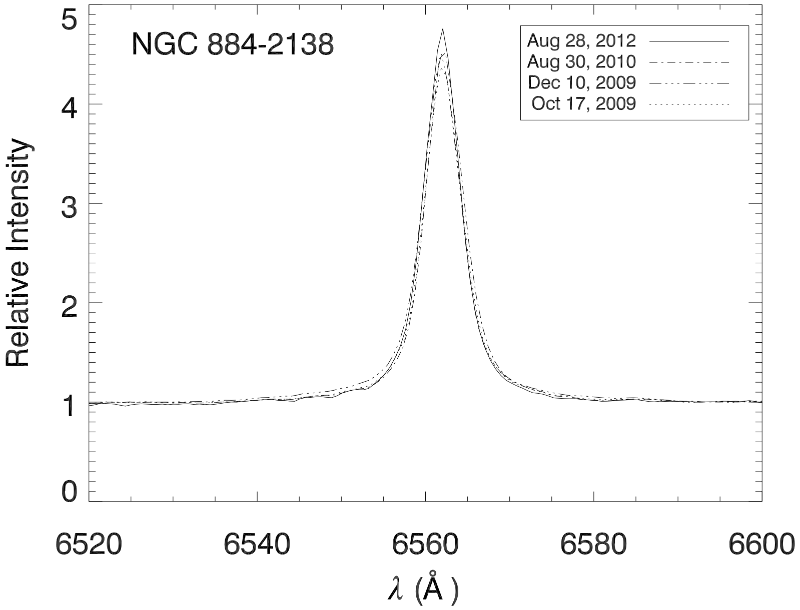

Figure A.37 Hα spectra of NGC 884-2138 in same format as Figure A.3.

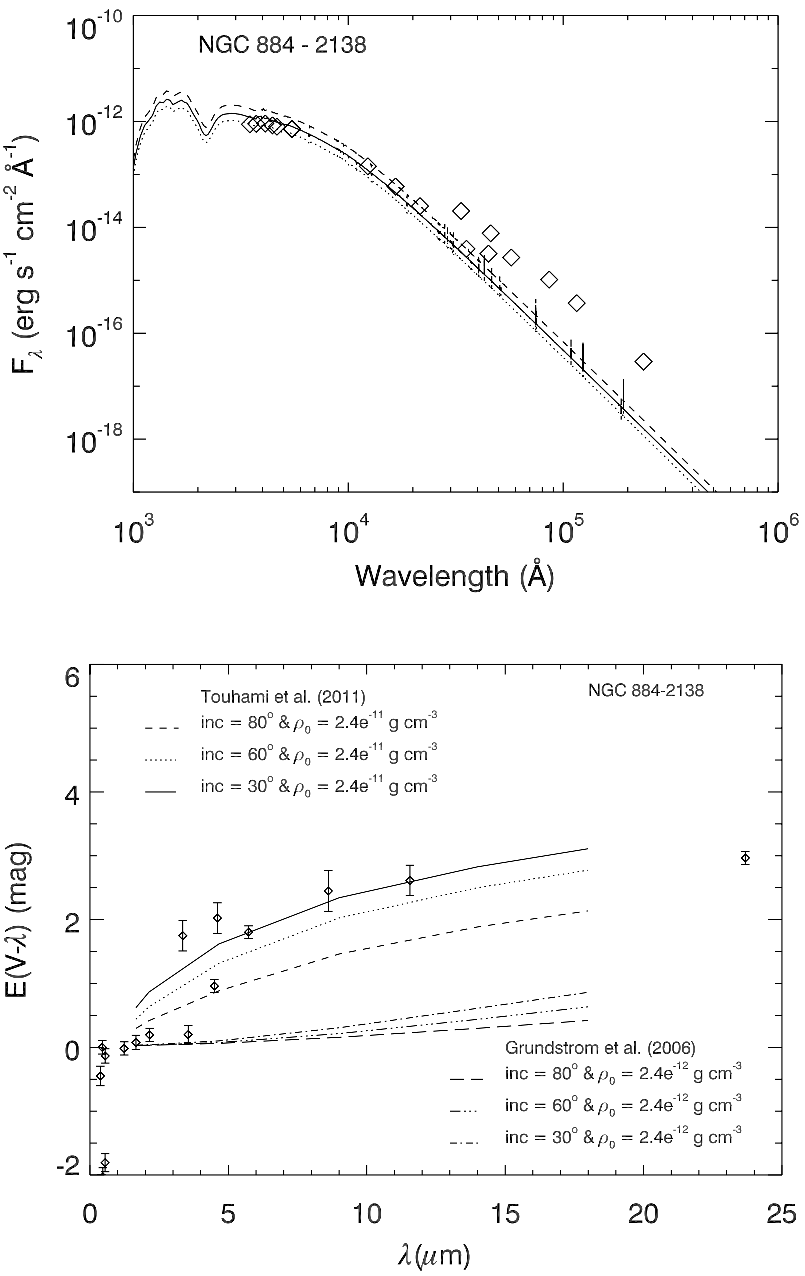

Figure A.38 Observed SED and disk excess of NGC 884-2138 in same format as Figure A.4.

A.2.7 Star 2165

Compiled spectroscopic and photometric observations of NGC 884-2165. Significant variation evident in our observations of Hα, and to a lesser extent in the available photometric measurements. The observed disk excess is well matched by the models of Touhami et al. [2011], with the exception of a few variable points indicative of different phases of disk strength.

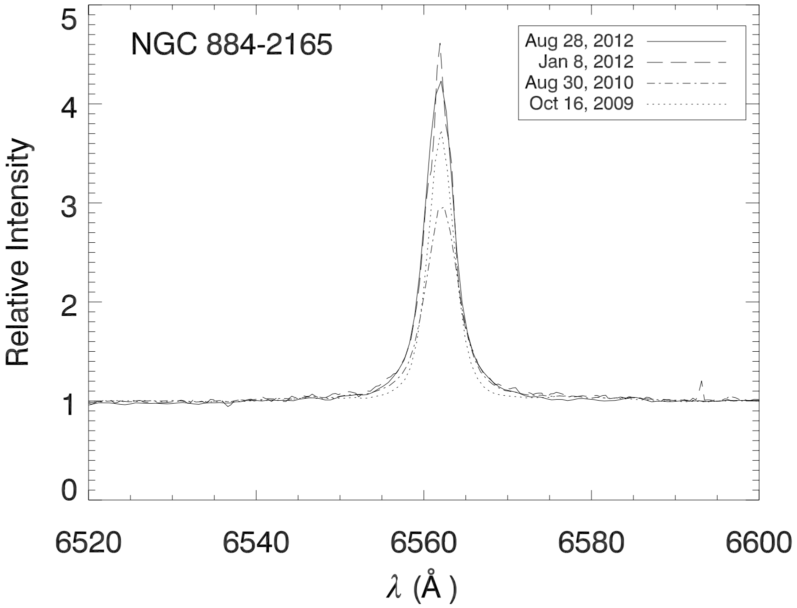

Figure A.39 Hα spectra of NGC 884-2165 in same format as Figure A.3.

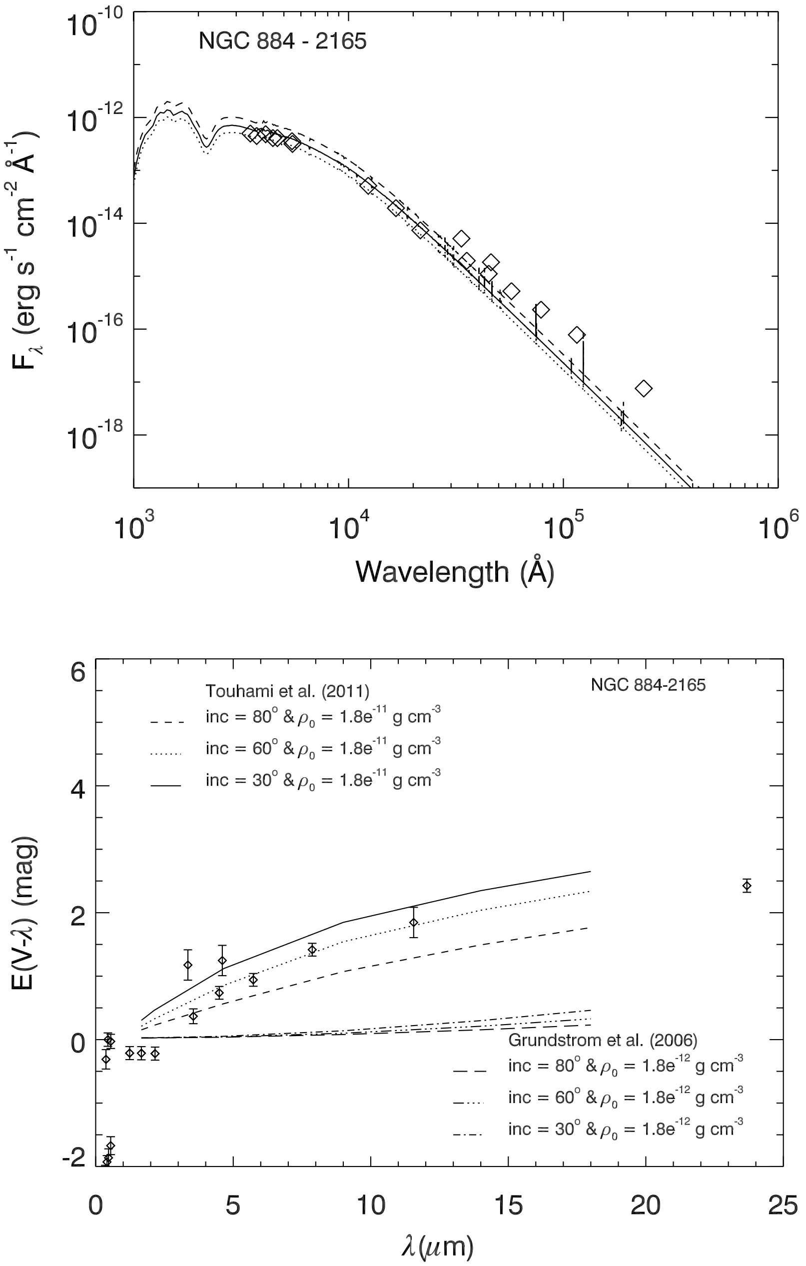

Figure A.40 Observed SED and disk excess of NGC 884-2165 in same format as Figure A.4.

A.2.8 Star 2262

Compiled spectroscopic and photometric observations of NGC 884-2262. This star neither exhibited any emission indicative of a Be disk at the times of our observations, nor does its observed SED show any signs of IR excess. There does appear to be some small changes in the depth of the line core over time, but not enough to suggest the presence or growth of a disk. The observation of emission by Slettebak [1985] and Bragg & Kenyon [2002], is suggestive of this star possibly being a transient Be star. As there is no observed IR excess for this star, we do not present any modeling of the IR excess.

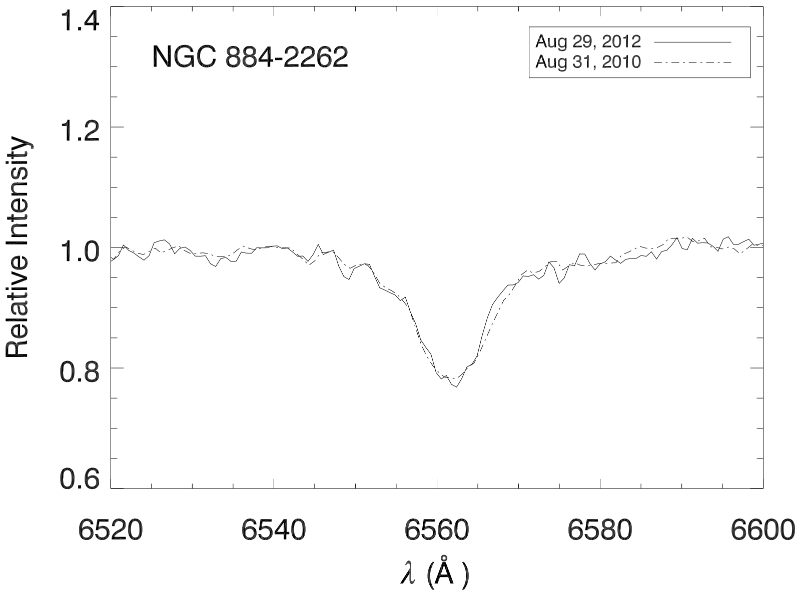

Figure A.41 Hα spectra of NGC 884-2262 in same format as Figure A.3.

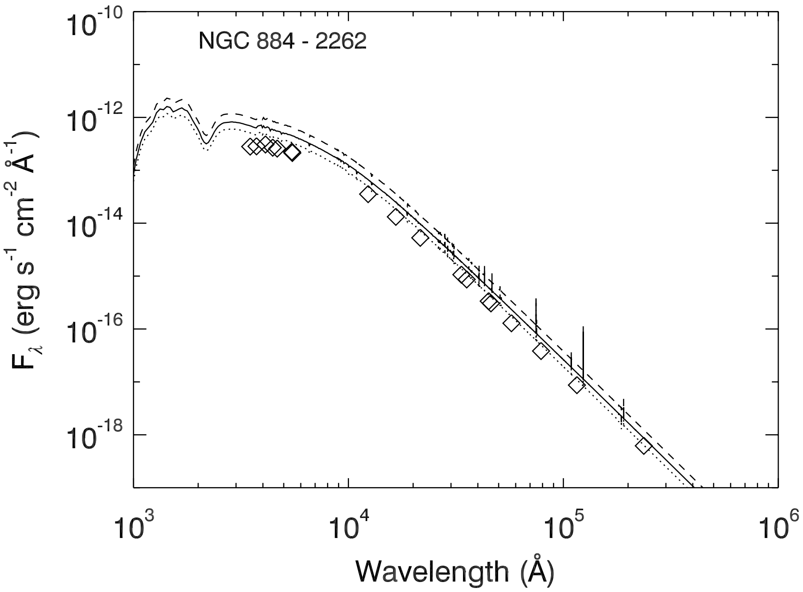

Figure A.42 Observed SED of NGC 884-2262 in same format as Figure A.4.

A.2.9 Star 2284

Compiled spectroscopic and photometric observations of NGC 884-2284. Subtle variation evident in our observations of Hα and in the available photometric measurements. The observed disk excess can be well matched by the models of Touhami et al. [2011], with the exception of a few spurious points caused by variations in the disk strength at different times of observation.

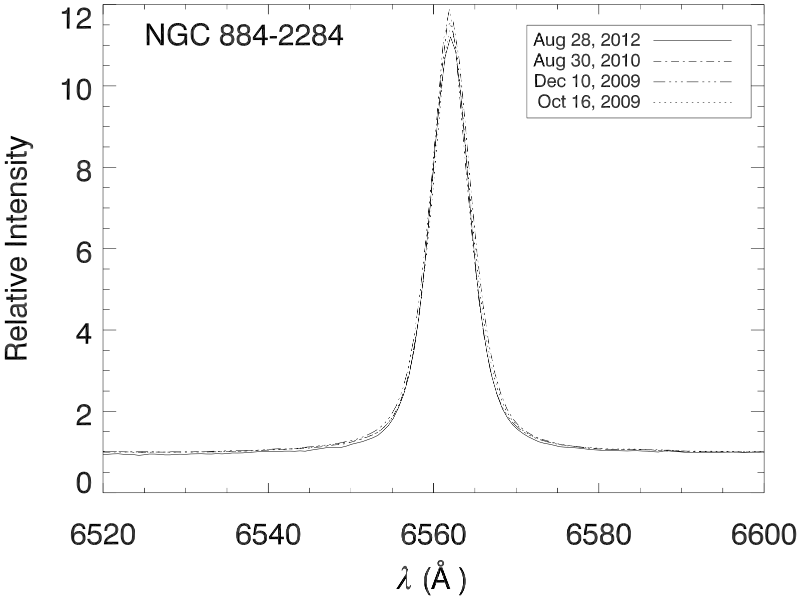

Figure A.43 Hα spectra of NGC 884-2284 in same format as Figure A.3.

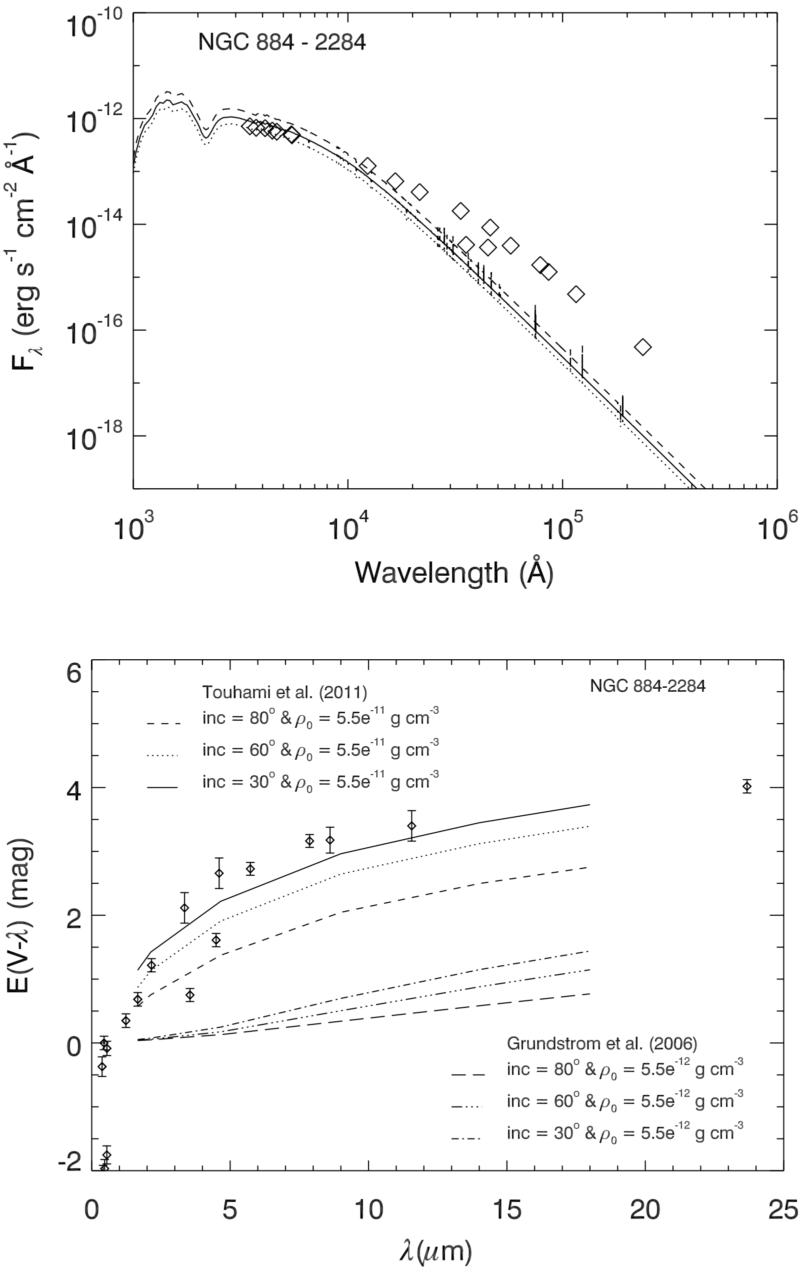

Figure A.44 Observed SED and disk excess of NGC 884-2284 in same format as Figure A.4.

A.2.10 Star 2563

Compiled spectroscopic and photometric observations of NGC 884-2563. With only one observation available for this star in our data, we cannot speak to any variability it may in fact exhibit. The observed SED clearly shows some excess produced by the disk. The observed disk excess can be well matched by the models of Touhami et al. [2011].

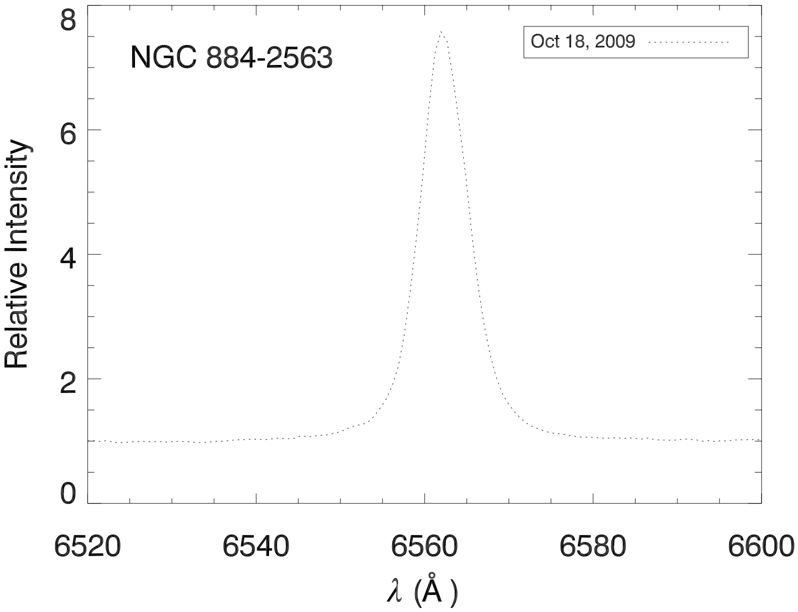

Figure A.45 Hα spectra of NGC 884-2563 in same format as Figure A.3.

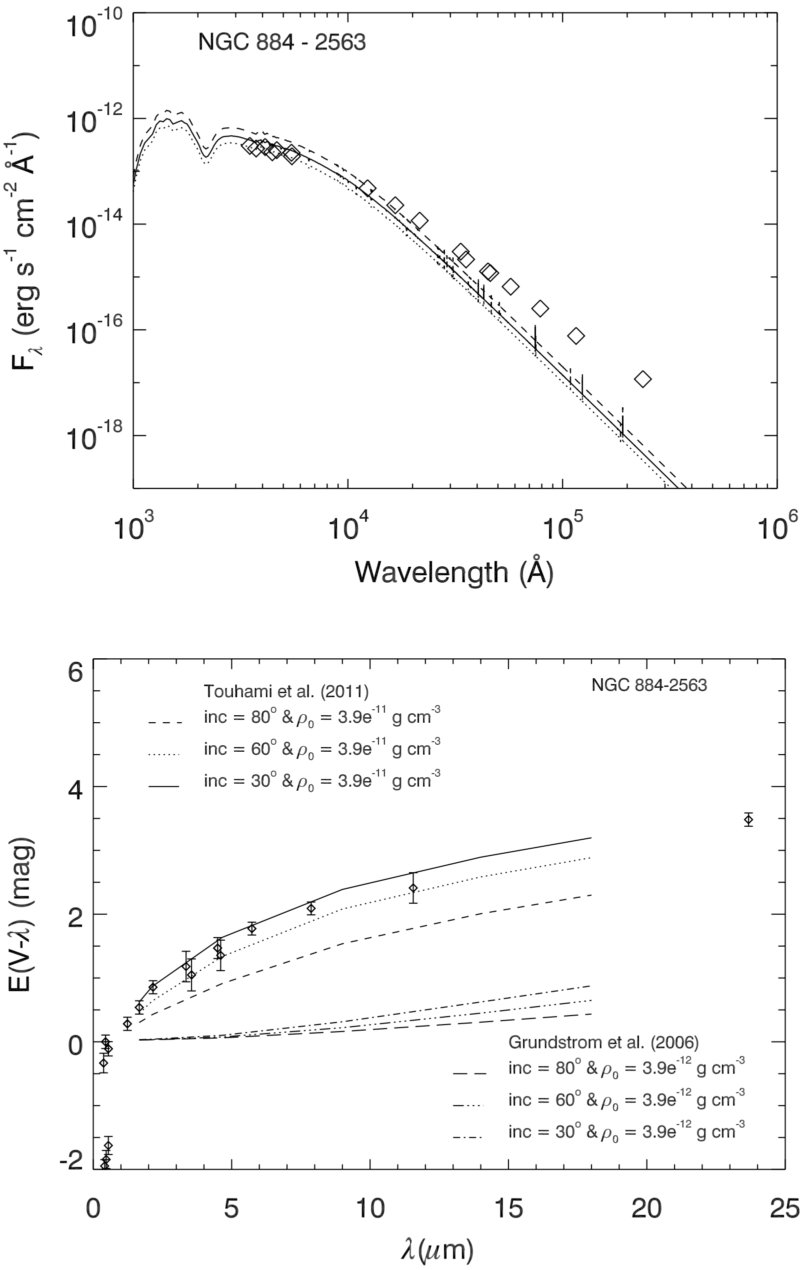

Figure A.46 Observed SED and disk excess of NGC 884-2563 in same format as Figure A.4.

A.2.11 Star 2771

Compiled spectroscopic and photometric observations of NGC 884-2771. With only one observation available for this star in our data, we cannot speak to any variability it may in fact exhibit. The observed SED clearly shows some excess produced by the disk. The observed disk excess can be well matched by the models of Touhami et al. [2011].

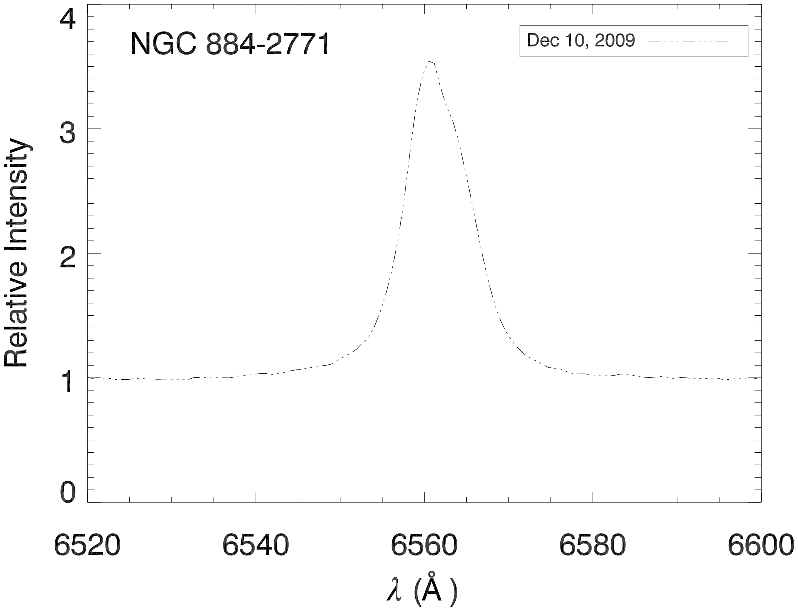

Figure A.47 Hα spectra of NGC 884-2771 in same format as Figure A.3.

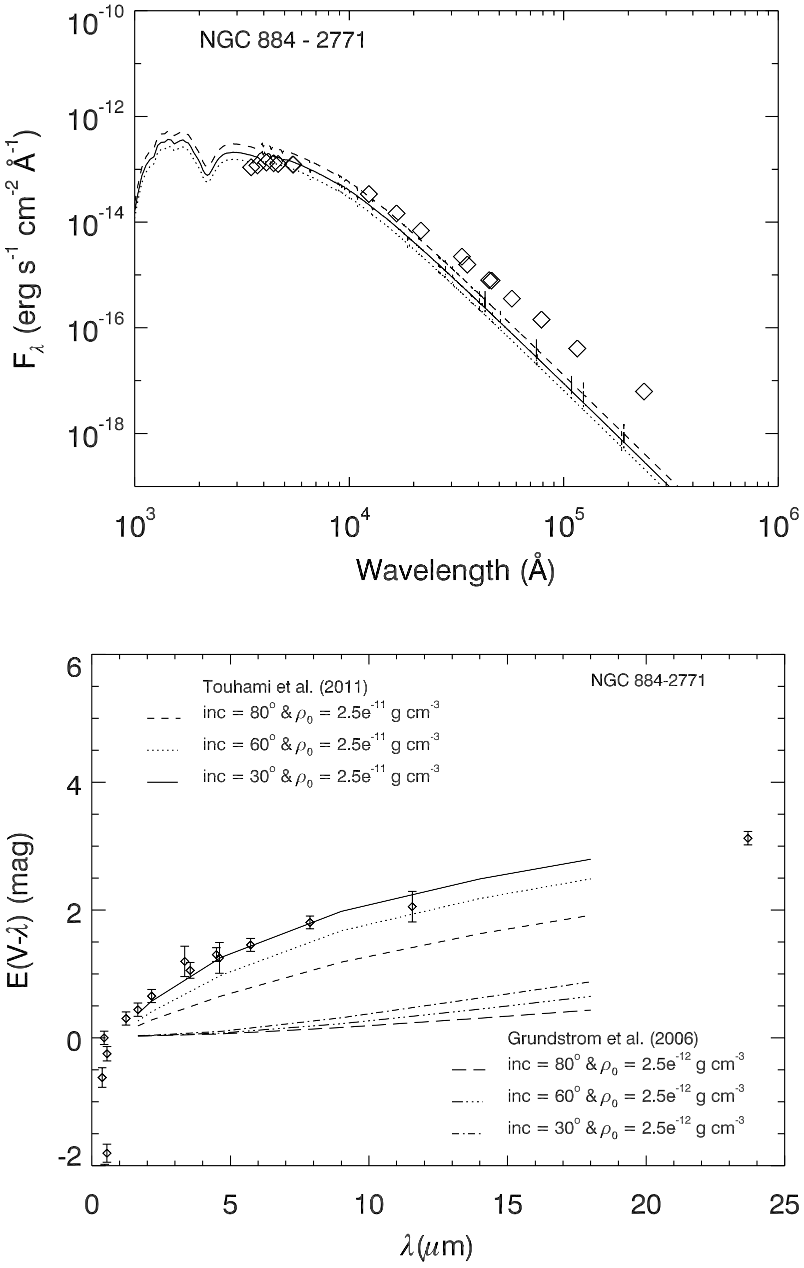

Figure A.48 Observed SED and disk excess of NGC 884-2771 in same format as Figure A.4.

Bibliography

Adams, W. S., & VanMaanen, A. 1913, AJ, 27, 187

Balona, L. A. 1984, MNRAS, 211, 973

Balona, L. A., & Shobbrook, R. R. 1984, MNRAS, 211, 375

Bjorkman, J. E., & Carciofi, A. C. 2005, in Astronomical Society of the Pacific Conference Series, Vol. 337, The Nature and Evolution of Disks Around Hot Stars, ed. R. Ignace & K. G. Gayley, 75

Bragg, A., & Kenyon, S. 2002, AJ, 124, 3289

—. 2005, AJ, 130, 134

Carciofi, A. C., & Bjorkman, J. E. 2006, ApJ, 639, 1081

Carroll, B., & Ostlie, D. 2007, An introduction to modern astrophysics (Pearson Addison-Wesley)

Castelli, F., & Kurucz, R. L. 2004, ArXiv Astrophysics e-prints

Cohen, M., Wheaton, W. A., & Megeath, S. T. 2003, AJ, 126, 1090

Colina, L., Bohlin, R. C., & Castelli, F. 1996, AJ, 112, 307

Conti, P. S., & Leep, E. M. 1974, ApJ, 193, 113

Cranmer, S. R. 2009, ApJ, 701, 396

Currie, T., Kenyon, S., Rieke, G., Balog, Z., & Bromley, B. C. 2007, ApJ, 663, L105

Currie, T., et al. 2008, ApJ, 672, 558

—. 2010, ApJS, 186, 191

Dachs, J., Kiehling, R., & Engels, D. 1988, A&A, 194, 167

Ekström, S., et al. 2012, A&A, 537, 146

Emilio, M., et al. 2010, A&A, 522, 43

Fabregat, J., Torrejón, J. M., & Bernabeu, G. 1994, Be Star Newsl, 29, 8

Fitzpatrick, E. L. 1999, PASP, 111, 63

Gies, D. R., et al. 2007, ApJ, 654, 527

Grundstrom, E. D., & Gies, D. R. 2006, ApJ, 651, L53

Grundstrom, E. D., McSwain, M. V., Aragona, C., Boyajian, T. S., Marsh, A. N., & Roettenbacher, R. M. 2011, BSRSL, 80, 371

Hertzsprung, E. 1922, BAN, 1, 151

Horne, K., & Marsh, T. R. 1986, MNRAS, 218, 761

Huang, W., & Gies, D. R. 2006a, ApJ, 648, 591

—. 2006b, ApJ, 648, 580

Huang, W., Gies, D. R., & McSwain, M. V. 2010, ApJ, 722, 605

Hummel, W., & Vrancken, M. 2000, A&A, 359, 1075

Ishihara, D., et al. 2010, A&A, 514, A1

Keller, S. C., Grebel, E. K., Miller, G. J., & Yoss, K. M. 2001, AJ, 122, 248

Krzesiński, J., & Pigulski, A. 1997, A&A, 325, 987

Krzesiński, J., Pigulski, A., & Kołaczkowski, Z. 1999, A&A, 345, 505

Kurucz, R. 1994, Solar abundance model atmospheres for 0,1,2,4,8 km/s. Kurucz CD-ROM No. 19. Cambridge, Mass.: Smithsonian Astrophysical Observatory, 1994., 19

Lanz, T., & Hubeny, I. 2007, ApJS, 169, 83

Marsh Boyer, A. N., McSwain, M. V., Aragona, C., & Ou-Yang, B. 2012, AJ, 144, 158

McSwain, M. V., Huang, W., & Gies, D. R. 2009, ApJ, 700, 1216

McSwain, M. V., Huang, W., Gies, D. R., Grundstrom, E. D., & Townsend, R. H. D. 2008, ApJ, 672, 590

Messow, B. 1913, AAHam, 2b, 1M

Meynet, G., & Maeder, A. 2000, A&A, 361, 101

Napiwotzki, R., Schoenberner, D., & Wenske, V. 1993, A&A, 268, 653

Porter, J. M., & Rivinius, T. 2003, PASP, 115, 1153

Przybilla, N., & Butler, K. 2004, ApJ, 609, 1181

Przybilla, N., Nieva, M., & Butler, K. 2011, JPhCS, 328, 012015

Reach, W. T., et al. 2005, PASP, 117, 978

Rieke, G. H., et al. 2008, AJ, 135, 2245

Rivinius, T., Baade, D., & Štefl, S. 2003, A&A, 411, 229

Rivinius, T., et al. 1998, A&A, 333, 125

—. 2001, A&A, 369, 1058

Saesen, S., et al. 2010, A&A, 515, A16

Schaller, G., Schraerer, D., Meynet, G., & Maeder, A. 1992, A&AS, 96, 269

Schild, R. E. 1966, ApJ, 146, 142

Sigut, T. A. A., McGill, M. A., & Jones, C. E. 2009, ApJ, 699, 1973

Skrutskie, M. F., et al. 2006, AJ, 131, 1163

Slesnick, C., Hillenbrand, L. A., & Massey, P. 2002, ApJ, 576, 880

Slettebak, A. 1968, ApJ, 154, 933

—. 1985, ApJ, 59, 769

Southworth, J., Zucker, S., Maxted, P. F. L., & Smalley, B. 2004, MNRAS, 355, 986

Strom, S. E., Wolff, S. C., & Dror, D. H. A. 2005, AJ, 129, 809

Touhami, Y., Gies, D. R., & Schaefer, G. H. 2011, ApJ, 729, 17

Trumpler, R. J. 1926, PASP, 38, 350

Wright, E. L., et al. 2010, AJ, 140, 1868

Curriculum Vitae

EDUCATION

Lehigh University, Bethlehem, Pennsylvania USA

Ph.D., Physics — September 2013
Adviser: M. Virginia McSwain, Ph.D.
Thesis: *Characterization of the B and Be Star Populations of NGC 869 and NGC 884*

M.S., Physics — January 2010

Christopher Newport University, Newport News, Virginia USA

B.S., Applied Physics (Leadership minor), *Cum Laude, Honors* — May 2008

SKILLS & EXPERTISE

- *Astronomy*: Optical observation and instrumentation · Spectroscopy · Photometry · Data acquisition and quality control · Signal processing and analysis · Databases · Troubleshooting · Scripting
- *Software*: IRAF · Mathematica · Word · PowerPoint · Excel · $\LaTeX\,2_\varepsilon$
- *Programming and platforms*: IDL · Python · Java · Root · Windows · Macintosh · Unix

TEACHING EXPERIENCE

Lehigh University, Bethlehem, Pennsylvania USA

Apprentice Teacher — **Spring 2012**

- Co-taught ASTR 07 with Prof. M. Virginia McSwain. The class consisted of approximately 60 students, predominantly non-science majors.
- Taught 4 supervised and 6 unsupervised lectures.
- Assisted in writing homework and exams, grading, and tutoring students.

Lehigh University's Teacher Development Program — **Fall 2011, Spring 2012**

- Weekly seminars on teaching in a higher education environment. Topics included: differences between effective and ineffective presentation techniques and communication skills, incorporation of technology into lectures, academic support services available to students, and how to engage and inspire students to promote concept mastery and higher-order thinking.

Substitue Lecturer — **November 15, 2010**

- ASTR-301 Modern Astrophysics I. Prepared and delivered a lecture reviewing the physical properties of massive stars and stellar clusters. Particular emphasis was placed on Be stars as laboratories for study of massive star and angular momentum evolution.

Graduate Teaching Assistant — **Fall, Spring 2009**

- ASTR-08 Introductory Astronomy Lab (single semester course for science and non-science students). Lab material covered a basic introduction to planetary, stellar, galactic, and extragalactic astronomy. Two lab sections were taught, each consisting of about 20 students, meeting for three hours per week and two night observation sessions of the Moon and Jupiter.
- PHY-22 Introductory Physics Laboratory II (second semester physics for science and engineering students). Labs covering material on circuits, optics, and a basic introduction to electrostatics and magnetostatics. Two lab sections where taught, each consisting of about 20 students, meeting for three hours per week.

RESEARCH EXPERIENCE

Lehigh University, Bethlehem, Pennsylvania USA

Graduate Research Assistant — **Summer 2008 – Summer 2013**

- Thesis Work: Investigating the B and Be star populations of the well known double cluster h and χ Persei (NGC 869 and NGC 884). The primary project goals include measuring physical parameters for 104 B and Be stars, initial characterization of the Be star disk temperatures and radii, and in-depth modeling of the Be star disk structures.
- Experience observing a total of 70 nights on 4 different instruments.
- 3 successful proposals (2 as PI) for observations using the KPNO 2.1m and WIRO 2.3m telescopes.

Research Experience for Undergraduates (REU) Student **Summer 2006**

- Determined orbital period and physical parameters of optical star in the Algol binaries U Cephei and RS Vulpecula from available archived *IUE* and *FUSE* data.

Thomas Jefferson National Accelerator Facility, Newport News, Virginia USA
Undergraduate Research Assistant **February 2007 – May 2008**

- Worked closely with the GEp-III, GEp-2γ, and SANE collaborations in conducting measurements of the elastic and magnetic form factors of the proton at large momentum transfer, Q^2.
- Assisted in assembling, testing, and running experimental packages.
- Worked 25 shifts during experiment runtime as Shift Leader.

Honors and Awards

GRC Meeting: Astronomy's Discoveries and Physics Education - travel support	June 2012
AAS Travel Grant to 27th IAU General Assembly Meeting	August 2009
Selected participant Lehigh University Academic Symposium	April 2009
William T. Patrick, Jr. Scholars in Science Endowment Scholarship	2007 – 2008
Northrop Grumman Newport News Scholarship	2004 – 2007

Accepted Grant Proposals

Sigma Xi Grants in Aid of Research Spring 2011 $3000.00
PI: **Marsh, A. N.** *A Study of the B and Be Star Populations of h & χ Persei*

Accepted Observing Proposals

Physical Properties and Variability of Be Star Disks, WIRO Aug–Oct semester 2012
PI: **Boyer, A. N. M.**
CoIs: McSwain, M. V., Aragona, C., & Touhami, Y.

A Study of Balmer Emission in Be Stars, KPNO 2.1m Semester B 2011
PI: Aragona, C.
CoIs: **Marsh, A.**, McSwain, M. V.

Stellar Properties and Variable Emission of Be Stars, WIRO Aug–Oct semester 2010
PI: **Marsh, A. N.**
CoIs: McSwain, M. V., Roettenbacher, R. M., & Aragona, C.

Observing Experience

Kitt Peak National Observatory	
Coudé Feed with Spectrograph (17 nights)	2008, 2011
2.1m Telescope with Spectrograph (8 nights)	2011
Wyoming Infrared Observatory	
2.3m Telescope with Spectrograph (17 nights)	2010, 2012
Cerro Tololo Inter-American Observatory	
0.9m Telescope with Imager (35 nights)	2009 – 2013

Professional Development

Member of American Astronomical Society	Fall 2008 – Present
CAE Introductory Teaching Workshop	January 2013
GRC Meeting: Astronomy's Discoveries and Physics Education	June 2012
Virtual Astronomical Observatory Workshop for Educators	January 2012
Teacher Development Series for Higher Education	Fall 2011, Spring 2012
Member of Sigma Xi	Spring 2011 – Present
President's Leadership Program at Christopher Newport University	Fall 2004 – Spring 2008

Publications

Graduate Work at Lehigh University

Bonnefoy, M., (66 coauthors) et al. *Characterization of the gaseous companion κ Andromedae b: New Keck and LBTI high-contrast observations* 2013, A&A, submitted

Boyer, A. N. M., McSwain, M. V., Aragona, C., & Ou-Yang, B. *Physical Properties of the B and Be star Populations of h and χ Persei* 2012, AJ, 144, 158

Napoli, V. J., McSwain, M. V., **Marsh Boyer, A. N.**, & Roettenbacher, R. M. *The Distance of the Gamma-ray Binary 1FGL J1018.6-5856* 2011, PASP, 123, 1262

Grundstrom, E. D., McSwain, M. V., Aragona, C., Boyajian, T. S., **Marsh, A. N.**, & Roettenbacher, R. M. 2011, Bulletin of the Liége Royal Scientific Society, 80, 371

Marsh, A. N., McSwain, M. V., Currie, T. *Analysis of the B and Be-star Populations of the Double Cluster h and χ Persei* 2010, Proceedings of IAU Symposium 266, 462

Marsh, A. N., McSwain, M. V., Currie, T. *Analysis of the B and Be-star Populations of the Double Cluster h and χ Persei* 2010, Active B Stars Newsletter

McSwain, M. V., De Becker, M., Roberts, M. S. E., Boyajian, TṠ., Gies, D. R., Grundstrom, E. D., Aragona, C., **Marsh, A. N.**, & Roettenbacher, R. M., *Multiwavelength Observations of the Runaway Binary HD 15137* 2010, AJ, 139, 857

Aragona, C., McSwain, M. V., Grundstrom, E. D., **Marsh, A. N.**, Roettenbacher, R. M., Hessler, K. M., Boyajian, T. S., Ray, P. S., *The Orbits of the γ-ray Binaries LS I +61 303 and LS 5039* 2009, ApJ, 698, 514-518

Undergraduate Work at Jefferson National Laboratory

Lou, W., (109 coauthors) et al. *Polarization Components in π^o Photoproduction at Photon Energies up to 5.6 GeV* 2012, PhRvL, 108, 222004

Meziane, M., (110 coauthors) et al. *Search for effects beyond the Born approximation in polarization transfer observables in $\vec{e}p$ elastic scattering* 2011, PhRvL, 106, 132501

Puckett, A. J. R., (105 coauthors) et al. *Recoil Polarization Measurements of the Proton Electromagnetic Form Factor Ratio to $Q^2 = 8.5GeV^2$* 2010, PhRvL, 104, 2301

Presentations

Boyer, A. N. M., *Analysis of B and Be Star Populations of the Double Cluster h and χ Persei*, Lehigh University, July 18, 2013, Dissertation Defense

Boyer, A. N. M., McSwain, M. V., Touhami, Y., Aragona, C. *Physical Properties of the Be Star Disks in h and χ Persei*, 2013, AAS 221, poster #144.25

Boyer, A. N. M. *Massive Stars with Disks* Oct. 14 2012, Lehigh Valley Amateur Astronomy Society, public talk

Boyer, A. N. M., McSwain, M. V., Aragona, C. *The Spectral Energy Distributions of the Be Stars of h and χ Persei*, 2012, AAS 219, poster #344.21

Boyer, A. N. M., McSwain, M. V., *Analysis of B and Be Star Populations of the Double Cluster h and χ Persei*,"Four Decades of Research on Massive Stars", July 11-15, 2011, poster

Marsh, A. N., McSwain, M. V., *Analysis of B and Be Star Populations of the Double Cluster h and χ Persei*, AstroPhilly meeting, May 21, 2011, talk

Marsh, A. N., McSwain, M. V., & Currie, T., *Analysis of B and Be Star Populations of the Double Cluster h and χ Persei*, 2009, IAU S26, poster #68

Marsh, A. N., Ou-Yang, B., Danly, C., McSwain, M. V., & Currie, T., *Analysis of B and Be Star Populations of the Double Cluster h and χ Persei*, Lehigh Academic Symposium, April 16, 2009, poster

Marsh, A. N., Ou-Yang, B., Danly, C., McSwain, M. V., & Currie, T., *Analysis of B and Be Star Populations of the Double Cluster h and χ Persei*, 2009, AAS 213, poster #407.03

Marsh, A., for the GEp-III Collaboration, *The GEp-III Experiment at Jefferson Lab: Understanding the Structure of the Proton*, Paideai Research Conference at Christopher Newport University, April 2008, talk